2007

Combinatorial fabrication & studies of small molecular organic light emitting devices (OLEDs) and structurally integrated OLED-based chemical and biological sensors

Zhaoqun Zhou
Iowa State University

Combinatorial fabrication & studies of small molecular organic light emitting devices (OLEDs) and structurally integrated OLED-based chemical and biological sensors

by

Zhaoqun Zhou

A dissertation submitted to the graduate faculty

in partial fulfillment of the requirements for the degree of

DOCTOR OF PHILOSOPHY

Major: Condensed Matter Physics

Program of Study Committee:
Joseph Shinar, Major Professor
John Hill
Michael Tringides
Gary Tuttle
Rana Biswas

Iowa State University

Ames, Iowa

2007

TABLE OF CONTENTS

ACKNOWLEDGEMENTS

I am deeply indebted to my major professor Joseph Shinar for supervising my graduate studies. His wide knowledge and logical way of thinking have been of great value for me. Without his inspiration and understanding, it would have been impossible for me to finish my Ph. D work at ISU.

I especially thank Dr. Ruth Shinar for her persistent help throughout my whole Ph.D research. Her understanding, encouragement and personal guidance have provided a good basis for this thesis. It would be unimaginable for me to seek the beautiful truth of science inside this work without her.

My most sincere gratitude also extends to Professors John C. Hill, Michael Tringides, Garry Tuttle and Rana Biswas for taking time from their busy schedule to help me with this work. The meaningful discussions with each professor will benefit me throughout my whole life.

My sincere thanks also go to Dr. Gang Li and Dr. Yun Tian for their helpful discussions in research and life. I also want to extend my thanks to my group members, Ying Chen, Zhengqing Gan, Yuankuan Cai, Min Cai and Teng Xiao, who have made my life enjoyable.

I would also like to thank the many staff members of the physics department and Ames Laboratory for all of their help, especially Diane Smith, Joyce Smith, Rebecca Shivvers and Lori Hockett. The financial support of the Iowa State University is gratefully acknowledged.

I have been blessed with a wonderful family that has been an unending source of support and encouragement. I especially thank my parents, whose faith has encouraged my own and who taught me so many things, most recently exemplifying optimism and perseverance. Finally and most importantly, my deepest thanks to my wife Qiaoli Chen, for her amazing love and support.

1. INTRODUCTION TO ORGANIC LIGHT EMITTING DEVICES (OLEDS) AND STRUCTURALLY INTEGRATED OLED-BASED CHEMICAL AND BIOLOGICAL SENSORS

1.1 What is an OLED?

OLED refers to **o**rganic **l**ight **e**mitting **d**iode (or **d**evice) [1], which is a cutting edge technology of using organic materials (small molecular or polymeric) to generate light. The basic structure of an OLED consists of a stack of organic layers sandwiched by a transparent conducting anode and a metallic cathode. With suitable driving voltage applied to the diode, holes are injected from the anode and electrons from the cathode; both holes and electrons are driven by the electric field and meet in the recombination zone; their recombination results in electroluminescence (EL). Such technology can be used in portable system screens, television screens, computer displays, advertisement information indication, and general illumination as well. One of the great advantages of OLED technology over conventional displays is that OLEDs do not require backlights to function, which saves much more space than current technologies like liquid crytal displays (LCDs).

1.1.1 History of OLEDs

The first organic EL was reported by M. Pope et al. [2] and W. Helfrich et al. [3] in the early 1960's. The organic material they used at that time was anthracene single crystals, which has relatively high carrier mobility. In order to detect the EL coming from the several microns-thick crystal, the onset voltage, defined as the driving voltage required to reach a luminance of 1 Cd/m^2) was over 100 V. Due to this high driving bias and low brightness, for

a very long time this organic EL drew only limited interest. In 1982, P. S. Vincett [4] achieved progress by vacuum-depositing 0.6 μm thick anthracene crystal films with driving voltage of less than 100 V. However, the lower quantum efficiency (less than 0.1%) and high driving bias still limited the application of this technology.

In 1987, C. W. Tang and S. A. VanSlyke achieved a breakthrough in organic EL [5]. They fabricated around 100 nm thin amorphous organic layers by thermally evaporating small molecular organic materials in vacuum. Although it was well-known that disordered films possess inferior electron transport properties relative to the crystalline films [6], the material purity achieved by train sublimation and vacuum thermal evaporation of organic thin films resulted in excellent pinhole-free physical properties, which were manifest in extremely thin and low driving voltage organic cell. The organic device in reference 5 was made of small molecular weight organic materials including N, N'-diphenyl-N, N'-bis(3-methylphenyl) 1, 1'-biphenyl-4, 4' diamine (TPD) and tris(quinolinolate) aluminum (Alq3). High external quantum efficiency of 1% (photons/electrons) and high brightness of more than 1000 Cd/m^2 were obtained at an applied voltage of less than 10 V. Following the successful demonstration of such small molecular OLEDs by Tang [5], another dramatic progress in organic EL was achieved by R. H. Friend's group in 1990 [7]. They used poly (*p*-phenylene vinylene) (PPV), which is fluorescent in the yellow-green region, to make the first polymer-based lighting emitting diode (PLED). Partly due to single layer structure, which is inefficient to balance the carriers, the initial PLED possessed very low external quantum efficiency of 0.05%. However, PLEDs have several potential advantages over small molecular OLEDs (SMOLEDs), including a simple structure and a simple low-cost solution-processed fabrication using, e.g., spin coating or ink jet printing.

Since the first development of the thin-film SMOLEDs in 1987 [5] and PLEDs in 1990 [7], the development of these two branches proceeded in parallel with dramatic progress achieved by various academic, government, and industrial research groups. Based on the first OLED structure proposed by C. W. Tang, researchers [8-13] successfully developed multi-layer structure by inserting carrier injection and transport layers between two electrodes to improve device performance.

1.1.2 Advantages of OLEDs

The first commercial products incorporating OLEDs were car stereos debuted in 1997 by Pioneer. Since then, more and more companies are applying OLED-based technology not only in displays [14-18] and general illumination [19-21] but also in photodetectors [22-24], photovoltaic cells [25-27], sensors [28-30] and field effect transistors [31-33]. Major organic electronic companies such as Philips and Pioneer, Sony, Universal Display Corporation, Cambridge Display Technology, Eastman Kodak, DuPont, General Electric, Samsung SDI, and Seiko Epson, are investing heavily in this emerging technology to produce low cost and high performance products. Currently, most of OLEDs products focus on low information content displays with limited size such as mobile phones, PDAs, MP3 players, digital cameras, digital camcorders and some virtual imaging displays. The advantages of OLEDs over conventional technology such as cathode ray tube (CRT) or liquid crystal display (LCD) are summarized in Table 1.

The disadvantages of OLED-based products are mainly related to the lifetime. In order to commercialize a product, operational time of above 10,000 hours at a brightness level of at least 100 Cd/m^2 is normally required, except for some portable electronics. Yet it

is well known that the organic materials are sensitive to oxygen and moisture, so suitable encapsulation is needed to protect the organic cell from degradation. In recent progress (as of December 2006), Universal Display Corporation and Cambridge Display Technology announced lifetimes, at an initial luminance of 100 Cd/m^2, of 600,000 hours for green SMOLEDs (CIE color coordinates x = 0.35, y = 0.61) and 400,000 hours for blue (CIE coordiates x = 0.14, y = 0.21) PLEDs, respectively. The rapid improvement in their performance will greatly accelerate their commercialization.

Table 1. Performance comparison of OLED with conventional display (source: MIT online organic lecture).

Performance	AMLCD	PMLCD	LED	PDP	CRT	OLED
Brightness	Good	Good	Very good	Good	Good	Very good
Resolution	High	High	Poor	Medium	High	High
Driving Voltage	Low	Low	High	High	Very high	Low
Viewing Angle	Medium	Poor	Excellent	Excellent	Excellent	Excellent
Contrast Ratio	Good	Fair	Good	Fair	Excellent	Excellent
Response time	Good	Poor	Fast	Very fast	Very fast	Very fast
Power Efficiency	Good	Good	Fair	Medium	Poor	Very good
Temperature Range	Poor	Poor	Very good	Very good	Very good	Very good
Flexibility	Fair	Fair	No	No	No	Good
Form Factor	Thin	Thin	Thick	Thick	Very thick	Very thin
Weight	Light	Light	Fair	Heavy	Heavy	Very light
Screen Size	Small to Large	Small to medium	Small to Large	Large	Small to Large	Small to Large
Primary Applications	Computer displays, TV, Monitors	Small displays, like cell phone, PDA	Sign, indicators, Large ad display	Large display, like TV,	TV, receding from market	Multiple usage, New/Existing
Cost	Average	Low	High	High	Low	Low

1.1.3 OLEDs in the future

The most dominant reasons for pursuing organic electronics are high quality and low cost productions. Since the first reports on thin film OLEDs in 1987, researchers worldwide

are making strong efforts to commercialize this new cutting-edge technology. There is no doubt that current organic electronic devices in the market are commercially valuable. The striking improvements in the lifetime and efficiency of OLEDs demonstrate that organic electronics will certainly be a new exciting lucrative industry.

One of the major future applications of OLEDs would be in general lighting. There is no known fundamental physical reason why 21st century lighting technology should not be greatly more efficient, thereby reducing equally greatly our energy consumption [34]. 620 billion kilowatt-hours per year would be saved by 2025 if 50%-efficient technology would be employed, which would eliminate the need for about 70 nuclear plants, each generating a billion Watts of power. The advent of OLED technology has already provided scientific background and market potential to replace conventional lighting.

Another major application of OLEDs is display. Customers have been using OLED-based small size displays ranging from car stereos, MP3s, and PDAs since 1997 (see Figure 1). As for large-size OLED-based displays, the schedule is almost on the table. In the 2007 Consumer Electronics Show (CES), Sony demonstrated its latest two OLED displays, with sizes comparable to current TVs, and expects to ship mass-produced OLED TVs as early as 2008.

In addition to OLED applications in general illumination and displays, there are other emerging organic thin film semiconductor technologies such as solar cells [25-27], thin-film transistors [31-33], organic photodetectors [22-24], and organic memory devices..

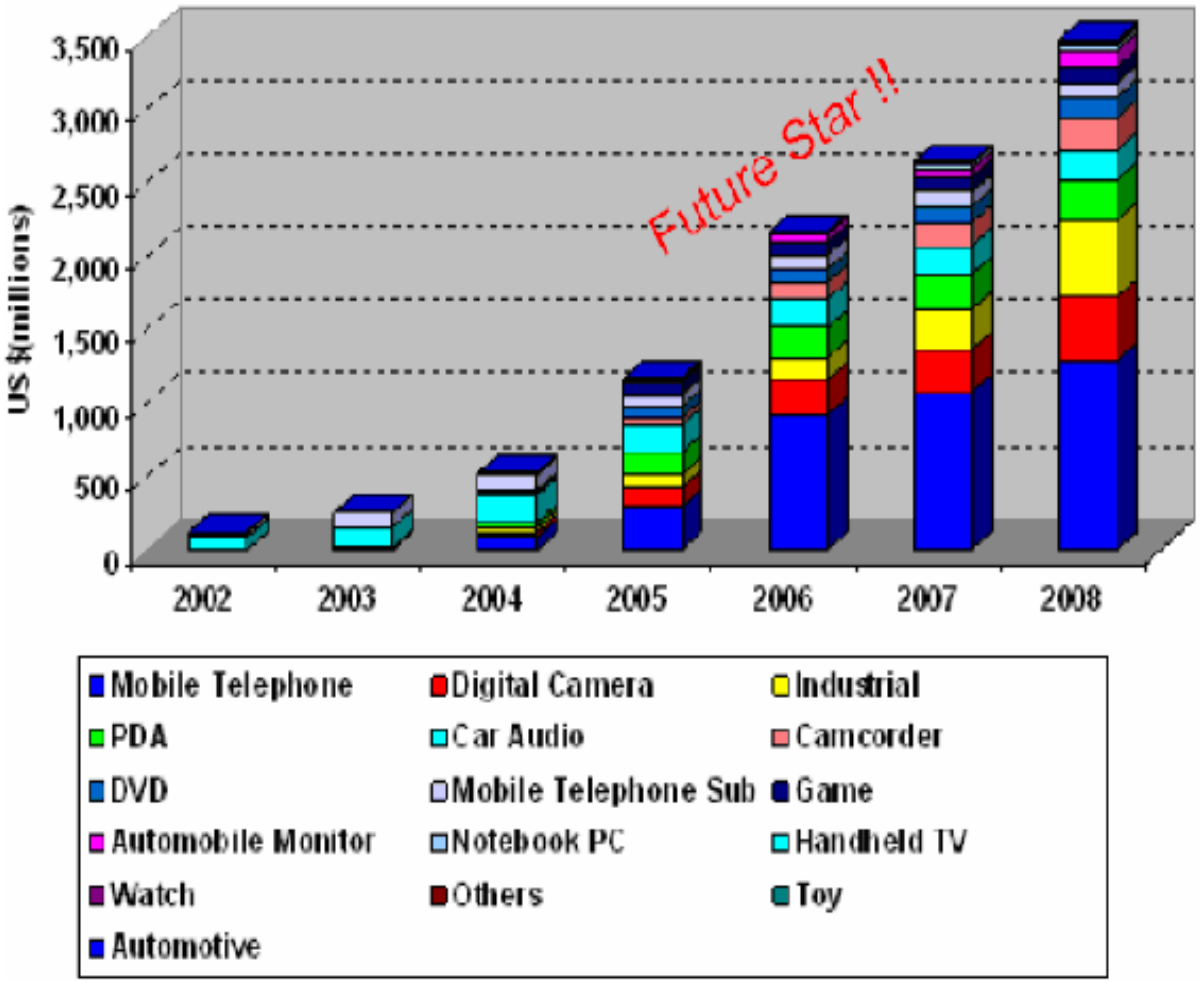

Figure 1. OLED application trends in display.

Source: http://www.displaysearch.com/press/2003/122303.htm

It is worth to note that currently a lot of ongoing research seeks to improve the performance of OLEDs, such as color gamut, efficiency and stability etc. Recently, a hybrid device [35-36], which incorporates nanocrystal (NC) quantum dots into OLEDs (NC-OLEDs), has been suggested as a new form of display platform to overcome the disadvantages of OLEDs. The optical properties of this NC-OLED are determined by the quantum confinement effect [37], so that the emission color and the electron affinity can be finely controlled not only by the material choice but also by size within a single synthetic

route. The high radiative recombination efficiency of excitons and narrow emission spectra of inorganic NCs and the low cost fabrication of organic semiconducting films would make these hybrid devices highly advantageous, especially in terms of color purity and brightness.

1.2 Basic properties of OLEDs

1.2.1 Basic structure

The most significant step in developing thin-film OLEDs was using thermally evaporated amorphous films to fabricate organic heterostructures sandwiched between the transparent indium tin oxide (ITO) anode and a metal, typically Al, cathode [5]. The energy level diagram of such a typical organic heterostructure is shown in Fig. 2.

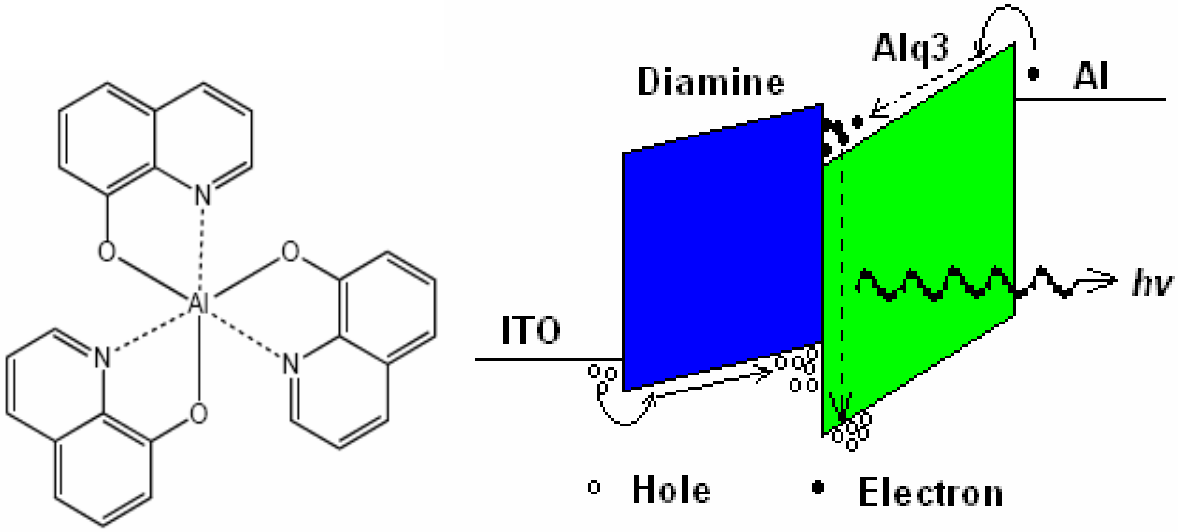

Figure 2. Molecular structure of Alq3 and bi-layer structure of a SMOLED.

The first OLEDs consisted of thin films of diamine and Alq_3 grown on the ITO substrate, then capped with Al. The total organic film thickness was about 100 nm. Under forward bias, electrons and holes are injected from the Al cathode and ITO anode,

respectively. Due to the unbalanced carrier motilities, the excitons are formed in the Alq_3 layer adjacent to the interface with the hole transport layer.. Due to the extreme thin layer of organic films (normally around 100 nm), the typical driving voltage ranges from 2 to 15 V, which generates decent brightness to satisfy the demands of displays or general lighting.

One of the successful points in the first SMOLEDs was using heterostructures, which functionally contain a hole transport layer (HTL) and an electron transport layer (ETL) to balance the carriers density in the recombination region. Later on, researchers [8-13] used multilayer structures, including hole injection layer (HIL), HTL, recombination layer, ETL, and electron injection layer (EIL), to greatly improve carrier balance and improve device efficiency.

1.2.2 Carrier transport in organic devices

The processes in OLEDs that culminate in EL include four distinct steps: carrier injection, carrier transport, electron-hole recombination at a molecule that results in exciton formation, and radiative decay of that exciton.

1.2.2.1 Carrier injection

Under an applied voltage, electrons are injected from the cathode into a lowest unoccupied molecular orbital (LUMO) level of the adjacent EIL or ETL and holes are injected from the anode into a highest occupied molecular orbital (HOMO) of the adjacent HIL or HTL. Neglecting surface states, the carrier injection process can be described by two mechanisms [38]: Fowler-Nordheim tunneling and thermionic injection.

1.2.2.1.1 Fowler-Nordheim tunneling

Neglecting surface states, there is typically a triangular energy barrier caused by the mismatch between the work function (Φ) of the electrode and the electron affinity (EA) or the ionization potential (IP) of the adjacent organic layer. (see Fig. 2). Under the applied bias, the Fermi level of the organic semiconductor E_{Fm} will be shifted up and the tunneling process can easily happen. Fowler and Nordheim demonstrated [38] that the significant possibility of carrier tunneling occurs when an electric filed was applied. The field emission current density based on their model is given by:

$$J = \frac{A^* T^2}{\phi_B}(\frac{eE}{\alpha k_B T})^2 \exp(\frac{2\alpha \phi_B{}^{3/2}}{3eE}) \quad (1)$$

Where $A^* = (4\pi e m^* k_B{}^2)/h^3$, ϕ_B is the potential barrier in the interface between the electrode and organic semiconductor, E is the applied electric field, and

$$\alpha = \frac{4\pi(2m^*)^{1/2}}{h} \quad (2)$$

Equation (2) describes the barrier. m^* is the effective mass of the charge carriers. Denoting

$$\beta = \frac{2\alpha \phi_B{}^{3/2}}{3e} \quad (3)$$

Then the current density can be written as:

$$J \propto E^2 \exp(-\frac{\beta}{E}) \quad (4)$$

It also can be expressed in this way,

$$\ln(\frac{J}{E^2}) = -\beta \frac{1}{E} + c \quad (5)$$

A plot of $\ln(\frac{J}{E^2})$ versus $\frac{1}{E}$ gives a straight line with a negative slope, which yields β.

1.2.2.1.2 Thermionic injection

Charge injection at low bias is primarily due to the thermal emission of charges carriers over the interface potential barrier when the barrier is not too high for thermionic injection. The current density is then given by the Richardson law [39]:

$$J = A^{*}T^{2}\exp(-\frac{\phi_B}{k_B T}) \tag{6}$$

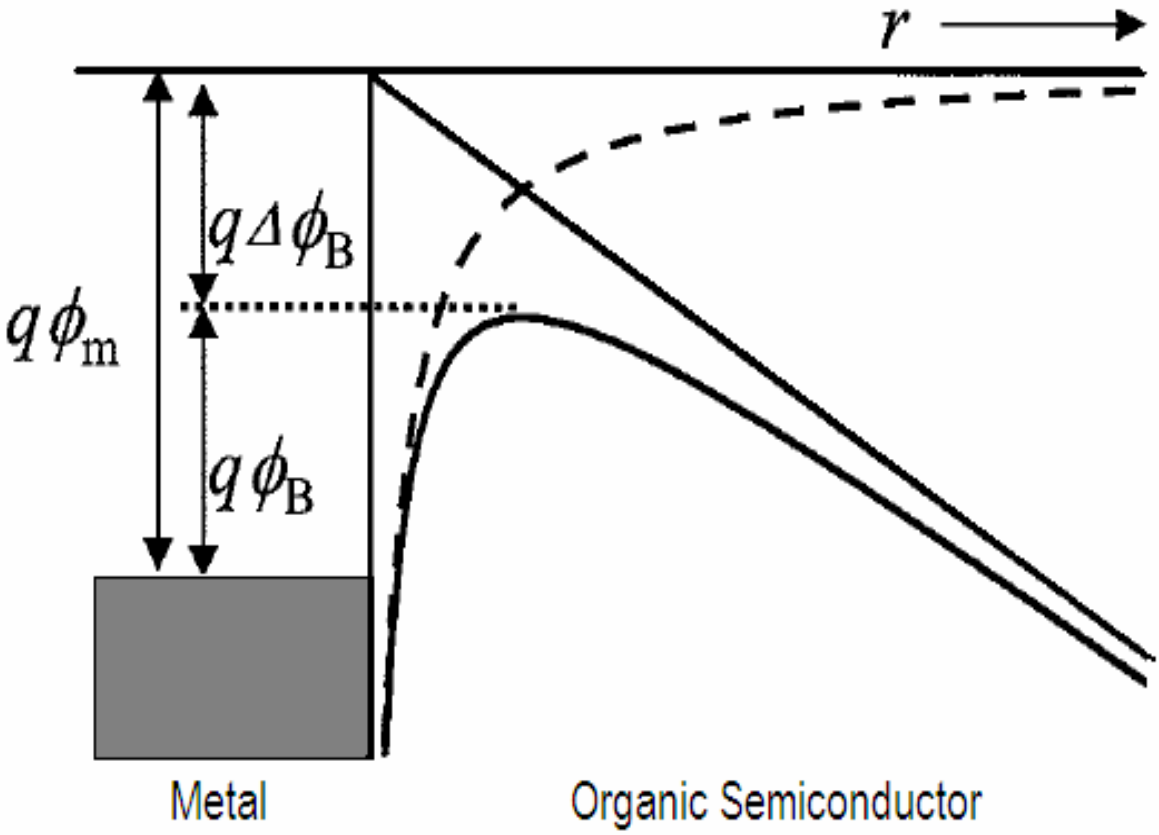

Figure 3 Metal-organic contact illustration.

Basically, the Richardson law describes charge carrier flow taking into account only the carrier flux from both contacts. However, image charge forces should be also considered.

When an electric field E exists at the interface, the actual barrier ϕ_B is lowered by an amount $\Delta\phi_B$:

$$\Delta\phi_B = (\frac{e^3}{4\pi\varepsilon\varepsilon_0})^{1/2} E^{1/2} = \nu E^{1/2} \quad (7)$$

Where $\nu = (\frac{e^3}{4\pi\varepsilon\varepsilon_0})^{1/2}$ is a constant in equation (7). Then the current density becomes

$$J = A^* T^2 \exp(-\frac{\phi_B}{k_B T}) \exp(\frac{2\nu E^{1/2}}{k_B T}) \quad (8)$$

Which is also called the Richardson-Schottky law [40].

1.2.2.2 Carrier transport

Following carrier injection from the electrodes, charged excitations move under the influence of the applied electric field. In transport-limited single organic layer OLEDs, three major conduction mechanisms are commonly significant [41]: ohmic conduction, space-charge-limited conduction (SCL), and trapped-carrier limited (TCL) space charge conduction.

1.2.2.2.1 Ohmic conduction

Ohmic conduction is observed at low voltages when the density of injected carriers is smaller than the thermally generated background free charge density. In this regime, the current density is governed by Ohm's law:

$$J = e\mu_n n_0 V / d \quad (9)$$

Where e is the electronic charge, μ_n is the electron mobility, n_0 is the free charge density, V is the applied bias, and d is the thickness of electron transport layer.

1.2.2.2.2 Space charge limited current (SCLC) regime

At higher applied bias, the number of carriers in the organic semiconductor increases above the free charge density, which results in a build-up of space charge in the organic material. Consequently, Ohm's law is invalid in this regime.

Firstly, the Poisson's equation was applied to the electric field in the presence of space charge:

$$\frac{dE(x)}{dx} = \frac{\rho}{\varepsilon} = \frac{e[n(x) + n_t(x)]}{\varepsilon} \tag{10}$$

Where ρ is the charge density, *n(x)* is the thermally generated free charge density and $n_t(x)$ is the trapped charge density. The current density is then given by:

$$J = e\mu_e n(x)E(x) \tag{11}$$

In the absence of traps, a combination of Eqs. (10) and (11) yields

$$2E(x)\frac{dE(x)}{dx} = \frac{2J}{\varepsilon\mu} \tag{12}$$

This can be solved using the boundary condition for the applied voltage $V = \int_0^d E(x)dx$ to obtain the current density [38]:

$$J = \frac{9}{8}\varepsilon\mu\frac{V^2}{d^3} \tag{13}$$

This equation is valid only for sufficiently high bias because the diffusion component is no longer negligible in the lower bias range. The transition at which SCLC takes over from Ohmic conduction occurs when the SCLC current is equal to the Ohmic current.

1.2.2.2.3 Trapped carrier limited space charge conduction

At higher bias, the quasi-Fermi level rises toward the LUMO, filling traps that might exist in the energy gap of the organic layer. The trap concentration and energy distribution govern J at high trap density, which results in trapped charge limited space charge conduction. The current density versus applied voltage can be expressed by [42]

$$J = N_{LUMO}\mu_n e^{(1-m)}[\frac{\varepsilon m}{N_t(m+1)}]^m(\frac{2m+1}{m+1})^{(m+1)}\frac{V^{(m+1)}}{d^{(2m+1)}} \tag{14}$$

Where N_{LUMO} is the density of states in the LUMO band, N_t is the total trap density, and

$$m = \frac{T_t}{T} = \frac{E_t}{kT}, \tag{15}$$

Where E_t is the characteristic trap energy.

1.2.3 Carrier recombination and device efficiency

1.2.3.1 Carrier recombination

Under the applied electric field, both electrons and holes will drift toward each other and recombine on a molecule to form a Frankel exciton on that molecule..

The capture of a free electron by a free hole to form an exciton is a bimolecular process. The recombination rate can be expressed by

$$R = \frac{dN_{exciton}}{dt} = \gamma pn \tag{16}$$

Where $\gamma = \frac{e}{\varepsilon}(\mu_n + \mu_p)$ is the bimolecular capture constant, and p, n are the hole and electron concentrations in the recombination zone, respectively.

The Langevin process assumes that the capture of the electron or hole is random, and that the escape of the electron or hole from the encounter center involves two mechanisms: a thermally activated step to escape the Coulomb potential, and sufficiently kinetic energy to escape. Thus, recombination to an exciton requires an electron-hole separation, called the Langevin radius [43-45], no larger than

$$R_{recom} = \frac{e^2}{4\pi\varepsilon kT} \tag{17}$$

A typical value for R_{recom} is around 180 Å at 300K since $\varepsilon \sim 3\varepsilon_0$ for most organic materials.

1.2.3.2 Device efficiency

The internal quantum efficiency (IQE) is the ratio of the number of photons emitted inside the device to the number of injected electrons. The binding energy of the Frankel excitons in molecular semiconductors is ~1 eV. If the injected electrons and holes, each with a spin 1/2, are not spin polarized, simple spin statistics lead to 25% singlet excitons (SEs) and 75% triplet excitons (TEs). Since the ground state wave functions of these molecules are typically spatially symmetric under electron exchange, i.e., they are spin 0 singlet states, spin conservation forbids radiative decay of the TEs. The EL is therefore limited to the allowed radiative decay of the SEs, and the maximal IQE is IQE_{max} = 25%. This allowed SE emission is termed fluorescence, as distinct from the normally forbidden radiative TE decay, which is termed phosphorescence.

Although the radiative decay from TEs to the singlet ground state is normally forbidden as it violates spin conservation, certain second order effects may mix singlet and

triplet states, rendering the decay of the resulting state weakly allowed. Singlet-triplet mixing also enhances SE to TE energy transfer, known as intersystem crossing (ISC) [46]. Such singlet-triplet mixing can result from spin-orbit coupling. This coupling is due to the interaction between an electron's spin and the magnetic moment created by the electron oscillating in a closed orbit. Since the spin-orbit interaction is proportional to Z^4, incorporation of heavy metal atoms such as europium, platinum, and iridium, in the organic molecule can lead to efficient phosphorescence [47].

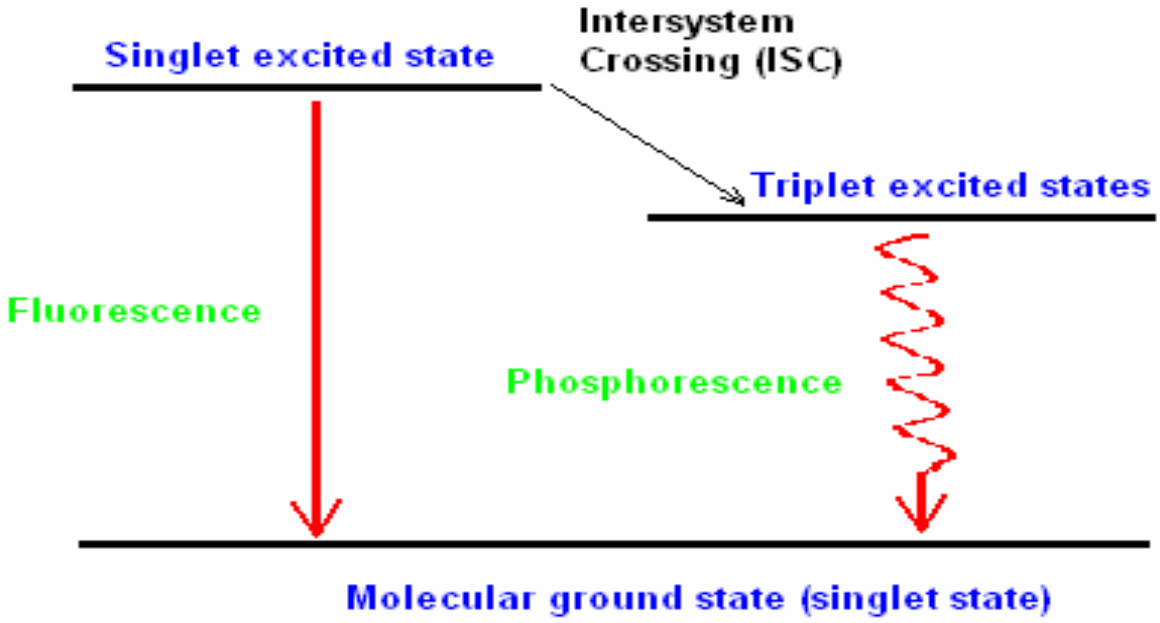

Figure 4. Illustration of fluorescence and phosphorescence operational mechanisms.

Thus, while IQE_{max} is only 25% in fluorescenct OLEDs, in phosphorescence devices it can reach 100% as such devices can be fabricated to harvest the radiative decay of all the excitons.

The other limitation to the IQE of OLEDs is the photoluminescence (PL) efficiency of the emissive material, Φ_{PL}, which defines the ratio of emitted photons over absorbed

photons under optical excitation. Since the absorption of triplet excitons is typically weak, Φ_{PL} is generally a measurement of the efficiency of the re-radiation of absorbed singlet excitons. Through chemical optimization and material processing, Φ_{PL} can often approach 100%.

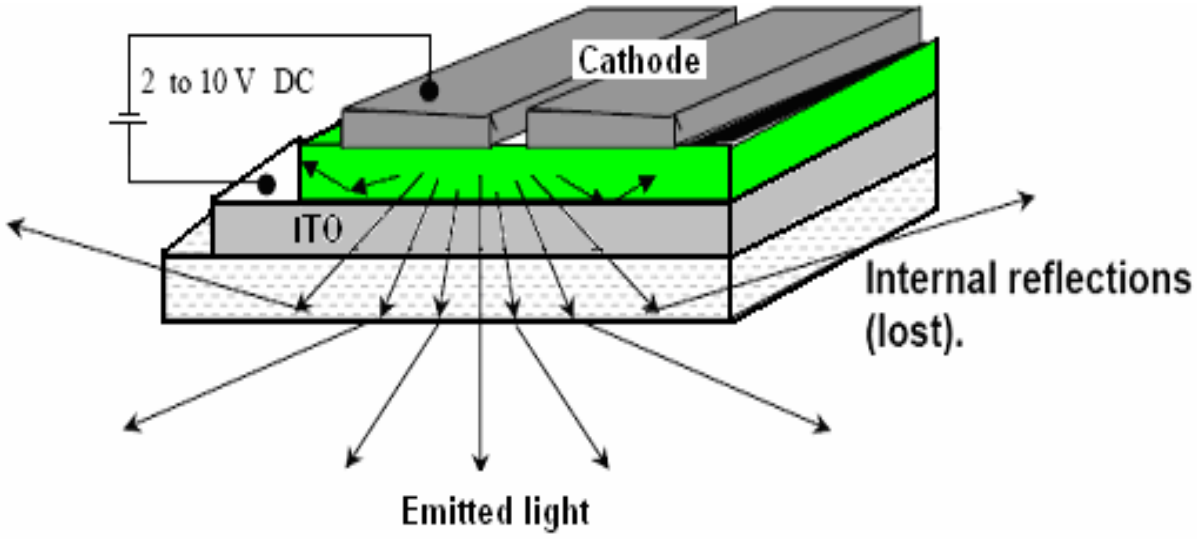

Figure 5. Device output coupling efficiency illustration.

Besides the IQE, another factor limiting the overall external quntum efficiency η_{EQE} is the outcoupling factor η_{out}. Due to the higher refractive index n of the organic layer than the cladding layers outside, η_{out}, which depends on the direction of the dipole moment of the emitting molecules and the refractive index n of the emitting layer, is estimated to be $\eta_{out} = 1/(2n^2)$ for isotropic dipoles of the emitter, and $\eta_{out} = 1/n^2$ for in-plane dipoles [48].

Considering the carrier recombination probability, the external quantum efficiency η_{EQE} of an OLED under external bias may be expressed as:

$$\eta_{EQE} = \eta_{out} \chi \Phi_{PL} \zeta, \tag{18}$$

where η_{out} is the output coupling efficiency (typically around 20%), χ is the fraction of emissive excitons (25% for fluorescence and 75% for phosphorescence), Φ_{PL} is the PL quantum efficiency of the emissive material (up to 100%), and ζ is the carrier balance factor (can be tuned to 1 with structure optimization).

However, even with an optimal structure, several loss mechanisms still have to be considered; these are due to various exciton quenching processes:

(i) Increased polaron population at high electric field. These polarons are effective quenching sites for SEs [49].

(ii) Exciton-exciton annihilation at high electric field [50].

(iii) Heat accumulation in the device due to the electric power dissipation results in an increase in temperature [51], which increases collisional quenching, or increase the non-radiative decay rate of the SEs

(iv) Quenching by the electrodes if the recombination zone is too close to the electrodes [52], or the position of the recombination zone changes with increasing field and moves toward the electrodes.

(v) Finally, quenching is also caused by field-induced annihilation of SEs [53].

Thus, in order to maximize the efficiency of OLEDs, it is necessary to ensure that: 1) essentially all electrons and holes injected from electrodes into the structure form excitons, 2) the excitons recombine radiatively with high probability, 3) the recombination zone is far from the quenching electrodes, 4) the light emitted by exciton decay is efficiently coupled out of the device, 5) the bias for a given current density is minimized, and 6) the materials used in the device are intrinsically highly efficient and thermally stable.

1.2.4 Degradation mechanisms of OLEDs

Stability is one of the most important criteria for commercialization of OLEDs. Typical lifetimes of commercial electronic product (such as displays) is at least 10 years with normal usage, which means a lifetime >10,000 hours, at initial display brightness (luminance) of 100 cd/m^2, is required. Significant improvements have been made on the stability of organic devices over the last two decades.

The degradation of the devices during operation demonstrates following characteristics: 1) decay of luminance; 2) voltage increase in the constant-current mode; 3) growth of nonemissive black spots; 4) color distortion. The degradation mechanisms could be attributed to the following processes.

1.2.4.1 Morphological degradation

1.2.4.1.1 The role of electrodes in degradation

ITO is widely used as the transparent electrode for light output in OLEDs or light input in photovoltaic devices. However, ITO may decompose at high temperature since it is a metal oxide. It liberates not only oxygen but is also the source for In electromigration into the organic layer. Lee and coworkers proposed that the In centers in the organic matrix are PL-quenching centers [54]. To investigate whether the presence of trace amounts of In in organic layer could cause a significant EL decrease, they deliberately doped In into different regions of OLEDs and tested their efficiency. The results showed that only the EL efficiency of In doped into the emission zone of Alq_3 was greatly decreased, while In had very little influence when doped into other regions. On this basis, they concluded that the deep penetration of In, possibly assisted by electromigration of In ions from oxygen deficient ITO, into the emission

zone, substantially decreases OLED stability. Furthermore, Scott [55] claimed that the oxidation of the polymer in PLEDs by oxygen escaping from ITO, which was tested in the absence of atmospheric oxygen, also leads to the loss of EL efficiency. Some investigators [56, 57] proposed that an intermediate layer was created between ITO and organic layer due to the diffusion of ITO into the polymer layer, which results in the low efficiency.

A variety of countermeasures to the foregoing ITO-induced degradation processes have been proposed. For example, ITO surface treatment, such as UV ozone cleaning [58-60] and oxygen plasma treatment [61-62], improve device stability by reducing oxygen deficiency of as-received ITO films, thus creating a more stable surface which may reduce the release of In. Such treatments also reduce the surface roughness and increase the work function, both of which improve OLED performance [63, 64].

Other countermeasures eliminate the direct contact of the ITO with the organic layers by introducting a buffer layer between them, e.g., a carbon layer [65], copper phthalocyanine (CuPc) [66], 4,4',4"-tris[2-naphthyl (phenyl)-amino] triphenylamine (2-TNATA) [67], plasma-polymerized CHF_3 [68], or CuO_x [69]. These buffer layers act as a barrier for In diffusion into the organic layers. In some cases, adding the buffer layer also aligns the energy level to reduce the barrier for hole injection into the organic layer, which also improve the performance of the OLEDs.

Another possible degradation is due to the cathode. Huang *et al.* revealed Al penetration into Alq_3 at a rate of 10^{-18} cm^2/s and a strong correlation with Alq_3 PL quenching [70]. They proposed that penetration and PL quenching can be effectively suppressed by ~20 Å of an intervening layer of Al_2O_3 at the Alq/Al interface. However, no evidence was shown that Mg diffused into Alq_3 layer for devices with a Mg/Ag cathode. Aziz and coworkers [71]

demonstrated that cathodes utilizing a mixture of metals and organic materials have the ability to retard dark-spot formation caused by cathode element diffusion into the organic layer.

1.2.4.1.2 The role of moisture and oxygen in degradation

Humidity-induced degradation is regarded as a major cause for the growth of dark spots in improperly encapsulated OLEDs. This degradation includes three distinct mechanisms.

a) Humidity induced electrochemical reaction.

In the ambient environment, the dark spots grow very fast under applied bias but growth stops immediately when the bias is turned off [72]. This provides strong evidence that their growth is related to an electrochemical process. The chemical reduction of water under bias can be expressed by

$$2H_2O + 2e^- \rightarrow H_2 + 2OH^- \quad (19)$$

The water vapor penetrates into organic device through aluminum cathode micro-cracks, pinholes, and edges of the encapsulated OLED, then it is reduced and generates H_2 gas under applied bias. Due to the gas pressure formed under the cathode, bubbles or dome-like structures are created [73, 74]. When the pressure inside the dome reaches a critical level, the bubble burst, creating additional access for penetration of more water into the film. The pressure from the bubble, and its rupture, may also delaminate the Al cathode, leaving non-emissive regions, namely dark spots or black spots, due to the absence of electron injection in those regions. Fung [75] and his coworkers used a hydrophilic layer of calcium deposited on top of cathode as a sacrificial layer to inhibit the humidity-induced degradation, providing

additional evidence that water penetration into the organic layers speeds up OLED degradation.

b) Humidity induced crystallization of Alq_3.

Aziz et al. [76] demonstrated that humidity induces crystallization of Alq_3. As the crystalline Alq_3 clusters grow in the organic film, they may lift and delaminate the cathode due to their volumetric change. The crystallization of Alq_3 was confirmed by polarization microscopy, in which the cluster rotated a plane polarized incident beam of light. Cathode pinholes and micro-cracks subsequently provide the entry channel for water and oxygen.

The growth of oxygen-induced dark spots is very different from that induced by water vapor. Despite the fact that the oxygen partial pressure in air is 50 times higher than that of water, the oxygen-induced dark spot growth rate is $\sim 10^3$ times lower than the water vapor-induced rate [72].

The degradation due to water and oxygen can be effectively suppressed by proper device encapsulation [77-80]. A glass cover with epoxy around the encapsulation edge provides an easy and simple way to slow down the degradation process. The Barix™ encapsulation developed by Vitex Systems, Inc. [81] employs alternative coatings of ceramic and polymer layers to achieve a smooth and lightweight protection layer for the OLEDs.

1.2.4.2 The role of structural defect in organic film.

This kind of degradation causes a sudden decrease or total loss of luminescence due to an electrical short that develops across the device. As discussed above, the OLED typically consists of several amorphous organic layers with a total thickness of ~100 nm. For such thin films, surface roughness can play a critical role in determining the electrical properties, and

the thin film is prone to shorting through defect channels at the high electric fields (~1 MV/cm) present under bias [82]. The morphological related defects or pinholes in the organic layers become hot spots during device operation, resulting in melting or decomposition of the organic layers. Eventually, direct contact between the electrodes occurs at this region, causing a catastrophic failure of the device.

1.2.4.3 Intrinsic degradation mechanism

a) Crystallization of amorphous organic film. Due to the low glass transition temperature of most organic materials, an increased film surface roughness could lead to the interlayer delamination at the organic interface and the subsequent interruption of efficient charge injection. Furthermore, a non-emissive recombination region would form at the boundaries of the crystalline domains. The Joule heat generated during the operation will also accelerate such crystallization if the heat is not effectively dissipated. Major efforts are focused on developing high T_g organic materials to prolong the OLED lifetime [83-85].

b) Formation of Alq_3 cationic quenching centers.

Aziz and co-workers identified this degradation model in 1999 [86]. They proposed that the Alq_3-based OLED stability has close relation with the injection of holes in Alq_3. The transport of holes into Alq_3 causes a decrease in its fluorescence quantum efficiency, thus demonstrating the cationic Alq_3 species are fluorescence quenchers. In order to effectively prevent extra hole injection into the Alq_3 emitting layer, (i) a buffer layer is added at the hole injection contact, or (ii) the NPD HTL is doped with a fluorescent dye such as rubrene, which is an excellent hole trapping center in NPD, or (iii) the Alq_3 is mixed with the hole transporting material [66, 87].

1.2.4.4 Other degradation processes

The growth conditions of the organic layers are also very important for the performance of the OLED. Bohler at al. [88] reported that the device performance (quantum efficiency, turn on voltage) could be significantly improved by using organic molecular beam deposition technique under ultrahigh vacuum (UHV, 10^{-9} mbar), as compared to thermal vacuum evaporation in high vacuum (10^{-6} mbar). In particular, the formation of the black spots in these devices was delayed and they were fewer.

The location of the recombination zone in the organic device affects device stability as well. Matsumura and Jinde [89] calculated the depth of the emitting zone in ITO/TPD/Alq/cathode structures and showed that as the diodes degraded the emitting zone shrank and the zone near the metallic electrode became nonemissive.

It is noteworthy that no single degradation mechanism can explain the aging phenomenon. For example, the degradation mechanism due to indium diffusion into organic layer cannot explain why changing the order of two hole transport layers (NPB and TPD) can affect the OLED stability [90]. The Alq_3 cationic species model cannot explain the degradation mechanism in non-Alq_3 OLEDs. Although dramatic progress on OLED degradation has been made, a complete and consistent understanding of the degradation process is still lacking, leaving room for further highly desirable investigations.

1.3 Overview of OLED-based chemical and biological sensors

1.3.1 Photoluminescence (PL)-based sensors

Since the radiative decay of SEs is allowed, their decay rate is typically 10^9 s^{-1}, so that a typical fluorescence lifetime is ~1 ns. Thus, time-resolved measurement of fluorescence

decay requires fast optics and electronics. In contrast, since the radiative decay of TEs is forbidden, their decay rate is much slower – typically $1 - 10^6$ s^{-1}, so that a typical phosphorescence lifetime can be as long as several seconds. Due to nonradiative quenching processes, phosphorescence is usually not seen in fluid solutions at room temperature. However, as mentioned above, through singlet-triplet mixing by spin-orbit coupling process, organic molecules containing heavy metal atoms reduce the phosphorescence lifetime to values than can be lower than 1 μs [47]. This process also enhances the efficiency of intersystem crossing from the lowest SE state to the lowest TE state.

1.3.2 Jablonski Diagram and Stokes shift

A typical Jablonski Diagram is shown in Figure 6. The ground state, first excited singlet, second excited singlet and excited triplet states are presented as S_0, S_1, S_2, and T_1 respectively [91]. At room temperature, the thermal energy is not adequate to significantly populate the excited vibrational states. Absorption typically occurs from molecules with the lowest vibrational energy.

Following light absorption by a luminescent dye, several processes usually occur. A fluorophore is usually excited to some higher vibrational level of either S_1 or S_2. With extremely fast relaxation process (typically around 10^{-12} s or less), called internal conversion, most molecules relax to the lowest vibrational level of S_1. Since the fluorescence lifetime is much longer than the internal conversion time, the fluorescence emission generally results from a thermally equilibrated excited state, that is, the lowest vibrational state of S_1.

Another spin conversion process, called intersystem crossing, can induce a transition from S_1 to T_1. The emission from T_1 to S_0 is the phosphorescence, and it is generally at longer

wavelength relative to the fluorescence, as the energy of T_1 is typically 0.5 – 1.0 eV lower than that of S_1. Hence, the transition from T_1 back to S_1 is forbidden.

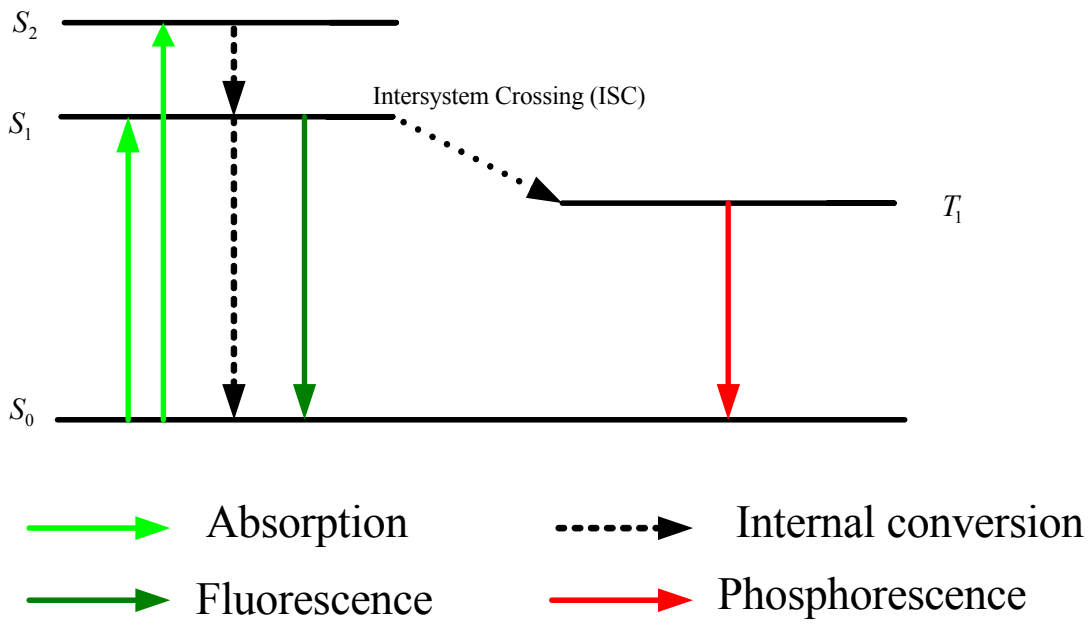

Figure 6. Schematic of Jablonski diagram.

The shift between the excitation energy and emission energy is called the Stokes Shift. As shown in Figure 6, the fluorescence typically occurs at lower energies or longer wavelength. Therefore, it is much easier to distinguish the emission from excitation by putting a long pass filter, which blocks the short wavelength while lets longer wavelength through.

1.3.3 Sensor indicators

Due to the widespread and diverse applications of PL-based oxygen sensors, a wide range of probes have been employed for such sensors, which provide high sensitivity, unique selectivity, long term stability, and reversibility. The most popular luminescent dye materials

used in optical oxygen sensors include complexes of ruthenium, with PL lifetimes $1 \leq \tau \leq 10$ μs, and of platinum (II)- and palladium (II)-porphyrins, with $90 \leq \tau \leq 1200$ μs. In particular, Pt (II) octaethylporphine (PtOEP) and Pd (II) octaethylporphine (PdOEP) are widely used, as their unquenched excited state lifetimes are ~100 and ~1100 μs, respectively.

1.3.4 PL quenching

Collisional quenching of the excited dye molecules by O_2 decreases the PL intensity. During the collision, the triplet dye molecule transfers its energy to O_2, whose ground state is a triplet state, resulting in a singlet dye state and an excited singlet O_2 state. Since the collision process is a physical process rather than a chemical reaction, this PL quenching is reversible, and the sensor films containing the oxygen-sensitive dye can be used to monitor the O_2 level continuously.

1.3.5 PL decay analysis

The luminescence process, with quenching, can be illustrated by:

Dye excitation: $L + h\nu_1 \longrightarrow L^*$ (20)

Dye radiation: $L^* \xrightarrow{K_d} L + h\nu_2$ (21)

Dye-Oxygen Quenching: $L^* + O_2 \xrightarrow{Kq[Q]} L + O_2^*$ (22)

Where L and L^*, O_2 and O_2^* are ground and excited states of luminescence dye molecule and oxygen molecule, respectively. $K_q[Q]$ is the quenching rate constant. K_d is the decay rate constant from L^* to L (exclusive of quenching by O_2), and it includes the radiative and nonradiative decay rate constants K_r and K_{nr}, respectively:

$$K_d = K_r + K_{nr} \tag{23}$$

Let $[L^*]$ be the concentration of L^*. If $\frac{d[L^*]}{dt}$ is proportional to $[L^*]$, then:

$$\frac{d[L^*]}{dt} = -r[L^*] \tag{24}$$

So

$$[L^*](t) = [L^*]_0 e^{-rt} \tag{25}$$

Since the total decay rate constant $r = K_d + K_q[Q]$,

$$\frac{[L^*]}{[L^*]_0} = e^{-(k_d + K_q[Q])t} \tag{26}$$

Because $\tau = \frac{1}{K_d + K_q[Q]}$ and $\tau_0 = \frac{1}{K_d}$, we get

$$\frac{[L^*]}{[L^*]_0} = e^{-t/\tau} \tag{27}$$

and

$$\frac{I(t)}{I_0} = e^{-t/\tau} \tag{28}$$

(see Fig. 7).

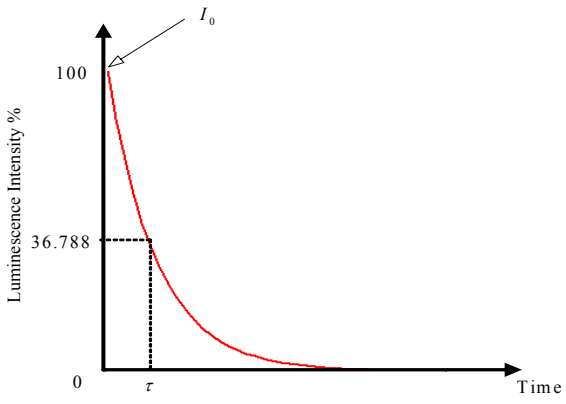

Figure 7. Schematic of single exponential decay.

1.3.6 Stern-Volmer (SV) equation

The PL quantum yield Φ is the ratio of the number of photons emitted to the number absorbed. In terms of the decay rates,

$$\Phi = \frac{K_r[L^*]}{[K_d + K_q[Q]][L^*]} \tag{29}$$

Therefore,

$$\Phi = \frac{K_r}{K_d + K_q[Q]} = K_r\tau \tag{30}$$

Since $\Phi_0 = K_r\tau_0$, we get the SV equation

$$\frac{\Phi_0}{\Phi} = \frac{I_0}{I} = \frac{\tau_0}{\tau} = 1 + K_q\tau_0[Q] \tag{31}$$

Where I_0 and τ_0 are luminescence intensity and decay time in the absence of oxygen, I and τ are luminescence intensity and decay time in the presence of oxygen respectively. Hence, if $K_q\tau_0$ and I_0 or τ_0 are known, the O_2 concentration $[Q]$ can be determined by measuring I or τ.

1.4 Organization of dissertation

This dissertation includes seven chapters. This first chapter is the introduction to OLEDs and structurally integrated OLED-based chemical and biological sensors. The second chapter describes the combinatorial fabrication and study of UV UV-OLEDs. The third chapter describes highly bright white OLEDs based on double hole transport layers and rubrene-doped tris-(4-methyl-8-quinolinolato) Al (III) ($Almq_3$). Structurally integrated organic light emitting device (OLED)-based sensors for hydrazine (N_2H_4) is described in

Chapter 4. Chapter 5 describes structurally integrated OLED-based sensors for gas-phase and dissolved oxygen (DO). Chapter 6 covers the improved oxygen sensors based on dye-doped films containing titania nanoparticles. The final Chapter 7 summarizes this thesis and some resulting conclusions

1.5 Reference:

[1] http://www.answers.com/topic/oled

[2] M. Pope, H. P, Kallmann, and P. Magnante, J. Chem. Phys. **38**, 2042 (1963)

[3] W. Helfrich and W. G. Schneider, Phys. Rev. Lett. **14**, 229 (1965)

[4] P. S. Vincentt, W. A. Barlow, R. A. Hann, and G. G. Roberts, Thin Solid Films **94**, 171 (1982)

[5] C. W. Tang and S. A. VanSlyke, Appl. Phys. Lett. **51**, 913 (1987)

[6] V. Podzorov, S. E. Sysoev, E. Loginova, V. M. Pudalov and M. E. Gershenson, Appl. Phys. Lett. **83**, 3504 (2003)

[7] H. Burroughes, D. D. C. Bradley, A. R. Brown, R. N. Marks, K. Mackay, R. H. Friend, P. L. Burns and A. B. Holmes, Nature **347**, 539 (1990).

[8] U. Mitschke, P. Bäuerle, J. Mater. Chem. **10**, 1471 (2000).

[9] C. Adachi, T. Tsutsui and S. Saito, Optoelectron. Devices Technol. **6**, 25 (1991).

[10] Y.-E. Kim, H. Park, and J.-J. Kim, Appl. Phys. Lett. **69**, 599 (1996).

[11] H. H. Kim, T. M. Miller, E. H. Westerwick, Y. O. Kim, W. Kwock, M. D. Morris, and M. Cerullo, J. Lightwave Technol. **12**, 2107 (1994).

[12] F. Li, H. Tang, J. Anderegg, and J. Shinar, Appl. Phys. Lett. **70**, 1233 (1997).

[13] L. S. Hung, C. W. Tang, and M. G. Mason, Appl. Phys. Lett. **70**, 152 (1997).

[14] Dupont, Dupont OLED, 2006, <http://www2.dupont.com/Displays/en_US/products_services/oled/oled_materials/index.html>

[15] Kodak, Kodak OLED, 2006, <http://www.kodak.com/go/oled>

[16] Universal Display Coporation, OLED display, 2006, <www.universaldisplay.com/>

[17] Samsung, OLED display, 2006, <www.samsung.com/>

[18] LG, OLED display, 2006, <www.lge.com>

[19] General Electric, OLED general illumination, 2006, <www.ge.com>

[20] Philips, OLED general illumination, 2006, <www. Philips.com>

[21] Osram, OLED application, 2006, <www.osram.com>

[22] M. Sampietro, G.Ferrari, D.Natali, M. Arca, C. Denotti and F.A. Devillanova, Proceeding of SPIE, **4943,** 116 (2002).

[23] J. Xue and S. R. Forrest, Appl. Phys. Lett. **82**, 136 (2003).

[24] T. Morimune, H. Kajii and Y. Ohmori, Jpn. J. Appl. Phys. **44**, 2815 (2005).

[25] G. A. Chamberlain, Organic solar cell **8**, 47 (1983).

[26] C. W. Tang, Appl. Phys. Lett. **48**, 183 (1986).

[27] N.S. Sariciftci, L**.** Smilowitz, A.J**.** Heeger, F. Wudl, Science **258**, 1474 (1992).

[28] A. Rose, Z. Zhu, C. F. Madigan, T. M. Swager and V. Bulovic, Nature **434**, 876 (2005).

[29] Z. Zhou, R. Shinar, B. Choudhury, L. B. Tabatabai, C. Liao and J. Shinar, Proceeding of SPIE, **5994** (2005).

[30] R. Shinar, Z. Zhou, B. Choudhury and J. Shinar, Anal. Chim. Acta **568**, 190 (2006).

[31] M. Shtein, J. Mapel, J.B. Benziger, S.R. Forrest, Appl. Phys. Lett. **81**, 268 (2002).

[32] Z. Bao, Adv. Mater., **12**, 227 (2000).

[33] A. J. Lovinger, L. J. Rothberg, J. Mater. Res., **11**, 1581 (1996).

[34] Basic research needs for solid-state lighting, May, 2006.

[35] V. L. Colvin, M. C. Schlamp, A. P. Alivisatos, Nature **370**, 354 (1994).

[36] S. Coe, W. K. Woo, M. Bawendi, V. Bulovic, Nature **420**, 800 (2002).

[37] N. Gaponik, D. V. Talapin, A. L. Rogach, K. Hoppe, E. V. Shevchenko, A. Kornowshi, A. Eychmuller, H. Weller, J. Phys. Chem. B **106**, 7177 (2002).

[38] M. Pope and C. E. Swenberg, Electronic processes in organic crystals and polymers, 2nd edition, Oxford University Press, (1998).

[39] E. H. Rhoderick, Metal-semiconductor contacts, Clarendon Press, Oxford, 1981.

[40] J. G. Simmons, Handbook of thin film technology, Mc Graw-Hill, New York, 1970.

[41] J. H. Schön, C. Kloc, R. A. Laudise and B. Batlogg Phys. Rev. B **58** 12952 (1998).

[42] M. A. Lampert, A. Rose, and R. W. Smith, J. Phys. Chem. Solids **8**, 464 (1959).

[43] H. Bassler, Phys. Stat. Sol. (b) **175**, 15 (1993).

[44] J. C. Scott, S. Karg and S. A. Carter, J. Appl. Phys. **82**, 1454 (1997).

[45] P. Langevin, Annales de Chimie et de Physique, **28**, 289 (1903).

[46] M. Baldo, S. Lamansky, P. E. Burrows, M. E. Thompson, S. R. Forrest, Appl. Phys. Lett. **75**, 4 (1999).

[47] M. Baldo, M. E. Thompson and S. R. Forrest, Nature **403**, 750 (2000).

[48] J. S. Kim, P. K. H. Ho, N. C. Greenham, and R. H. Friend, J. Appl. Phys. **88**, 1073 (2000).

[49] W. Graupner, J. Partee, J. Shinar, G. Leising, and U. Scherf, Phys. Rev. Lett. **77**, 2033 (1996).

[50] R. G. Kepler, Phys. Rev. B **47**, 9253 (1993).

[51] H. Nakanotani, H. Sasabe, and C. Adachi, Appl. Phys. Lett. **86**, 213506 (2005).

[52] N. Oskar, J. Steffen, W. Valerie, B. Erwin, and M. Klaus, Monatshefte fur Chemie **137**, 811 (2006).

[53] Y. Hou, X. Yang, Y.Li and X. Xu, Thin Solid Films **363**, 248 (2000).

[54] S. T. Lee, Z. Q. Gao, L. S. Hung, Appl. Phys. Lett. **75**, 1404 (1999).

[55] J. C. Scott, J. H. Kaufman, P. J. Brock, R. DiPietro, J. Salem, and J. A. Goitia, J. Appl. Phys. **79**, 2754 (1996)

[56] E. Gautier, A. Lorin, J. M. Nunzi, A. Schalchli, J. J. Benettar, and D. Vial, Appl. Phys. Lett. **69**, 1071 (1996)

[57] A. Gyoutokou, S. Hara, T. Komatsu, M. Shirinashihama, H. Iwanaga, and K. Sakanoue, Snth. Mte. **91**, 73 (1997)

[58] A. B. Djurisic, T. Lau, C. Y. Kwong, W. Guo,Y. Bai, E. E. H. Li, W. K. Chan, Proceeding of SPIE, **4464**, 273 (2002).

[59] C. N. Li, C. Y. Kwong, A. B. Djurisic, P. T. Lai, P. C. Chui, W. K. Chan, S. Y. Liu, Thin solid films **477**, 57 (2005)

[60] J. Olivier, B. Servet, M. Vergnolle, M. Mosca, G. Garry, Synthetic Metals, **122**, 87 (2001).

[61] Y. Hashimoto, M. Hamagaki, T. Sakakibara, Jpn. J. Appl. Phys., Part 1, **40**, 4720 (2001).

[62] I. M. Chan and F. C. Hong, Thin Solid Films **444**, 254 (2003).

[63] C. C. Wu, C. I. Wu, J. C. Sturm and A. Kahn , Appl. Phys. Lett. **70**, 1348 (1997)

[64] T. P. Nguyen, P. Le Rendu, N. N. Dinh, M. Fourmigue, C. Meziere, Synt. Met. **138**, 229 (2003).

[65] A. Gyoutoku, S. Hara, T. Komatsu, M. Shirinashihama, H. Iwanaga, K. Sakanoue, Synth. Met. **91**, 73 (1997).

[66] S. A. Van Slyke, C. H. Chen, C. W. Tang, Appl. Phys. Lett. **69**, 2160 (1996).

[67] Y. Shirota, Y. Kuwabara, H. Inada, Appl. Phys. Lett. **65**, 807 (1994).

[68] L. S. Hung, L. R. Zheng, M. G. Mason, Appl. Phys. Lett. **78**, 673 (2001).

[69] W. Hu, K. Manabe, T. Furukawa, M. Matsumura, Appl. Phys. Lett. **80**, 2640 (2002)

[70] M. B. Huang, K. McDonald, J. C. Keay, Y. Q. Wang, S. J. Rosenthal, R. Weller, and L. C. Feldman, Appl. Phys. Lett. **73**, 2914 (1998).

[71] H. Aziz, Y. F. Liwe and Z. popovic, Proceedings of the SPIE conference, Organic Light emitting materials and devices VII; San Diego, CA, July (2003).

[72] M. Schaer, F. Nüesch, D. Berner, W. Leo, and L. Zuppiroli, Adv. Funct. Mater. **11**, 116 (2001).

[73] D. Kolosov, D. S. English, V. Bulovic, P. .F Barbara, S. R. Forrest and M. Thompson, J. Appl. Phys. **90**, 3242 (2001).

[74] S. Jeong, W. Koo, S. Choi, S. Jo, H. Baik, S. Lee and K. Song, Thin Solid Films **475**, 227 (2005).

[75] M. K. Fung, Z. Q. Gao, C. S. Lee, S. T. Lee, Chem. Phys. Lett. **333**, 432 (2001).

[76] H. Aziz, Z. Popovic, S. Xie, A. Hor, N. Hu, C. Tripp, G. Xu, Appl. Phys. Lett. **72**, 756 (1998).

[77] S. Park, J. Oh, C. Hwang, J. Lee, Y. Yang and H. Chu, Electrochem. Solid-State Lett., **8**, H21 (2005).

[78] K. Yamashita, T. Mori1 and T. Mizutani, J. Phys. D: Appl. Phys. **34**, 740 (2001).

[79] P. E. Burrows, V. Bulovic, S. R. Forrest, L. S. Sapochak, D. M. McCarty, and M. E. Thompson, Appl. Phys. Lett. **65,** 23 (1994).

[80] H. Biebuyck, E. Haskal, US Patent 5,895,228

[81] Barix, encapsulation technique, 2005, <http://www.barix.com/>

[82] Vadim N. Savvate'ev, Aharon V. Yakimov, and Dan Davidov, Roman M. Pogreb, Ronny Neumann, Yair Avny, Appl. Phys. Lett. **71**, 3344 (1997).

[83] H. Spreitzer,H. W. Schenk, J. Salbeck, F. Weissoertel, H. Reil,W. Riess, Proceedings of SPIE **3797**, 316 (1999).

[84] V. I. Adamovich, M. S. Weaver, R. C. Kwong and J. J. Brown, current applied physics **5**, 15 (2005).

[85] Tomohiko Mori, Takuya Mitsuoka, Masahiko Ishii, Hisayoshi Fujikawa, and Yasunori Taga, Appl. Phys. Lett. **80**, 3895 (2002).

[86] H. Aziz, Z. D. Popovic, N. X. Hu, A. M. Hor, G. Xu, Science **283**, 1900 (1999).

[87] J. Shi, C. W. Tang, Appl. Phys. Lett. **70**, 1665 (1997).

[88] A. Bohler, S. Dirr, H. H. Johannes, D. Ammermann, and W. Kowalsky, Synth. Met. **91**, 95 (1997)

[89] M. Matsumura, Y. Jinde, Synth. Met. **91**, 197 (1997)

[90] H. Aziz, Z. D. Popovic, N. Hu, A. Hor, G. Xu, Mater. Res. Soc. Symp. Proc. **558**, 507 (2000).

[91] J. R. Lakowicz, Principles of Fluorescence Spectroscopy, 2nd edition, Kluwer Academic/Plenum Publishers, 10 (1999).

Appendix: Color coordinates

Color coordinates were standardized by the (Commission Internationale de l'Eclairage (CIE)). The sensation of color in nature is usually quantified by the combination of three primary colors (stimuli), such as red (R), green (G) and blue (B). The tristimulus values (*X*, *Y*, and *Z*) can be calculated by measuring the illumination spectral density $S(\lambda)$ and tristimulus response of the color receptive cells---color-matching functions $\bar{x}(\lambda), \bar{y}(\lambda)$ and $\bar{z}(\lambda)$ (see Figure 1).

$$X = \int \bar{x}(\lambda) S(\lambda) d\lambda ,$$

$$Y = \int \bar{y}(\lambda) S(\lambda) d\lambda ,$$

$$Z = \int \bar{z}(\lambda) S(\lambda) d\lambda .$$

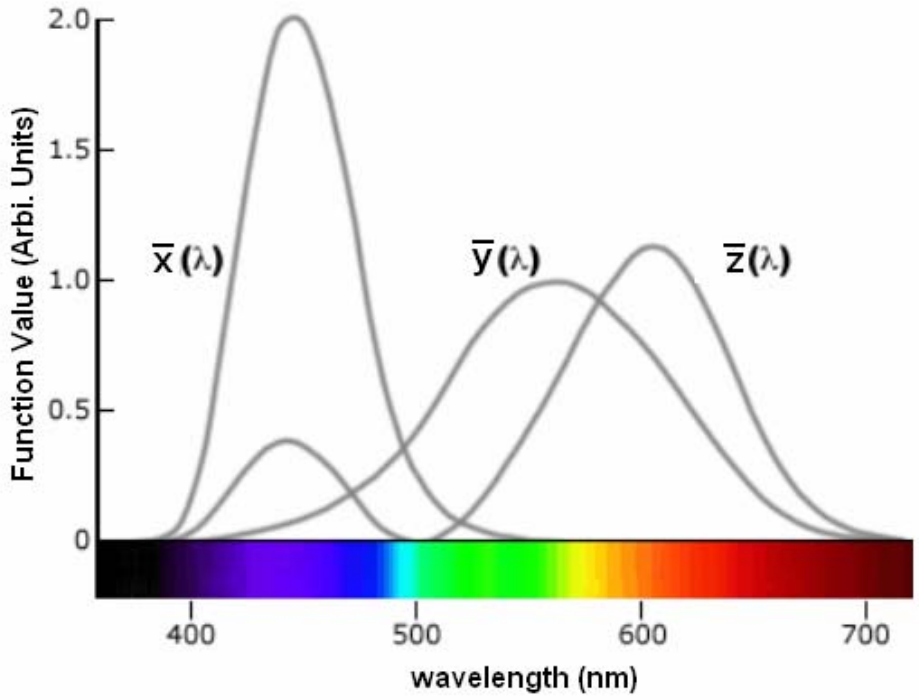

Figure 1. 1931 CIE color-matching functions

Then the color coordinates of a light source with a spectrum $S(\lambda)$ can be described by:

$$x = \frac{X}{X+Y+Z}$$

$$y = \frac{Y}{X+Y+Z}$$

$$z = \frac{Z}{X+Y+Z} \equiv 1 - x - y$$

Normally, the z value contains no additional information. Therefore, an in-plane description of colors can be made by CIE chromaticity diagram.

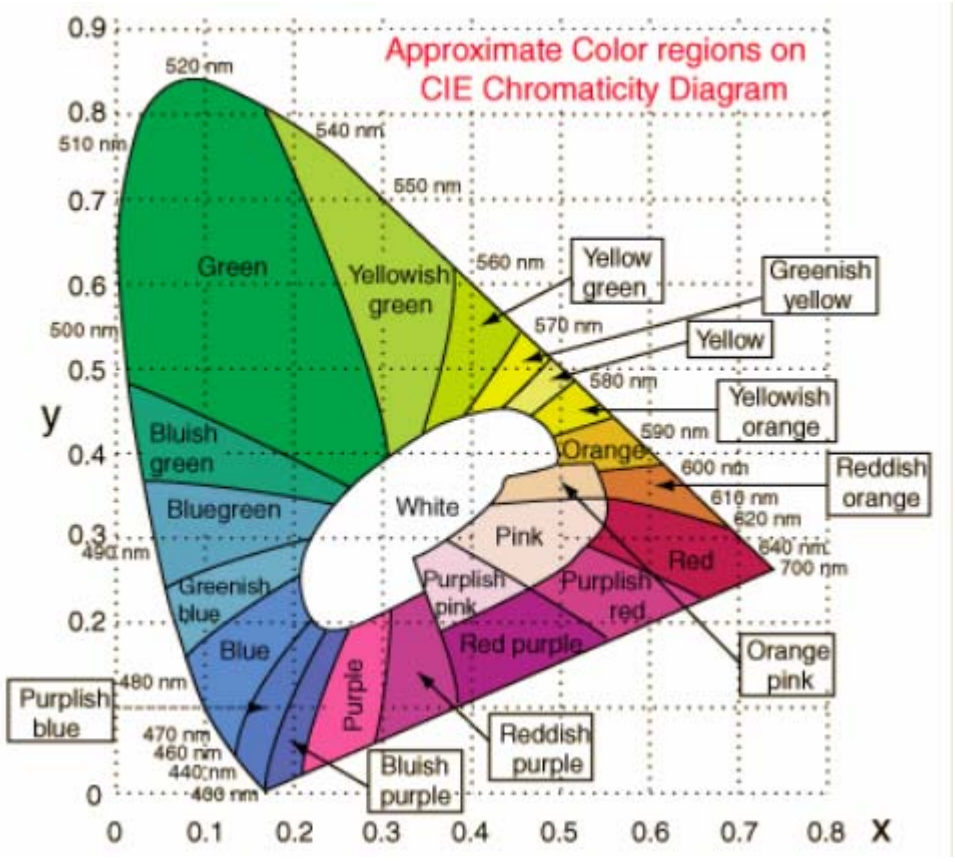

Figure 2. 1931 CIE chromaticity diagram.

2. COMBINATORIAL FABRICATION AND STUDY OF ULTRAVIOLET ORGANIC LIGHT EMITTING DEVICES (UV-OLED)

Abstract

UV-violet OLEDs based on ITO/[copper phthalocyanine]/[4,4'-bis(9-carbazolyl)biphenyl]/[bathocuproine]/CsF/Al, with a peak emission at ~380 nm, were fabricated and optimized using a single-batch combinatorial fabrication. The optimal device had a peak radiance of 20 W/m^2 at 500 mA/cm^2 with CBP and BCP thicknesses of 500 $\mathring{A}$ and 250 $\mathring{A}$, respectively. The maximum luminance was 142.9 Cd/m^2 at 11.74 V. Adding a thin layer (1.5 nm) of NPB as hole transport layer was sufficient to degrade the UV emission. This UV performance deterioration is due to energy transfer from the wide band-gap CBP to NPB; it limits the choice of HTL materials that are usable for enhancing such UV-OLEDs.

2.1 Introduction

Visible OLEDs from blue [1-3] to red [4, 5] have improved significantly in efficiency and brightness since the fabrication of the first thin-film OLEDs by Tang and VanSlyke in 1987 [6]. However, UV-OLEDs have received much less attention. In fact, UV light emitting devices are of great importance in e.g., photoluminescence-based chemical and biological sensors [7, 8], and UV-OLEDs as excitation sources in such sensors can lead to compact, efficient, and field-deployable sensors for a wide variety of analytes. UV-OLED fabrication was reported by Yuan *et al* [9] who used poly[bis(*p*-butylphenyl)silane] (PBPS) to generate near UV OLEDs with peak emission at 407 nm. Qiu *et al* [10] fabricated 400 nm thick OLEDs by using *N*, *N*'-diphenyl-*N*, *N*'-bis(3-methylphenyl)-(1,1'-biphenyl) -4,4'-diamine

(TPD) with GaN. The maximum luminance was only ~60 *lm*. Moreover, the fabrication was complicated, with the TPD and GaN layers deposited alternatively twice. Although Zou *et al* [11] fabricated CuPc/[4,4′-bis(9-carbazolyl)biphenyl (CBP)]/[2-(4-Biphenylyl)-5-(4-tert-butylphenyl)-1,3,4-oxadiazole (Bu-PBD)] UV-OLEDs,, with peak CBP emission at 380 nm, the emission spectrum of these devices was not stable due to the low thermal stability of Bu-PBD.

This chapter describes a combinatorial approach to optimize the CBP-based UV-OLEDs by replacing the Bu-PBD with the more stable hole-blocking bathocuproine (BCP) layer, and systematically changing the thicknesses of the CBP and BCP in the CuPc/CBP/ BCP devices. Thus, the BCP layer served two purposes: (i) to block holes from drifting past the emitting CBP layer and reaching the cathode, and thus to confine the excitons to the emission layer, preventing their quenching by the cathode, and (ii) to serve as the electron transport layer, and thus contribute to balancing hole-electron recombination and optimizing the efficiency. The optimal thicknesses of CBP and BCP were determined to be 50 nm and 25 nm, respectively; the maximal luminance was 449 *lm*. In addition, attempts to improve the UV-OLED by adding 4,4'-bis[N-(1-naphthyl)-N-phenyl-amino]biphenyl (α-NPD) as a hole transport layer (HTL) failed, indicating that the choice of HTL materials for wide band gap UV-OLEDs is limited.

2.2 Device structure and experimental procedure

The molecular structures of CBP, BCP, the energy band diagram of the OLED, and its structure, are shown in Fig. 1. The OLEDs were fabricated on: glass substrates pre-coated with ~140 nm of ITO (Applied Films Corporation; sheet resistance 20Ω/square. The ITO

was first cleaned with a surfactant in an ultrasonic bath, and then rinsed in flowing de-ionized water, followed by acetone and iso-propanol to remove dust and organic residue. Next, the cleaned ITO substrate was transferred to a vacuum chamber, where it was dried using argon.

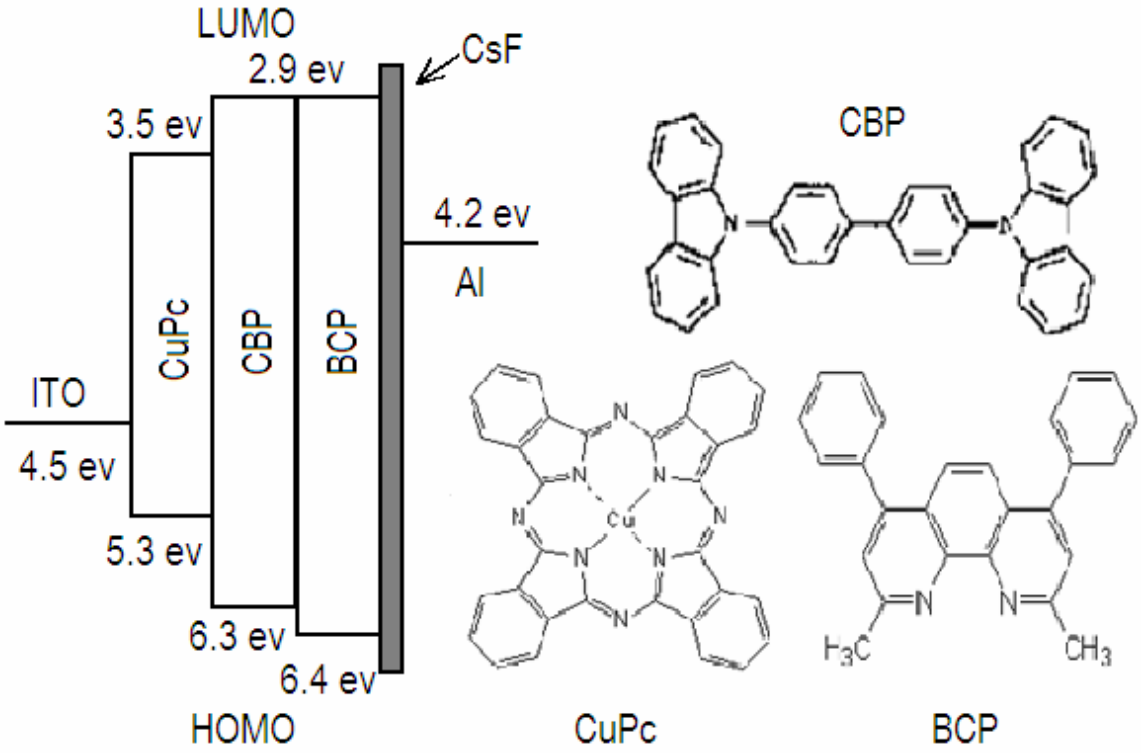

Figure 1. Molecular structures, the HOMO and LUMO energy band diagrams of organic materials, and the device structure.

The vacuum chamber is installed in a glove box in which the oxygen and water levels are generally below 1 ppm. The OLED layers were deposited by thermal evaporation, using a tungsten-heating basket. The evaporation rates of the organic materials and the cathode were 1-2 Å/s and 4-5 Å/s, respectively. The vacuum background in the chamber was around 2×10^{-6} mbar. The thickness of the organic layers was measured with a quartz crystal thickness monitor, which is installed 30 cm above the organic source.

The OLEDs were biased using a Kepco programmable power supply DPS 40-2M. The EL intensity was measured by a Hamamatsu R6060 photomultiplier tube (PMT). The EL spectra were measured using an Ocean Optics CHEM2000 spectrometer. In order to calculate the radiance of the OLEDs, a Minolta LS110 luminance meter was used. It is important to note that generally the luminance meter is mostly sensitive to the visible light; the spectral responsivity of the luminance meter for UV light is very low.

To obtain the optimal structure of the UV-OLED, the same combinatorial method, using a sliding shutter [11] was used. A 5×5 matrix of OLED array with ~1.5 mm diameter pixels in one batch was fabricated. This approach resulted in 25 different structures (combinations of CBP thicknesses of 5, 20, 35, 50, and 65 nm, and BCP thicknesses of 5, 15, 25, 35, and 45 nm). The CuPc layer was 12.5 nm thick in all of the devices. In order to improve electron injection from the cathode, a 1 nm-thick CsF buffer layer was deposited on the BCP. The ~150 nm thick Al cathode was deposited immediately after the CsF.

2.3 Results and discussion

Fig. 2 shows that the EL changes as the thickness of BCP and CBP varies. From Fig. 2(a), it is seen that the optimal thickness of CBP is 50 nm when the thickness of BCP is fixed at 25 nm. The emission originates in the CBP layer near the interface of CBP and BCP. A CBP layer that is too thin leads to imbalanced electron-hole pair recombination and an insufficient recombination zone, while a layer that is too thick leads to an insufficient electric field and a lower efficiency.

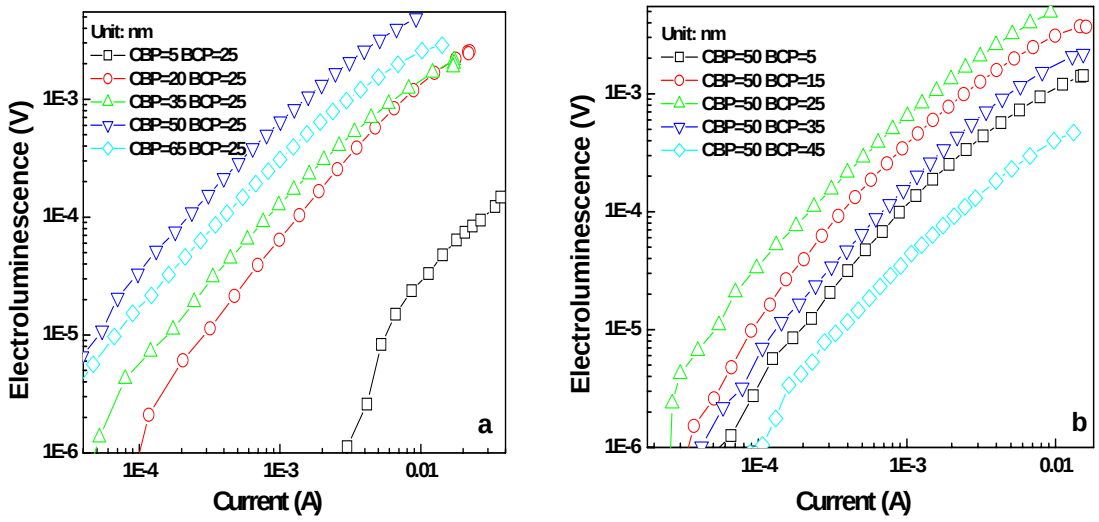

Figure 2. (a) The EL of the OLEDs vs the current at various thicknesses of CBP; (b) The EL of the OLEDs vs the current at various thicknesses of BCP.

As clearly seen in Fig. 2(b), the optimal thickness of BCP is 25 nm when the CBP thickness is kept constant at 50 nm. This optimal value is likely due to the following competing effects: (i) a thinner BCP layer cannot effectively block hole transport from CBP to the cathode, while (ii) a thicker BCP layer will result in a decrease in the electric field in the organic layer, which will decrease the EL. The three-dimensional radiance map in Fig. 3 also clearly shows that the optimal thicknesses of the CBP and BCP layers are 50 nm and 25 nm, respectively.

The highest radiance of 20 W/m^2 is obtained in the optimal device at a current density of 500 mA/cm^2. The response curve of the luminance meter is designed to match the human eye's sensitivity, ~~s~~o there is only a very small part of overlap between the UV-OLED spectrum and the response curve of the luminance meter. However, we can use this small overlap to extrapolate the total radiance of the UV-OLEDs.

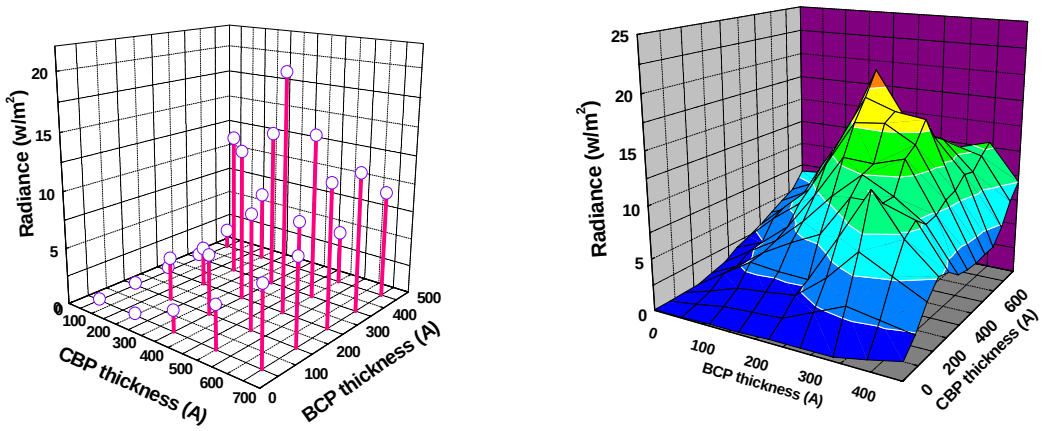

Figure 3. Three dimensional radiance maps at current density *J*=500 mA/cm^2.

Using the optimal thicknesses of CBP and BCP, the spectrum of optimal device peaked at 380 nm, which is among the shortest wavelength OLEDs reported to date. With changes in the voltages, the spectrum remains largely unchanged, probably due to the good thermal stability of BCP [12]. The full width at half maximum (FWHM) is ~45 nm. We also compared the UV-OLED with BCP to those with Bu-PBD based described earlier [11]. The spectra of these two devices are shown in Fig. 4. It is obvious that the devices with Bu-PBD are not stable when the applied voltage increases from 11 V to 19 V. The peak spectrum shifts by more than 70 nm when the voltage is changed in this range. In contrast, those with BCP are relatively stable, with the peak shifting by less than 8 nm when the applied voltage increases from 8 V to 19 V.

Finally, we consider the potential contribution of NPB, normally considered as one of the best HTLs in OLEDs, to these UV-violet OLEDs. However, this approach is not suitable for the CBP-based UV-OLEDs. The addition of an NPB HTL did not increase the efficiency of the devices. Indeed, as seen in Fig. 5, addition of a very thin layer of NPB (1.5 nm)

reduces the emission, and a 440 nm emission, originating from the NPB, is observed.

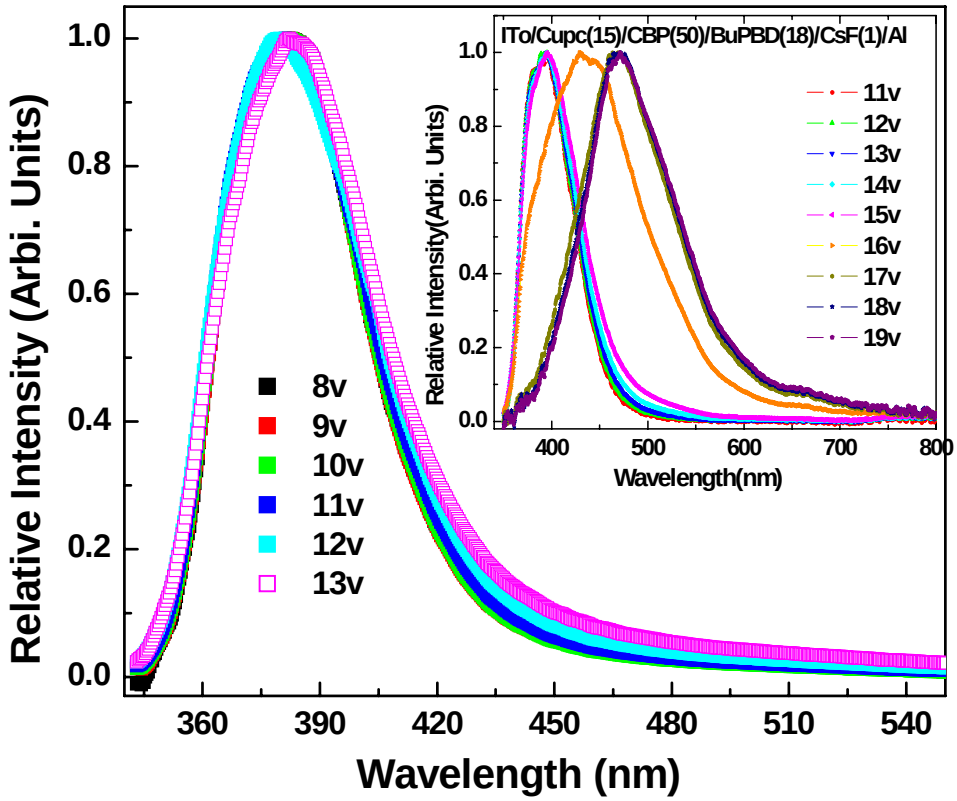

Figure 4. Spectra of BCP UV-OLEDs at different voltages. Inset is spectra of Bu-PBD UV-OLEDs.

As seen in Fig. 1, the energy levels of the CBP's highest occupied and lowest unoccupied molecular orbital [8] (HOMO, LUMO, respectively) are 6.3 and 2.9 eV, respectively, while the HOMO and LUMO of NPB are 5.2 eV and 2.2 eV respectively. Due to the large energy difference (1.1 eV) between the HOMO levels of NPB and CBP. Therefore, adding NPB results in hole accumulation in the NBP layer adjacent to the CBP. Thus, even for an NPB layer as thin as 1.5 nm, NPB emission is observed. This is also due to

the higher sensitivity of the eye to the blue emission of NPB, rather than the UV-violet emission from CBP.

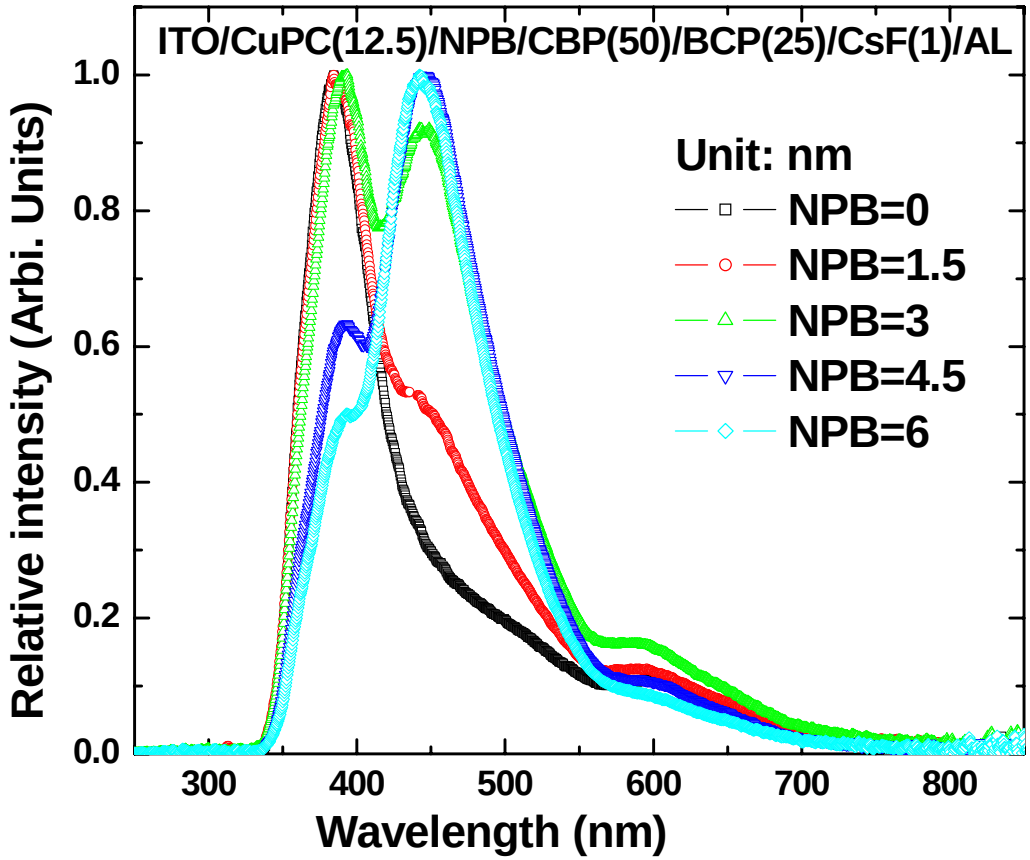

Figure 5. Spectra of UV- OLEDs with different thicknesses of NPB.

2.4 Conclusion

In summary, we fabricated and optimized UV-violet OLEDs by using a sliding shutter combinatorial fabrication technique. The optimal thicknesses of CBP and BCP were 50 and 25 nm, respectively. The peak emission of the optimized device was at ~380 nm. The maximal radiance of 20 W/m^2 was obtained at 500 mA/cm^2. The optimal structure can be clearly seen from the three dimensional radiance maps. Adding the conventional HTL NPB

reduced the UV-violet emission due to the large barrier for hole injection from NPB (E_{HOMO} = 5.2 eV) to CBP (E_{HOMO} = 6.3 eV). This also highlights the limited choice of HTL materials for UV-violet OLEDs in general.

2.5 References

[1] C. Adachi, T. Tsutsui, and S. Saito, Appl. Phys. Lett. **56**, 799 (1990).

[2] C. Hosokawa, N. Kawasaki, S. Sakamoto, and T. Kusumoto, Appl. Phys. Lett. **61**, 2503 (1992).

[3] H. Tokailin, H. Higashi, C. Hosokawa, and T. Kusumoto, Proc. SPIE **1910**, 38 (1993).

[4] M. A. Baldo, D. F. O'Brien, Y. You, A. Shoustikov, S. Sibley, M. E. Thompson and S. R. Forrest, Nature **395**, 151 (1998).

[5] A. Shoustikov, Y. J. You, P. E. Burrows, M. E. Thompson and S. R. Forrest, Synthetic Met. **91**, 217 (1997).

[6] C. W. Tang and S. A. Van Slyke, Appl. Phys. Lett. **51**, 913 (1987).

[7] V. Savvate'ev, Z. Chen-Esterlit and J. W. Aylott, B. Choudhury, C.-H. Kim, L. Zou, J. H. Friedl, R. Shinar, J. Shinar and R. Kopelman, Appl. Phys. Lett. **81**, 4652 (2002).

[8] Y. Amao, K. Asai, T. Miyashita and I. Okura, Chem. Lett. **10**, 1031 (1999).

[9] C. H. Yuan, S. Hoshina, S. Toyoda, H. Suzuki, M. Fujiki, and N. Matsumoto, Appl. Phys. Lett. **71**, 3326 (1997).

[10] C. F. Qiu, L. D. wang, H. Y. Chen, M. Wong, and H. S. Kwok, Appl. Phys. Lett. **79**, 2276 (2001).

[11] L. Zou, V. Savvate'ev, J. Booher, C. H. Kim, and J. Shinar, Appl. Phys. Lett. **79**, 2282 (2001).

[12] M. A. Baldo and S. R. Forrest, Physical Review B **62**, 10958 (2000).

[13] M. A. Baldo , S. Kamansky, P. E. burrows, M. E. Thompson and S. R. Forrest, Appl. Phys. Lett. **75**, 4 (1999).

[14] U. Mitschke and P. Bäuerle, J. Mater. Chem. **10**, 1471 (2000).

[15] C. Adachi, S. Tokito, T. Tsutsui and S. Saito, Jpn. J. Appl. Phys. **27**, L269 (1988).

[16] C. Adachi, T. Tsutsui, and S. Saito, Appl. Phys. Lett. **55**, 1489 (1989).

3. HIGHTLY BRIGHT WHITE ORGANIC LIGHT-EMITTING DIODES BASED ON DOUBLE HOLE TRANSPORT LAYERS AND RUBRENE-DOPED TRIS (4-METHYL-8-QUINOLINOLATO) ALUMINUM (III) ($ALMQ_3$)

Abstract

Very bright and highly efficient white organic light-emitting diodes (WOLEDs) are described. The WOLED's structure is ITO/ [4,4',4''-tris[2-naphthyl(phenyl)amino] triphenylamine (2-TNATA)] / NPB / [4,4'-bis(2,2'-diphenylvinyl)-1,1'-biphenyl (DPVBi)] / [0.5% rubrene): tris(4-methyl-8- quinolinolato)aluminum(III) (Almq3)] / $Almq_3$ / CsF / Al. Changing the thickness of the rubrene doped $Almq_3$ layer, a maximal brightness of 79100 Cd/m^2 at 11 V, and maximal luminance efficiency 9.0 Cd/A and maximal power efficiency 6.4 lm/W at 4.4 V, 56 Cd/m^2, and 0.62 mA/cm^2, corresponding to a maximal external quantum efficiency of 4.5% was obtained The color coordinates of the WOLEDs were quite stable at voltages ranging from 4 to 11 V. Double hole-transport layers 2-TNATA and NPB improved hole injection, enhanced the durability of EL device, and eliminated the leakage current that results from morphological defects. The high efficiency was attributed to the rubrene doped into the highly efficient fluorescent $Almq_3$; the turn on voltage (the bias at 1 Cd/m^2) was 2.9 V.

3.1 Introduction

Since the first thin-film OLED was reported by C. W. Tang and S. A. VanSlyke in 1987 [1], WOLEDs have attracted growing attention not only as back lights in liquid crystal displays (LCDs) [2] and in active matrix displays (with color filters), but also as general light

sources [3, 4]. Compared with inorganic white LED, WOLEDs enjoy advantages such as large flexible thin lightweight substrates, and easy and cheap fabrication. To obtain white organic EL, a variety of techniques were used, such as overlapping three different layers emitting three primary colors individually [5], doping a luminescent dye into the emitting layer to get efficient energy transfer from host to guest, or using trapping centers, which leads to the emission from the dye [6, 7]. Since the spectra of organic molecules are usually broad, it is possible to obtain white light through superposing yellow and blue emission. Other ways to make WOLED are exciplex emission [8], microcavity technique [9], multiple-quantum wells structures [10], and a blend of several different fluorescent dyes with host material by fused organic solid solution [11]. However, the efficiency of most of the resulting devices is low and their color stability to applied voltage changes is poor. In addition, high brightness WOLEDs are required in many special uses [12].

3.2 Device structure and experiment

In this letter, we report the fabrication and performance of very bright and highly efficient thermally evaporated small molecular WOLEDs. The double hole transport layer (4,4',4''-tris[2-naphthyl(phenyl)amino] triphenylamine (2-TNATA)/ N,N'-diphenyl-N,N'-bis(1-naphthyl phenyl)-1,1'-biphenyl-4,4'-diamine (α-NPD) was used in this white OLED fabrication. As a starburst π-electron, 2-TNATA not only has a high glass transition temperature (T_g = 110^{o}C) but also forms morphologically smooth, uniform amorphous films by vacuum evaporation [13], which prevents leakage currents due to the pinholes that occur in non-uniform film. The relatively shallow 5.1 eV HOMO level of 2-TNANA, also benefits hole injection from ITO, since the work function of ITO is typically 4.5 - 4.9 eV [14]. In

addition, adding the NPB HTL (E_{HOMO} = 5.2 eV) prevents exciplex formation between 2-TNATA and 4,4'-bis(2,2'-diphenylvinyl)-1,1'-biphenyl (DPVBi), and it enhances the hole injection efficiency by a stepwise process.

The emission layers were the blue emitting DPVBi and yellow-emitting layer of 0.5% rubrene-doped $Almq_3$. The PL quantum efficiency η_{PL} of $Almq_3$ is about twice that of Alq_3 [15], and the fluorescent dye rubrene has η_{PL} = 100% in dilute solutions or when lightly doped in a host matrix [16]. The high η_{PL} host combined with the high η_{PL} guest result in a high EL efficiency. The maximal power and luminous efficiencies were 6.41 lm/W, 8.95 Cd/A, respectively, at 4.4 V, 0.62mA/cm^2 and 56 Cd/m^2, corresponding to a maximal external quantum efficiency η_{ext} = 4.5%. The color coordinates (see appendix in chapter 1) of the WOLEDs at this driving voltage were x = 0.39, y = 0.44. The highest brightness obtained was 79100 Cd/m^2, which is the brightest fluorescent white OLED reported to date.

3.3 Results and discussion

Figure 1 shows the molecular structures of the organic materials used in the WOLED fabrication and the side view structure of the WOLEDs. The organic layers were deposited on 2"×2" Colorado Concept Coatings LLC ITO-coated glass substrates. The ~140 nm-thick ITO sheet resistance was $R \sim 20\ \Omega$. The ITO was wet scrubbed by using acetone to remove dust on the surface, followed by ultrasonic cleaning in surfactant for 15 minutes, then rinsing the substrate for 15 min with flowing distilled water and repeated ultrasonication in acetone and 2-propanol for 3 min, respectively. After 5 min of UV-ozone (UVOCS INC. Model: T16X16/0ES) treatment to remove the organic residues, the substrate was moved

immediately into the evaporation chamber located in a glove-box with oxygen and water levels generally below 1ppm.

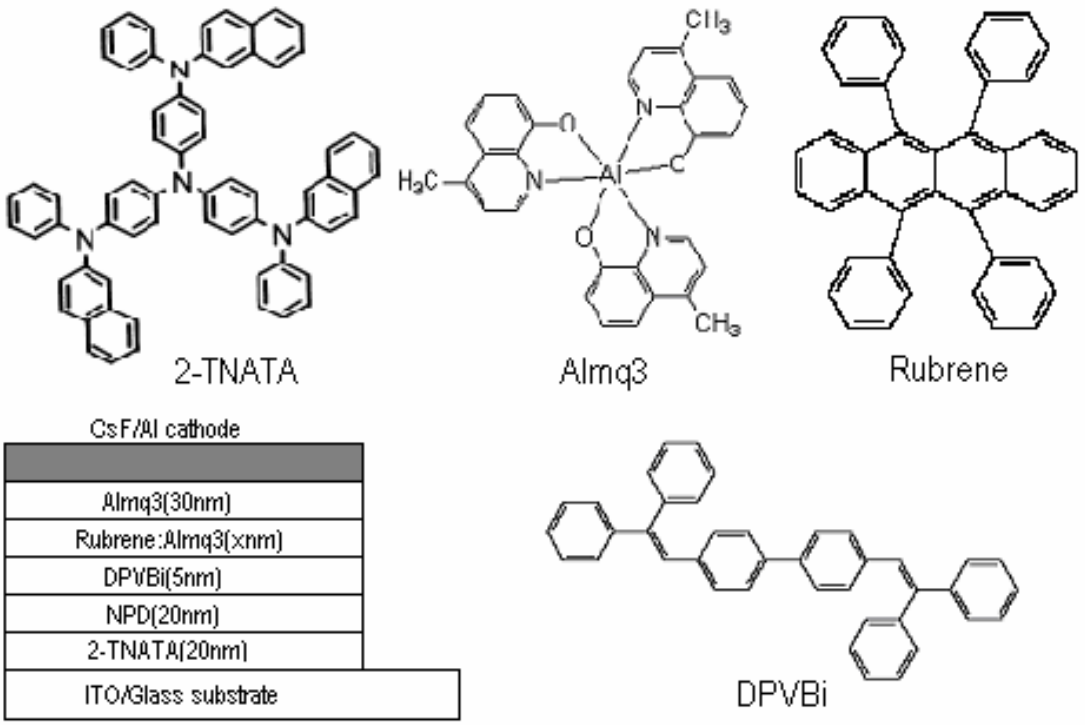

Figure 1. Molecular structures of the materials and the side view of the device.

All the organic materials were thermal evaporated with resistively heating tantalum coils at a background pressure of 2×10^{-6} mbar. The organic materials and Al cathode were deposited at 0.1 - 0.2 nm/s and 0.4 nm/s, respectively. The first layers deposited on the ITO were 20 nm 2-TNATA, 20 nm NPB, and 5 nm DPVBi. Using the sliding shutter technique [17], the thickness of the rubrene doped $Almq_3$ was varied from 2 to 10 nm in 2 nm steps. Following that layer, another 30 nm $Almq_3$ layer was deposited as an ETL, followed by the 1 nm CsF buffer layer and the 150 nm-thick Al layer.

All the current and voltage were obtained by Kepco programmable power supply DPS 40-2M. Luminance was obtained from Minolta LS110 luminance meter. Spectra of emitting devices were measured by Ocean Optics CHEM2000 spectrometer. All the

measurements were carried out at room temperature under ambient conditions, and the devices were exposed to air only while being tested.

Table 1 summarizes the performance of the different WOLEDs. As clearly seen, device A exhibited the highest luminous power efficiency of 6.4 lm/W, while device B exhibited the highest brightness, 79100 Cd/m^2. All the devices exhibited maximal brightnesses > 60000 Cd/m^2. Their impressive performance was probably due to good film formation of each organic layer and its high T_g. The turn on voltage (defined as the bias at 1 Cd/m^2) for device E was only 2.9 V, and its color coordinates (0.32, 0.38) were well within the white region. Indeed, the coordinates of all the WOLEDs in this study at 2000 Cd/m^2 were very close to the perfect white point (0.33, 0.33).

Table 1. The thickness of rubrene doped $Almq_3$ layer, the applied currents and brightness for maximum luminance efficiency, power efficiency, CIEs at maximum efficiency, L_{max} of the OLEDs, and CIEs at brightness of 2000 Cd/m^2.

	Doping thickness (nm)	Max. η_{LE} (Cd/A)	Max. η_{PE} (lm/W)	J (mA/cm^2)	L Cd/m^2	Color coordinates (x , y)	L_{max} Cd/m^2	CIE at L=2000 Cd/m^2
Device A	10	9.0	6.4	0.62	56	(0.39,0.44)	62080	(0.34,0.38)
Device B	8	6.7	5.1	0.52	35	(0.34,0.38)	79100	(0.29,0.33)
Device C	6	7.1	5.3	0.59	42	(0.34,0.39)	74120	(0.29,0.32)
Device D	4	7.0	5.2	0.73	50	(0.32,0.36)	76260	(0.29,0.32)
Device E	2	7.3	5.5	1.25	92	(0.30,0.35)	65910	(0.27,0.31)

Figure 2 shows the luminance and current density of the devices under different bias. As the thickness of rubrene doped layer decreased, the turn on voltages decreased from 3.06 V for device A to 2.9 V for device E. The color coordinates of all the devices were well within the white region at all brightness levels. The maximal luminance of devices A to E

were 62100 (at 10.7 V, 2.45A/cm^2), 79100 (at 11.0 V, 3.32 A/cm^2), 74120 (at 10.7 V, 3.24 A/cm^2), 76260 (at 10.5 V, 3.27 A/cm^2) and 65910 (at 10.28 V, 2.82 A/cm^2) respectively. At high current density (J > 1 A/cm^2), $J(V)$ did not follow trap-free space charge limited current (SCLC) behavior, probably because the glass substrate couldn't effectively dissipate the heat due to the very high current and bad thermal conductivity of the glass. Within the high J region, singlet-heat annihilation (SHA) would dominate the organic material electronic process [18], which is one of the major reasons leading to the efficiency roll-off at high J.

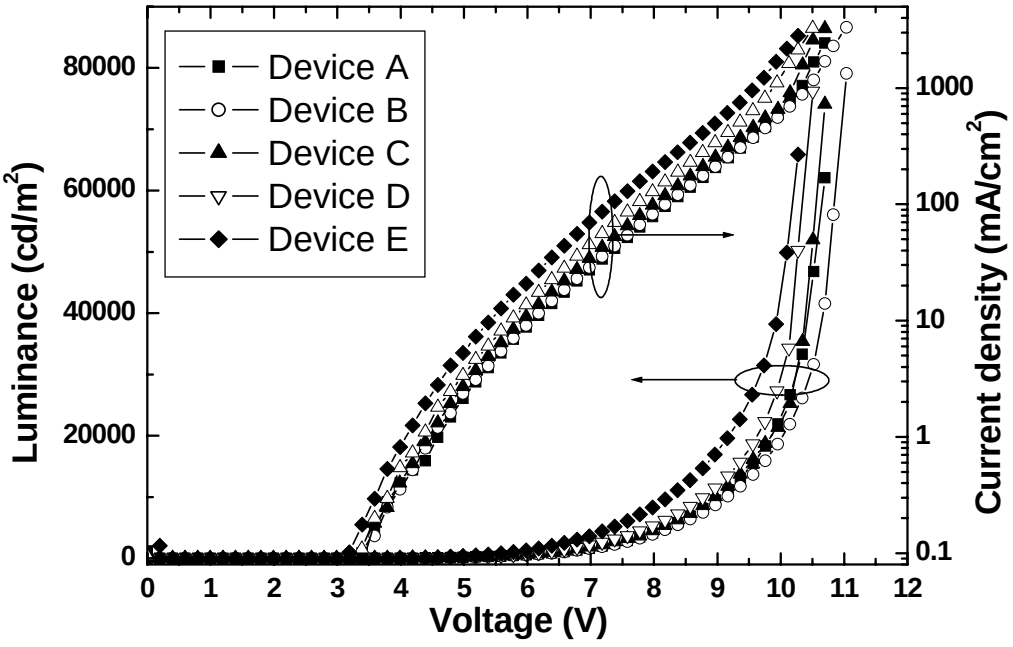

Figure 2. $J(V)$ and $L(V)$ curves of the WOLEDs at different voltages.

The power efficiency and luminance efficiency are shown in Figure 3. All the devices exhibited more than 5 lm/W power efficiency and 6 Cd/A for luminous efficiency. For device A, the maximal power efficiency 6.41 lm/W and luminous efficiency 8.95 Cd/A (corresponding to external quantum efficiency 4.5%) occurred at L = 56 Cd/m^2, J = 0.62

mA/cm^2, and 4.4 V. The color coordinates at the highest efficiency were all well within the white region. The decreased EL efficiency with the increasing current density, especially at higher *J*, was attributed to the singlet-singlet annihilation and singlet-heat annihilation [18].

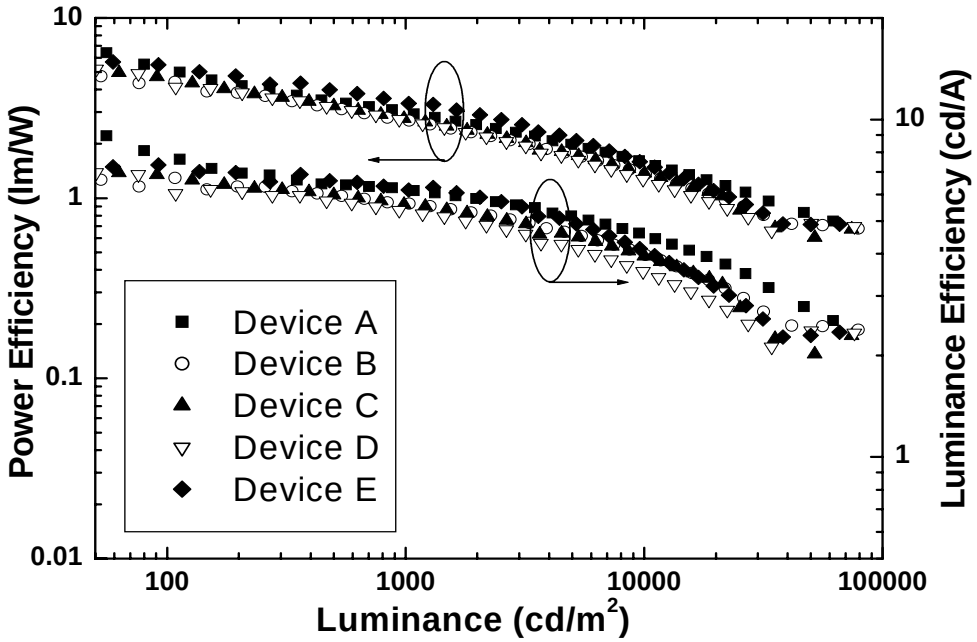

Figure 3. Power efficiency and luminance efficiency of the WOLEDs at different brightness.

Figure 4A shows the spectra of device B, which gave the highest brightness at 79,100 Cd/m^2, and color coordinates at different applied bias. At lower voltage, the emission coming from rubrene doped $Almq_3$ overweighed the blue emission from DPVBi. Since rubrene is a well-known carrier-trapping material, most electrons are trapped at low driving current.

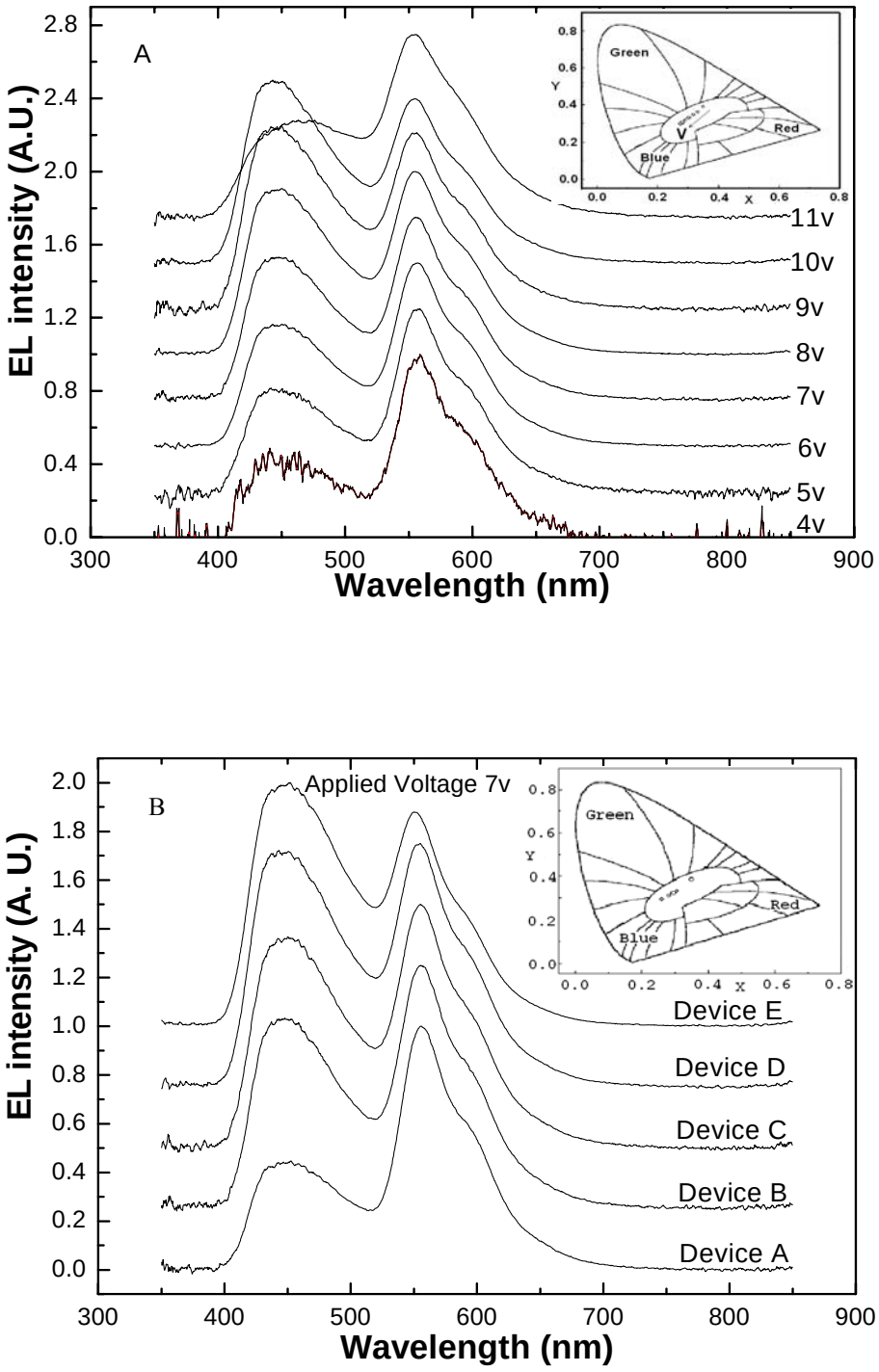

Figure 4. (A) Spectra of device B at different bias and their CIEs. (B) Spectra of different devices at bias 7v and their CIEs.

Electrons then recombine with holes on the rubrene molecules and emit yellow light. A small fraction of the electrons recombine with holes on the DPVBi molecule, yielding the blue emission band. Hence the total emission from device at lower current is a yellowish white light. Increasing the applied voltage, more and more electrons reach the DPVBi molecules and recombine with holes, leading to stronger blue emission. Once the yellow emission from rubrene is saturated, the blue emission overbalances the yellow emission resuting in a bluish white light. From figure 4A, the color coordinates of device B changed from yellowish-white (0.39, 0.35) at 4V, to bluish white (0.27, 0.30) at 10 V. From J = 0.35 mA/cm^2 at 4 V to J = 598 mA/cm^2 at 10 V, the color coordinates changed by only 14%, despite the 1500-fold increase in J.. It is worth mentioning that the breakdown of the WOLEDs was due to "the weakest link" DPVBi layer, as it has the lowest T_g = 64^{0}C among all the layers in these WOLEDs. This conclusion is confirmed by Figure 4A, as it is clear that at 11 V device B lost some of its blue emission relative to the yellow emission from rubrene. This observation leads to the conclusion that the brightness of the WOLEDs could increase if the DPVBi were replaced by a higher T_g material, e.g., Spiro-DPVBi.

Figure 4B shows the spectra and color coordinates of different devices at 7 V. It is obvious that the blue emission strengthens as the thickness of the rubrene-doped Almq$_3$ layer decreases. Considering the ~5 nm recombination zone and the carrier trapping properties of rubrene, the blue DPVBi emission increases once the rubrene-doped layer is reduced to a sufficiently thin layer.

The inset of Figure 4B shows the color coordinates of all the devices at 7 V. As expected, as the rubrene-doped layer became thinner, the color coordinates change from (0.34,0.39) for device A to (0.26, 0.30) for device E.

3.4 Conclusion

In conclusion, we fabricated and studied highly bright and efficient fluorescent WOLEDs with good color stability over a wide range of current density and brightness. By changing the thickness of a rubrene doped $Almq_3$ layer we achieved the highest brightness of 79100 Cd/m^2. The maximal luminance and power efficiencies were 9.0 Cd/A and 6.4 lm/W, respectively, at J = 0.62 mA/cm^2 and luminance of 56 Cd/m^2. The 2-TNATA/NPB double hole transport layer is morphologically smooth and homogeneous, and free of pinholes that may cause a leakage current. It therefore not only enhances hole injection but also the durability of the devices. The highly efficient host material $Almq_3$ also improves the overall device efficiency and brightness.

3.5 References

[1] C. W. Tang, and S. A. VanSlyke, Appl. Phys. Lett. **51**, 913 (1987).

[2] Y. Tung, T. Ngo, M. Hack, J. Brown, N. Koide, Y. Nagara, Y. Kato, and H. Ito,SID Symposium Digest of Technical Papers **35**, 48 (2004).

[3] U. S. Department of Energy, Illuminating the challenges: Solid state Lighting Program Planning Workshop Report, U. S. Government Printing Office, Washington, D. C., 1 (2003)

[4] B. W. D'Andrade, and S. R. Forrest, Adv. Mater. **16**, 1585 (2004).

[5] J. Kido, M. Kimura, and K. Nagai, Science **267**, 1332 (1995).

[6] G. Li and J. Shinar, Appl. Phys. Lett. **83**, 5359 (2003).

[7] B. W. D'Addrade, R. J. Holmes, and S. Forrest, Adv. Mater. 16, 624 (2004).

[8] S. P. Singh, Y. N. Mohapatra, M. Qureshi, and S. S. Manoharan, Appl. Phys. Lett. **86,** 113505 (2005).

[9] A. Dodabalapur, L. H. Rothberg, and T. M. Miller, Appl. Phys. Lett. **65**, 2308 (1994).

[10] Z. Y. Xie, J. Feng, J. S. Huang, Y. Wang, and J. C. Chen, Synth. Met. **108**, 81 (2000).

[11] Y. Shao, and Y. Yang, Appl. Phys. Lett. **86**, 073510 (2005).

[12] D. A. Vanderwater, I. H. Tan, G. E. H ¨ Ofler, D. C. Defevere, and F. A. Kish, Proceedings of the IEEE **85**, (1997).

[13] Y. Shirota, Y. Kuwabara, D. Okuda, R. Okuda, H. Ogawa, H. Inada, T. Wakimoto, H. Nakada, Y. Yonemoto, S. Kawami, K. Imai, Journal of Luminescence **72-74**, 985 (1997).

[14] D. Gebeyehua, C.J. Brabec, F. Padinger, T. Fromherz, J.C. Hummelen, D. Badt, H. Schindler, N. S. Sariciftci, Synth. Met. **118**, 1 (2001).

[15] J. Kido and Y. Lizumi, Appl. Phys. Lett. **73**, 2721 (1998).

[16] S. J. Strickler and R. A. Berg, J. Chem. Phys. **37**, 814 (1962).

[17] L. Zou, V. Savvate'ev, J. Booher, C. H. Kim, and J. Shinar, Appl. Phys. Lett. **79**, 2282 (2001).

[18] H. Nakanotani, H. Sasabe, and C. Adachi, Appl. Phys. Lett. **86**, 213506 (2005).

[19] H. Spreitzer, H. Schenk, J. Salbeck, F. Weissoertel, H. Riel, and W. Riess, Proceeding of SPIE, **3797** 316 (1999).

4. STRUCTURALLY INTEGRATED ORGANIC LIGHT-EMITTING DEVICE (OLED)-BASED SENSOR FOR INDUSTRIAL AND ENVIRONMENTAL SECURITY: SENSORS FOR HYDRAZINE AND ANTHRAX

An invited paper published in proceeding of SPIE Vol. **5994**-19, p1-9 (2005)

Note: The anthrax sensors were fabricated and studied by Dr. Bhaskar Choudhury, as part of his PhD thesis research. Therefore, only the parts of the paper describing the hydrazine sensors are reproduced in this chapter.

Zhaoqun Zhou, Ruth Shinar, Bhaskar Choudhury, Louisa B. Tabatabai, Chuxiong Liao, and Joseph Shinar

Abstract

The application of the new compact platform of structurally integrated, photoluminescent (bio) chemical sensors, where the photoluminescence (PL) excitation source is an OLED, to the detection of hydrazine and anthrax, is described. The hydrazine sensor is based on the reaction between nonluminescent anthracene-2, 3-dicarboxaldehyde and hydrazine or hydrazine sulfate, which generates a luminescent product. The results clearly show that the limit of detection of hydrazine by this system is ~60 ppb in 1 min, i.e., roughly equivalent to 1 ppb in 1 hr. Hence the sensitivity of this system exceeds the OSHA requirements by a factor of ~80.

4.1 Introduction

The field of photoluminescence (PL)-based chemical or biological sensors is growing rapidly [1-4]. Such sensors are typically composed of a sensing element, whose PL is monitored before and during exposure to the analyte, a light source which excites the PL, and

a photodetector (PD). The structural integration of these components is highly desirable, yet current light sources such as lasers and inorganic LEDs are bulky or require intricate integration procedures [5]. In contrast, the structural integration of an OLED with a sensing element is simple, resulting in small size devices [6-12] which are attractive for developing miniaturized sensor arrays for medical and environmental applications, including for high throughput, multianalyte analysis. This paper describes some recent results towards the realization of this new sensor platform for detection of hydrazine, which is needed for industrial and environmental security.

OLEDs are multilayer structures of organic layers sandwiched between an anode, typically indium tin oxide (ITO), and a metal cathode. They are easily fabricated by e.g., low vacuum thermal deposition of the organic layers on transparent substrates such as ITO-coated glass or plastic. The resulting device thickness is <0.5 μm, thus, the thickness of such an excitation source is determined by the thickness of the substrate. The viability of the proposed structurally integrated OLED/luminescent sensors results from the intrinsic advantages of OLEDs as low-voltage, miniaturizable [13], flexible [14] and efficient light sources, and the dramatic improvements in OLEDs achieved over the past decade, which has led to their emergence in commercial products [15].

These improvements include external quantum efficiencies and lifetimes which exceed 18% and ~60,000 hours, respectively, for green emitters, and 6% and ~4,000 hours, respectively, for blue emitters [14]. Motivated by the need for miniaturized sensors and multianalyte sensor arrays, and the above-mentioned OLED attributes, we have recently explored this new sensor platform by fabricating structurally integrated PL-based oxygen, glucose, hydrazine, and anthrax lethal factor (LF) sensors [8-10]. The basic structure of the

platform is shown in Fig. 1, where the OLED excitation source is deposited on one side of a glass substrate, while the sensing component is deposited on the other side of the substrate. Equivalently, the OLED and sensing components can be fabricated on separate substrates and attached back-to-back.

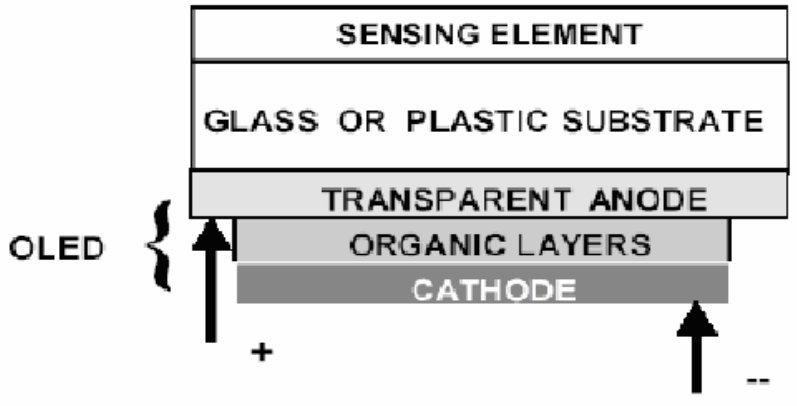

Figure 1. Basic structure of an integrated OLED/photoluminescence –based chemical and biological sensor.

This paper describes our recent results on the hydrazine and anthrax LF sensors. The development of OLED-based compact, field-deployable hydrazine sensors is motivated by the use of hydrazine, a highly toxic and volatile compound, as a powerful monopropellant in NASA space shuttles and a common precursor in the synthesis of some polymers, plasticizers and pesticides. Specifically, it's melting and boiling points are 2.0°C and 113.5°C, respectively; its vapor pressure is 14.4 Torr at 25°C. The American Conference of Governmental Industrial Hygienist) has recommended that the threshold limit value (TLV) for hydrazine exposure (i.e., the time weighted average concentration of permissible exposure within a normal eight-hour workday) be lowered from 100 ppb to 10 ppb in air [16].

The OSHA recommended skin exposure limit is 0.1 ppm (0.1 mg/m^3), and the Immediately Dangerous to Life or Health) concentration is 50.77 ppm [17].

4.2 Experiment setup and results

The hydrazine sensor is based on the reaction between N_2H_4 and anthracene 2,3-dicarboxaldehyde (ADA) (Fig. 2) [10,18]. The reaction product is excited at 476 nm by a blue OLED (see below) and emits at 549 nm; the signal is proportional to the N_2H_4 level (see Fig. 4). The sensor can be operated in air or solution.

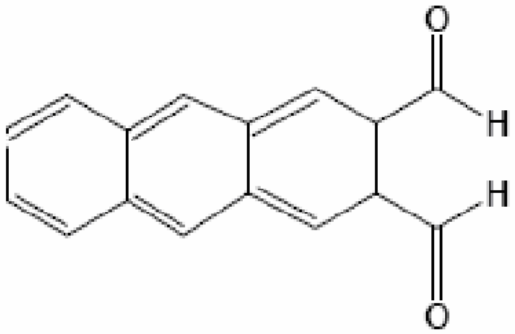

Figure 2. Structure of anthracene 2,3-dicarboxaldehyde (ADA).

The blue OLEDs were fabricated by vacuum evaporation of the organic layers, a CsF buffer layer (which lowers the barrier for electron injection), and the Al cathode, on Applied Films Corp. 20 Ω/square ITO-coated glass, as described previously [7,19-21]. The hole injection layer was copper phthalocyanine (CuPc); the hole-transporting layer was N,N'-diphenyl-N,N'-bis(1-naphthyl phenyl)-1,1'-biphenyl-4,4'-diamine (NPD). It was followed by a blue emitting 4,4'-bis(2,2'-diphenylvinyl)-1,1'-biphenyl (DPVBi) layer [19,22]. The OLEDs were prepared as either an unencapsulated 21×21 matrix array of ~1.5 mm diameter Al disc electrodes evaporated onto the organic layers for front detection (as the needed

mechanical wire contacts did not enable back-detection) [20] or as a smaller encapsulated matrix array of $\sim 2 \times 2$ mm^2 square pixels resulting from perpendicular stripes of etched ITO and evaporated Al for back-detection [9]. A typical encapsulated array, with 4×10 pixels lit simultaneously, is shown in Fig. 3. The OLEDs were operated in a dc mode with a forward bias of 9 – 20 V, or in a pulsed mode with a forward bias of up to 35 V. The photodetector (PD) was a photomultiplier tube (PMT).

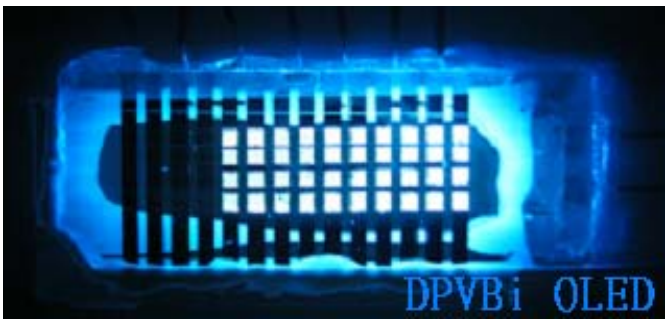

Figure 3. A 4×14 array of blue DPVBi OLEDs used to excite the PL of the reaction product of ADA and hydrazine. In the image at right, 4×10 pixels are lit. Each pixel is ~2×2 mm^2.

To avoid the hazards associated with exposure to N_2H_4, initial measurements exploring the OLED-based platform were performed using hydrazine sulfate ($N_2H_4 \bullet H_2SO_4$), which is less hazardous. Fig. 4 shows the PL intensity of the ADA-analyte solution for varying analyte levels in the 0 - 10 μg/L range. The PL was excited by a blue DPVBi OLED. Previously, using blue Firpic-doped CBP OLEDs or DPVBi OLEDs, the limit of detection (LOD) was ~50 μg/L. By optimizing OLED operation parameters, e.g., OLED voltage and pulse width, the LOD was reduced to < 5 μg/L in the final solution.

The hydrazine sulfate was monitored using a 96 well plate, where 1 mL buffer solution was mixed with 20 μL of 0.8 mM ADA in ethanol. This was followed by the addition of 40 μL of 66, 123, 184, or 230 μg/L hydrazine sulfates in water.

For monitoring hydrazine gas, disposable hydrazine permeation tubes were used. Fig. 5 shows the measurement system assembled to determine the LOD of the sensor for hydrazine in air. The disposable permeation tube was heated to 80°C by a Kin Tek CO395 Certification Oven. At that temperature, the emission rate of the hydrazine is 2750 ng/min. That emission rate corresponds to a concentration of 3.84 ppm in a carrier gas flowing at 500 sccm. Since the emission rate decreases by about 50% for every 10°C decrease of the oven temperature, a hydrazine concentration of ~60 ppb is obtained when the oven is at room temperature.

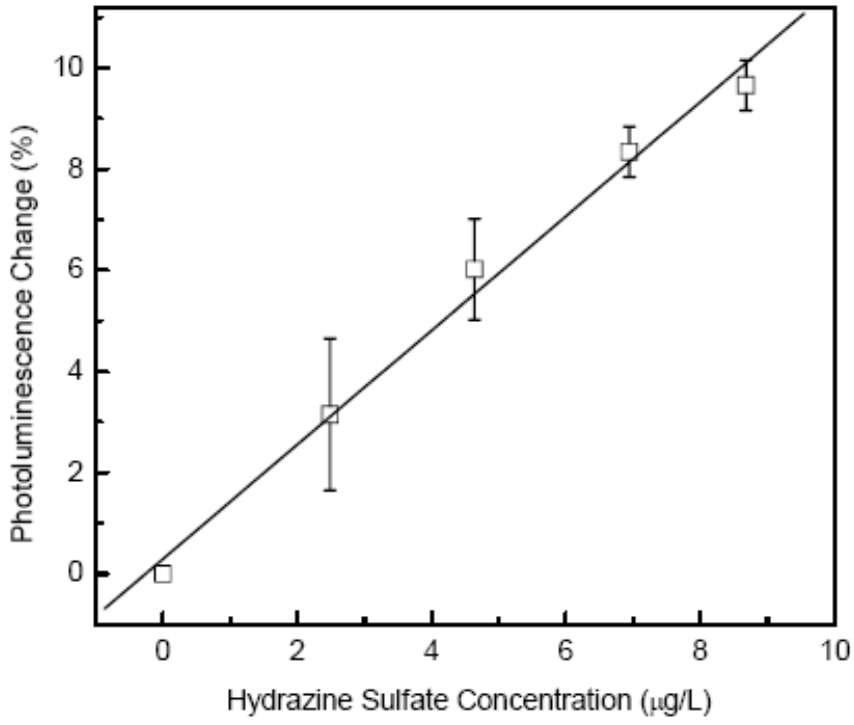

Figure 4. PL intensity vs hydrazine sulfate concentration. The PL was excited by a DPVBi OLED biased with 20us, 15 v pulses, at a repetition rate of 50 Hz.

To optimize the OLED-based hydrazine sensor performance, the OLED pulse width and voltage were varied. The optimal values were found to be 20 μs and 30 V, respectively. Fig. 6 shows the change in the PL of the hydrazine/ADA solution, excited by 10 - 60 μs pulses of a DPVBi OLED biased at 30 V, upon exposure to 60 ppb of hydrazine in Ar, bubbled through the solution at 500 sccm. Fig. 7 shows the PL change induced by 20 μs pulses of the OLED biased at 25 to 35 V under similar experimental conditions. The optimal parameters for the OLED operation are believed to be due to the dependence of the overshoot spikes of DPVBi OLEDs, which enhance the EL intensity at the end of the bias pulse, on the bias and pulse width [19, 23].

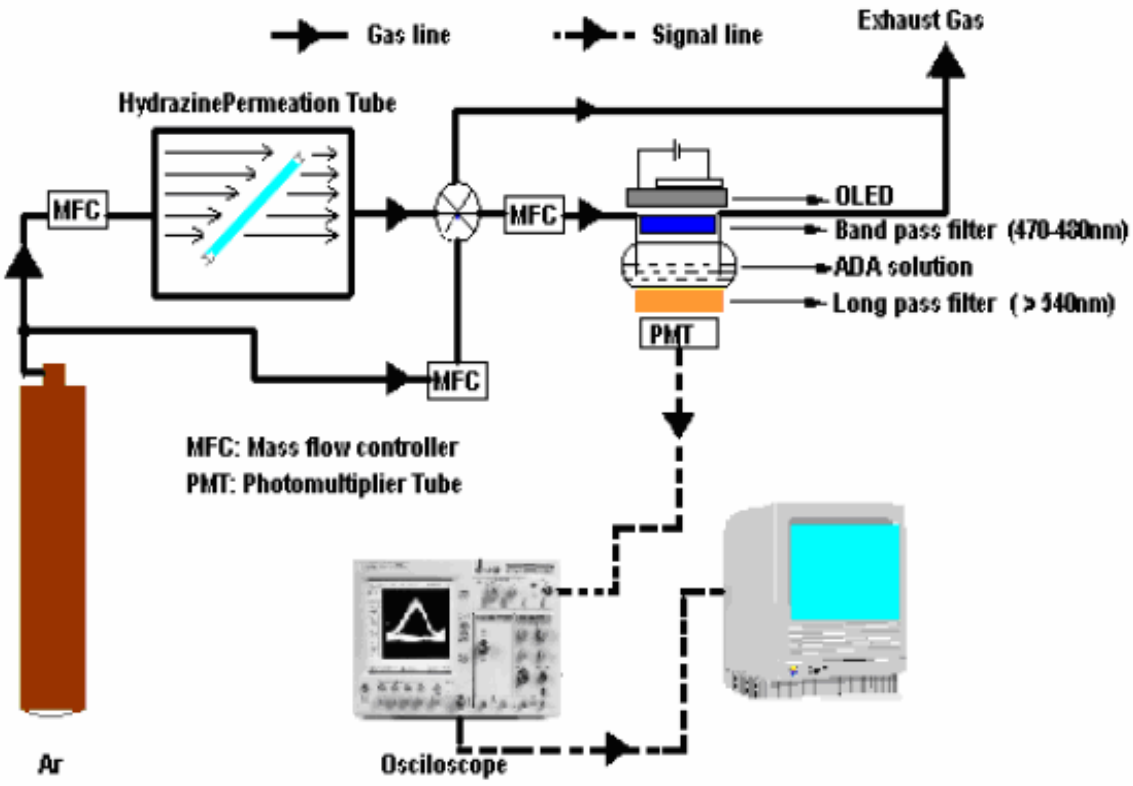

Figure 5. Schematic of the trace hydrazine generation and detection system.

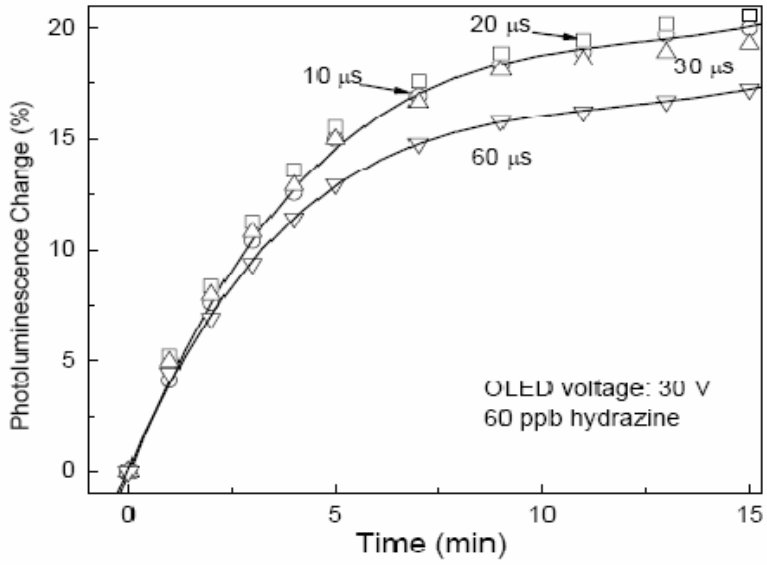

Figure 6. PL change of the hydrazine/ADA solution upon exposure to 60 ppb hydrazine in air, bubbled at 500 sccm, vs time. The PL was excited by 10-60 us pulses of a DPVBi OLED biased at 30V, at a repetition rate of 50 Hz.

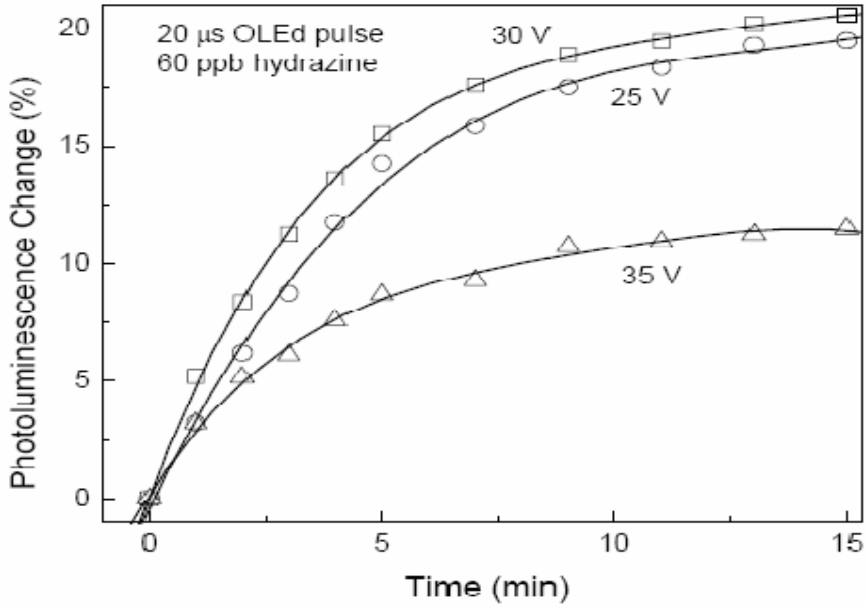

Figure 7. PL change of the hydrazine/ADA solution upon exposure to 60 ppb hydrazine in Ar, bubbled at 500 sccm, vs time. The PL was excited by a 20 μs pulse of a DPVBi OLED biased at 25 to 35 V, at a repetition rate of 50 Hz.

The results clearly show that the LOD of hydrazine by this system is ~60 ppb in 1 min, i.e., roughly equivalent to 1 ppb in 1 hr. Hence the sensitivity of this system exceeds the

OSHA requirements by a factor of ~80. We are currently exploring methods to develop ADA-based solid-state sensors.

4.3 Conclusion

The utility of structurally integrated OLED-based sensors for detection of hydrazine was demonstrated. The limit of detection for hydrazine gas bubbled through the ADA solution far exceeds OSHA requirements. Studies are underway to develop a more robust sensor based on a thin film-sensing component. The use of ultra-thin OLED excitation source in PL–based sensors will enable the realization of small-size, robust, field-deployable sensors for industrial and environmental security. Efforts are also underway to develop compact OLED-based multianalyte arrays.

4.4 Acknowledgements

Ames Laboratory is operated by Iowa State University (ISU) for the United States Department of Energy (USDOE) under Contract W-7405-Eng-82. This work was supported by the Director for Energy Research, Office of Basic Energy Sciences, USDOE, the National Aeronautics and Space Administration, and the National Science Foundation.

4.5 References

[1] O. S. Wolfbeis and H. E. Posch, "Fiberoptic Fluorescing Sensor for Ammonia," Anal. Chim. Acta **185**, 321 (1986); B. H. Weigl, A. Holobar, W. Trettnak, I. Klimant, H. Kraus, P. O'Leary, and O. Wolfbeis, “Optical triple sensor for measuring pH, oxygen and carbon dioxide,” J. Biotech. **32**, 127 (1994); P. Hartmann and W. Ziegler, “Lifetime Imaging of

Luminescent Oxygen Sensors Based on All-Solid-State Technology," Anal. Chem. **68**, 4512 (1996).

[2] A. K. McEvoy, C. M. McDonagh, and B. D. MacCraith, "Dissolved Oxygen Sensor Based on Fluorescence Quenching of Oxygen-Sensitive Ruthenium Complexes Immobilized in Sol-Gel-derived Porous Silica Coatings," Analyst **121**, 785 (1996).

[3] B. D. MacCraith, C. McDonagh, A. K. McEvoy, T. Butler, G. O'Keeffe, and V. Murphy, "Optical Chemical Sensors Based on Sol-Gel Materials: Recent Advances and Critical Issues," J. Sol-Gel Sci. Tech. **8**, 1053 (1997).

[4] X. Li and Z. Rosenzweig, "A fiber optic sensor for rapid analysis of bilirubin in serum," Anal. Chim. Acta **353**, 263 (1997).

[5] E. J. Cho and F. V. Bright, "Optical Sensor Array and Integrated Light Source," Anal. Chem. **73**, 3289 (2001).

[6] W. Aylott, Z. Chen-Esterlit, J. H. Friedl, R. Kopelman, V. Savvateev, and J. Shinar, "Optical Sensors and Multisensor Arrays Containing Thin Film Electroluminescent Devices," US Patent No. 6,331,438 (December 2001).

[7] V. Savvate'ev, Z. Chen-Esterlit, C.-H. Kim, L. Zou, J. H. Friedl, R. Shinar, J. Shinar, and R. Kopelman, "Integrated Organic Light Emitting Device/Fluorescence-Based Chemical Sensors," Appl. Phys. Lett. **81**, 4652 (2002).

[8] B. Choudhury, R. Shinar, and J. Shinar, "Luminescent chemical and biological sensors based on the structural integration of an OLED excitation source with a sensing component," in *Organic Light Emitting Materials and Devices VII,* edited by Z. H. Kafafi and P. A. Lane, SPIE Conf. Proc. **5214**, 64 (2004).

[9] B. Choudhury, R. Shinar, and J. Shinar, "Glucose Biosensors Based on Organic Light Emitting Devices Structurally Integrated with a Luminescent Sensing Element," J. Appl. Phys. **96**, 2949 (2004).

[10] R. Shinar, B. Choudhury, Z. Zhou, H.-S. Wu, L. Tabatabai, and J. Shinar, "Structurally Integrated Organic Light-Emitting Device-Based Sensors for Oxygen, Glucose, Hydrazine, and Anthrax," in *Smart Medical and Biomedical Sensor Technology II,* edited by Brian M. Cullum, SPIE Conf. Proc**. 5588**, 59 (2004)

[11] S. Camou, M. Kitamura, J.-P. Gouy, H. Fujita, Y. Arakawa and T. Fujii, Proc. SPIE **4833**, 1 (2002).

[12] O. Hofmann, X. Wang, J. C. deMello, D. D. C. Bradley, and A. J. deMello, "Towards microalbuminuria determination on a disposable diagnostic microchip with integrated fluorescence detection based on thin-film organic light emitting diodes," Lab on a Chip (2005).

[13] Emagin Corporation, OLED micro display, 2004, <www.emagincorp.com>

[14] Universal display corporation, OLED display, 2004, <www.universaldisplay.com>.

[15] Sony, OLED display, 2004, <www.sony.com>, Toshiba, OLED display, 2004, <www.toshiba.co.jp>, Pioneer, OLED display, 2001, <www.pioneer.co.jp>, Samsung, OLED display, 2004, <www.samsung.co.kr>.

[16] American Conference of Governmental Industrial Hygienists (ACGIH). 1999 TLVs and BEIs. Threshold Limit Values for Chemical Substances and Physical Agents, Biological Exposure Indices (Cincinnati, OH 1999). See also http://www.epa.gov/ttn/atw/hlthef/hydrazin.html#ref12

[17] National Institute for Occupational Safety and Health (NIOSH). Pocket Guide to Chemical Hazards. U.S. Department of Health and Human Services, Public Health Service, Centers for Disease Control and Prevention (Cincinnati, OH. 1997, <http://www.cdc.gov/niosh/npg/npg.html>).

[18] S. Rose-Pehrsson and G. E. Collins, "The Fluorescence Detection of Hydrazine via Derivatization with 2,3-Naphthalene Dicarboxaldehyde," US Patent 5,719,061 (Feb 17, 1998).

[19] V. Savvate'ev, J. H. Friedl, L. Zou, J. Shinar, K. Christensen, W. Oldham, L. J. Rothberg, Z. Chen-Esterlit, and R. Kopelman, "Nanosecond Transients in Electroluminescence from Multilayer 4,4'-bis(2,2'diphenyl vinyl) -1,1'-biphenyl-Based Blue Organic Light-Emitting Devices," Appl. Phys. Lett. **76**, 1501 (2000).

[20] L. Zou, V. Savvate'ev, J. Booher, C.-H. Kim, and J. Shinar, "Combinatorial fabrication and studies of intense efficient ultraviolet-violet organic light emitting device arrays," Appl. Phys. Lett. **79**, 2282 (2001).

[21] K. O. Cheon and J. Shinar, "Combinatorial Fabrication and Study of Doped-Layer-Thickness Dependent Color Evolution in Bright Small Molecular Organic Light-Emitting Devices," Appl. Phys. Lett. **83**, 2073 (2003).

[22] S. E. Shaheen, G. E. Jabbour, M. M. Morell, Y. Kawabe, B. Kippelen, N. Peyghambarian, M.-F. Nabor, R.Schlaf, E. A. Mash, and N. R. Armstrong, "Bright Blue Organic Light Emitting Diode with Improved Color Purity Using a LiF/Al Cathode," J. Appl. Phys. **84**, 2324 (1998).

[23] K. O. Cheon and J. Shinar, "Electroluminescence Spikes, Turn-off Dynamics, and Charge Traps in Organic Light-Emitting Devices," Phys. Rev. B (Rap. Comm.) **69**, 201306 (R) (2004).

5. STRUCTURALLY INTEGRATED ORGANIC LIGHT EMITTING DEVICE-BASED SENSORS FOR GAS PHASE AND DISSOLVED OXYGEN

A paper published in Analytica Chimica Acta, **568** 190–199 (2006)

Ruth Shinar, Zhaoqun Zhou, Bhaskar Choudhury, Joseph Shinar

Abstract

A compact photoluminescence (PL)-based O_2 sensor utilizing an organic light-emitting device (OLED) as the light source is described. The sensor device is structurally integrated. That is, the sensing element and the light source, both typically thin films that are fabricated on separate glass substrates, are attached back-to-back. The sensing elements are based on the oxygen-sensitive dyes Pt- or Pd-octaethylporphyrin (PtOEP or PdOEP, respectively), which are embedded in a polystyrene (PS) matrix, or dissolved in solution. A green OLED light source, based on tris(8-hydroxy quinoline) Al (Alq3), was used to excite the porphyrin dyes. The O_2 level was monitored in the gas phase and in water, ethanol, and toluene solutions by measuring changes in the PL lifetime τ of the O_2-sensitive dyes. The sensor performance was evaluated in terms of the detection sensitivity, dynamic range, gas flow rate, and temperature effect, including the temperature dependence of τ in pure Ar and O_2 atmospheres. The dependence of the sensitivity on the preparation procedure of the sensing film and on the PS and dye concentrations in the sensing element, whether a solid matrix or solution, were also evaluated. Typical values of the detection sensitivity in the gas phase, $S_g \equiv \tau(0\%O_2)/\tau(100\%O_2)$, at 23°C, were ~35 to ~50 for the [Alq_3 OLED]/[PtOEP dye] pair; S_g exceeded 200 for the Alq_3/PdOEP sensor. For dissolved oxygen (DO) in water and

ethanol, S_{DO} (defined as the ratio of τ in de-oxygenated and oxygen-saturated solutions) was ~9.5 and ~11, respectively, using the PtOEP-based film sensor. The oxygen level in toluene was measured with PtOEP dissolved directly in the solution. That sensor exhibited a high sensitivity, but a limited dynamic range. Effects of aggregation of dye molecules, sensing film porosity, and the use of the OLED-based sensor arrays for O_2 and multianalyte detection are also discussed.

5.1 Introduction

5.1.1 Photoluminescence-based oxygen sensors

There is a growing need for low-cost compact chemical and biological sensor platforms for commercial, including biomedical, applications. This need has resulted in efforts to develop structurally integrated oxygen sensors as well as platforms suitable for multianalyte detection that are efficient and easily fabricated. A well-known approach for gas-phase and solution O_2 sensing is based on the dynamic quenching of the photoluminescence (PL) of oxygen-sensitive dyes such as Ru-complexes and Pt or Pd porphyrins [1–16]. Collisions with increasing levels of O_2 result in a decrease in the PL intensity I and PL decay time τ. In a homogeneous matrix, the O_2 concentration can be determined ideally by monitoring changes in I under steady-state conditions or in τ using the Stern–Volmer (SV) equation:

$$\frac{I_0}{I} = \frac{\tau_0}{\tau} = 1 + K_{SV}[O_2] \quad (1)$$

where I_0 and τ_0 are the values in the absence of oxygen and K_{SV} is the S-V constant.

Despite the established sensing approach, in particular for gas phase measurements, extensive studies of optical O_2 sensors are still continuing in an effort to enhance sensor performance, reduce sensor cost and size, simplify fabrication, and develop an O_2 sensor that is compatible with in vivo biomedical monitoring [17].

Fast and reliable measurement of dissolved oxygen (DO) in water is important for biological, medical, environmental, and industrial monitoring [18, 19]. Most commercial DO sensors are based on electrochemical techniques that suffer from shortcomings related to oxygen consumption, solution stirring, and electrode poisoning. PL-based DO sensors, which do not suffer from such shortcomings, have also been studied [16, 20–22]. For example, a Ru-complex was used in a porous sol–gel silica film [11] and quenching responses of 56 and 80%, which depend on the sol–gel nature, were obtained. These quenching responses correspond to detection sensitivities S_{DO}, defined for DO sensing as the ratio of the PL intensity or lifetime in a de-oxygenated solution to the corresponding value in an oxygen-saturated solution, from ~2.3 to 5. A submicrometer optical fiber DO sensor, also based on a Ru dye, showed a sensitivity of 3.2 when the dye was embedded in an acrylamide polymer [9]. Pt octaethylporphyrin (PtOEP) in polymer matrices have been studied mostly for O2 monitoring in the gas phase with fewer studies for DO.

An SV plot for a PtOEP dye embedded in a fluorinated polymer was recently obtained for DO in water [16]. The plot was close to linear at O_2 concentrations <10 mg/L (i.e., 10 ppm by mass); it deviated from linearity (downward curvature) at higher concentrations. The sensitivity at 20°C was ~1.8. Large sensitivity (overall quenching response of 97%, i.e., S_{DO} ~33) and linear response over the entire concentration range were

reported recently for a PtOEP-based nanosensor [15]. The enhanced sensor performance was attributed to high porosity, hydrophobicity, and a larger surface-to-volume ratio of the sensing element.

Detection of DO in aqueous and organic media was also reported using an oxygen-sensitive dye in a sol–gel matrix and a Ru-based dye immobilized in a Nafion membrane [12]. In the latter, membrane swelling was a key factor in the quenching process. Solvents that penetrated the membrane (e.g., methanol and water) resulted in linear SV plots with large responses, whereas solvents such as toluene, which do not penetrate the Nafion, resulted in poor sensitivity and nonlinear SV plots.

Development of field-deployable, compact sensors is expected to be beneficial for the varied needs of gas phase and DO monitoring. We therefore tested the use of an organic light emitting device (OLED)-based sensor for such applications. OLED-based sensors with tris(4,7-diphenyl-1,10- phenanthroline) Ru II (Ru(dpp)) embedded in a sol–gel film and PtOEP and PdOEP embedded in polystyrene (PS) were used for gas phase O_2 detection. A PtOEP-doped PS film was used for O_2 detection in water and ethanol; PtOEP dissolved in a toluene solution was used for monitoring oxygen in toluene. Though the PS matrix may not be the ideal host for sensing of DO [23], our results, discussed below, demonstrate the viability of the OLED based sensor platform for high sensitivity O2 monitoring.

5.1.2 Structurally integrated photoluminescence-based sensor

The potential viability of structurally integrated OLED-based luminescent chemical and biological sensors results from the intrinsic advantages of OLEDs as low-voltage, miniaturizable [24], flexible [25, 26], and efficient light sources, and the dramatic

improvements in OLEDs achieved over the past decade, which has led to their emergence in commercial products [27].

These improvements include external quantum efficiencies and lifetimes which exceed 18% and 20,000 h, respectively, for phosphorescent green emitters [28–30], and 6% and 3000 h, respectively, for blue emitters [31, 32]. OLEDs are easily fabricated on glass or plastic substrates, in sizes ranging from ~100 μm^2 to > 100 mm^2. They consist of an anode, organic layers, and a cathode. The thickness of the OLED is typically < 0.5 μm. The OLEDs are operated by applying a low pulsed or dc positive bias of 9–20V. The basic structure of the OLED-based sensor platform is as shown in chapter 4, where the OLED excitation source is deposited on one side of a glass substrate, while the sensing component is fabricated on the other side of the substrate. Equivalently, the OLED and sensing components can be fabricated on separate substrates and attached back-to-back. For generating a compact sensor device, the position of the photodetector (PD) is important as well. One possible PD position is "in front" of the volume containing the analyte ("front-detection"). If the OLED consists of a single opaque pixel, this front-detection geometry is the obvious geometry. If, however, the OLED is transparent, or consists of an array of pixels, the PD can monitor the PL that passes through the transparent OLED or the gaps between the OLED pixels. In this geometry, therefore, the PD is positioned "behind" the transparent OLED or OLED array ("back-detection;" see Fig. 1 in chapter 4). Both front- and back-detection geometries are suitable for integration and miniaturization purposes, as well as for development of PL based sensor (micro) arrays for multianalyte detection. However, when using a PD such as a Si photodiode or a photomultiplier tube (PMT), the back-detection geometry is a simpler approach for

fabricating compact sensors, since in that geometry the analyte sample is in front of the entire sensor device, resulting in easier sample handling.

The rise and fall time of the electroluminescence (EL) of appropriate OLEDs operating in a pulsed mode, typically < 100 ns, is much faster than τ of the O_2-sensitive dyes used for monitoring gaseous or dissolved oxygen, which is typically 0.5–1000 μs. Hence the OLEDs can be used to monitor oxygen through its effect on I or τ. For monitoring I, the OLEDs are excited in a dc mode, while for monitoring τ they are operated in a pulsed mode. The advantage of using OLED excitation, in particular in pulsed operation, in comparison to laser excitation, was demonstrated previously [4,5]. For example, over 6 h, I of a typical Ru(dpp)-doped sol–gel film and a PtOEP-doped PS film decreased by 80 and 50%, respectively, under 3mW laser excitation at 488 and 515 nm, respectively, I of these dyes decreased only by <5% under pulsed blue and green OLED excitation at 400 Cd/m^2 and 10% duty cycle of a 100 μs pulse. This situation, together with the OLED attributes described above, demonstrates the potential viability of OLEDs as excitation sources for compact, commercial sensor devices, as the stability of the OLEDs is greater than that of either dye under laser excitation.

Thus, the utility of pulsed OLED excitation is advantageous for improving long-term sensor stability and, in addition, for protecting heat-sensitive sensing elements and/or analytes due to reduced heat generation by OLED excitation [2].

In this work we describe the development of structurally integrated oxygen sensors in which the light sources are OLEDs suitable for excitation of oxygen-sensitive dyes. The advantage of the OLED-excited sensors is presented through their small and flexible size, ease of fabrication, potential low cost, and promise as efficient light sources in sensor (micro)

arrays for multianalyte detection, including in real-world applications. The performance of the sensors in the gas phase and in solution is evaluated in terms of the dynamic range and the detection sensitivity at different temperatures, the effect of the temperature on τ_0 and τ (100% O_2), and the effect of the preparation procedure of the sensing elements on these metrics. In the gas phase, $S_g \equiv \tau_0/\tau(100\%\ O_2)$; in solution, as mentioned, S_{DO} is the ratio of τ measured in a de-oxygenated solution to that of an oxygen saturated solution. The utility of the OLED-based platform for detection of O_2 at various levels using different sensor films in a single, small-size array is also discussed.

5.2 Experiment procedures

5.2.1 OLED materials, fabrication and instrumentation

20 Ω/square indium tin oxide (ITO)-coated glass was obtained from Applied Films Corp., *N*,*N*'-diphenyl-*N*,*N*'-bis(1-naphthyl)-1,1'-biphenyl-4,4'-diamine (NPD), and Alq_3 were obtained from H.W. Sands. Copper phthalocyanine (CuPc), and CsF were obtained from Sigma–Aldrich. PtOEP and PdOEP were obtained from H.W. Sands, Ru(dpp) from GFS Chemicals, polystyrene, molecular weight 45,000. All chemicals were used as received. Their structures are shown in Fig. 1.

OLED arrays were fabricated by thermal vacuum evaporation of the organic layers in an evaporation chamber (background pressure ~ 5×10^{-7} Torr) installed in an Ar-filled glove box (typical water and O_2 levels ~1 ppm). The sensor PL was monitored with a Hamamatsu R6060 photomultiptier (PMT) tube operated at 900V. The PMT was typically used in the "back-detection" geometry, collecting the PL passing through the gap between two OLED pixels that were typically used for excitation.

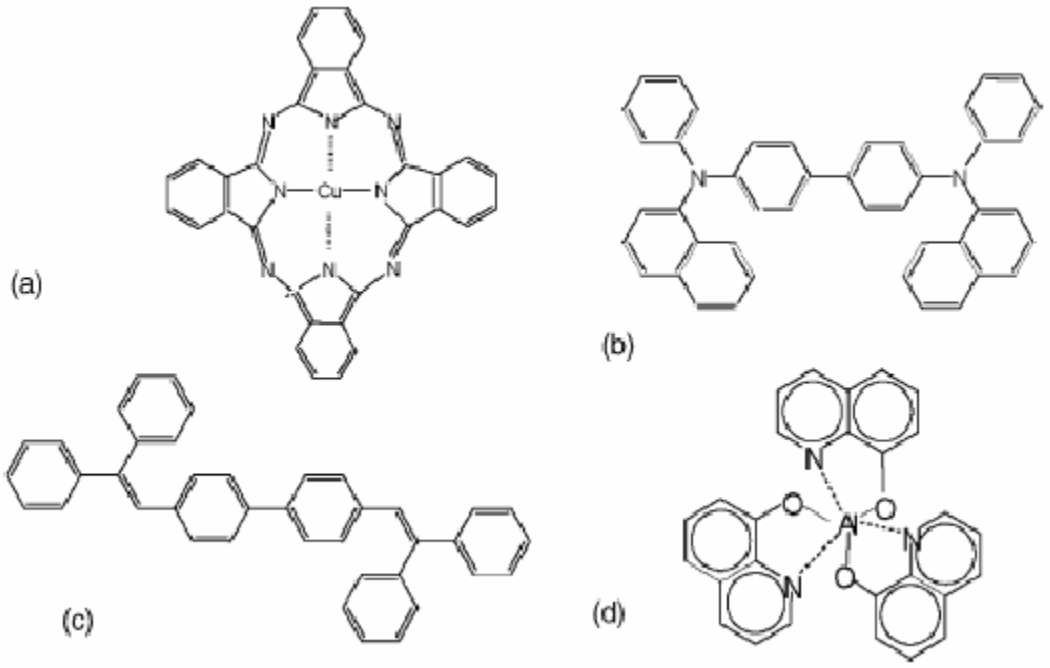

Figure 1. Molecular structures of (a) CuPc, (b) NPD, (c) DPVBi, and (d) Alq3.

Measurements were performed in a flow cell with flowing oxygen/argon mixtures. Mixing was achieved by means of mass flow controllers, where the flow rates of the oxygen and argon varied, while maintaining a constant total flow rate, thus generating varying oxygen partial pressures. Measurements at temperatures above ambient were performed using a Fisher Scientific Isotemp incubator. The incubator housed the sensing element and flow cell, the gas carrying tubing, which was extended to assure its temperature equilibration, the OLED excitation source, and the PMT, which was thermoelectrically cooled and suitable for operation up to 60 ˚C.

For measurements in the "front-detection" geometry, the OLEDs were initially prepared as unencapsulated 21×21 matrix arrays of ~1.5 mm diameter Al disc electrodes evaporated onto the organic layers [36]. For measurements in the "back-detection" geometry, the OLEDs were prepared as an encapsulated matrix array of ~2mm×2mm square pixels

resulting from mutually perpendicular stripes of etched ITO and evaporated Al [3, 5]. Encapsulation was achieved by lining the edges of the glass substrate with epoxy, and binding a top glass cover to the substrate. Initially, a common 5 min epoxy was used.

5.2.2 Sensor elements fabrication

PtOEP- or PdOEP-based sensing elements were prepared by dissolving 0.005–2.5 mg/mL of the dye and 1–100 mg/mL PS in toluene. Films were fabricated by drop casting 5–100 μL of the solution and evenly spreading it onto cleaned glass slides. The resulting films were allowed to dry for several hours in air in the dark at ambient temperature. Freestanding PtOEP/PS films, which were removed from the glass substrate and glued to the opposite side of an OLED glass substrate, were also tested, but they did not show an improved performance.

Solution-based sensing elements (i.e., a dye dissolved in an appropriate solvent) were contained in wells generated in glass. For PtOEP-based sensors, we observed detection sensitivities of ~37 and ~50 (see below), for similarly prepared sensor films fabricated from two different batches of the commercial dye.

5.2.3 Gas phase measurements

Gas phase measurements on the oxygen sensor films excited by integrated Alq3 OLEDs were performed in a flow cell with flowing oxygen/argon mixtures. Mixing was achieved by means of mass flow controllers, as described above. The effect of the flow rate in the range 25–500 sccm was evaluated; there was no effect to the flow rate in this range for any of the oxygen levels studied. For example, for 10% O2, τ was constant at 37.2 μs across

the whole range for one film. Measurements at temperatures above ambient were performed using a Fisher Scientific Isotemp incubator as described above.

5.2.4 Dissolved oxygen measurements

Measuring DO in water in an open cell, which bubbling the gas through the solution, was dependent on the flow rate of the bubbled gas mixture. τ_0, measured after flowing pure Ar for~7 min, generally increased with increasing flow rate (e.g., from ~35 to ~77 μs when the flow rate increased from 25 to 500 sccm). This behavior may indicate the presence of Ar (micro) bubbles at the surface and internal surfaces of the sensor film, in particular at high flow rates, which would result in a longer τ that is not due to DO. This situation can also stem from the need for a high flow rate to remove the DO and minimize dissolution from air. To overcome flow rate and cell-configuration related issues, experiments were performed in a closed cell with a narrow gas inlet and outlet using two approaches. To ensure an equilibrium concentration, the gas mixture was bubbled at 50 or 100 sccm for 15–30 min prior to the measurement; well beyond the 7 min of gas bubbling that appeared to be sufficient to obtain a constant τ. In one approach, gas bubbling was continued during the measurement and care was taken to introduce the gas mixture sufficiently above the sensing films to minimize possible (micro) bubble formation at the films' surface. Using this approach, the results were independent of the gas flow rate, which varied from 15 to 500 sccm; τ_0, obtained by flowing 100% Ar, was ~77 μs; τ (100% O2) was ~2.5 μs. The latter value, however, is suspected to be due to O_2 (micro) bubbles at the sensing element.

In the second approach, the cell was sealed following the bubbling of the gas mixtures used to obtain the desired oxygen levels in the cell gas and solution phases. The gas

phase in the sealed cell was then allowed to equilibrate with the solution. This approach appears to be the most promising in determining DO, as the value of τ measured when the solution was in equilibrium with ambient air was similar to the value measured for the solution exposed to 21% O_2 in Ar. These values were also verified using a commercial Omega model DOH247 DO sensor; 21% bubbled O_2 corresponded to ~8 ppm. Thus, the results shown for DO were obtained using this approach.

We note that for oxygen in toluene, the latter two approaches resulted in comparable results.

5. 3. Results and discussion

In testing the OLED-based sensor platform, we monitored τ, and evaluated SV plots for various films under different experimental conditions. Effects of film preparation procedure, gas flow rate, and measurement temperature for both, gas phase and DO, were monitored. We note that in the gas phase, the response time of the sensor was 1–2 s; this time resulted in a constant response.

5.3.1 Gas phase sensing

5.3.1.1 Effects of film preparation conditions on PtOEP- and PdOEP-doped PS sensors

In optimizing S_g and the dynamic range of the sensing elements using the OLED-based sensor platform, we varied the solution concentrations of the dye and the PS, and their ratio. The best results in terms of *S*g and the dynamic range for the porphyrin-based sensing elements were obtained for films prepared by drop casting 40–50 μL of solutions containing 0.5–1.5 mg/mL dye and 20–50 mg/mL PS in toluene, at a dye:PS ratio of 1:25–1:50.

The effect of the PS concentration in the solution used to generate the sensing film for a PtOEP concentration of 1 mg/mL is shown in Fig. 2. As clearly seen, for 1 mg/mL PtOEP, PS levels of ~30 mg/mL or higher resulted in the highest τ_0. The use of dye concentrations exceeding 2 mg/mL, in particular with PS levels lower than ~10 mg/mL, resulted in shorter τ_0 and reduced sensitivity. This situation is believed to stem from aggregation of dye molecules in the film and consequently, self-quenching. A similar dependence of τ_0 on the dye:PS ratio was observed for PdOEP. For films prepared by drop casting 50 µL of a solution containing 1 mg/mL PdOEP, τ_0 varied from ~52 µs for 1 mg/mL PS to 960 µs for 50 and 100 mg/mL PS.

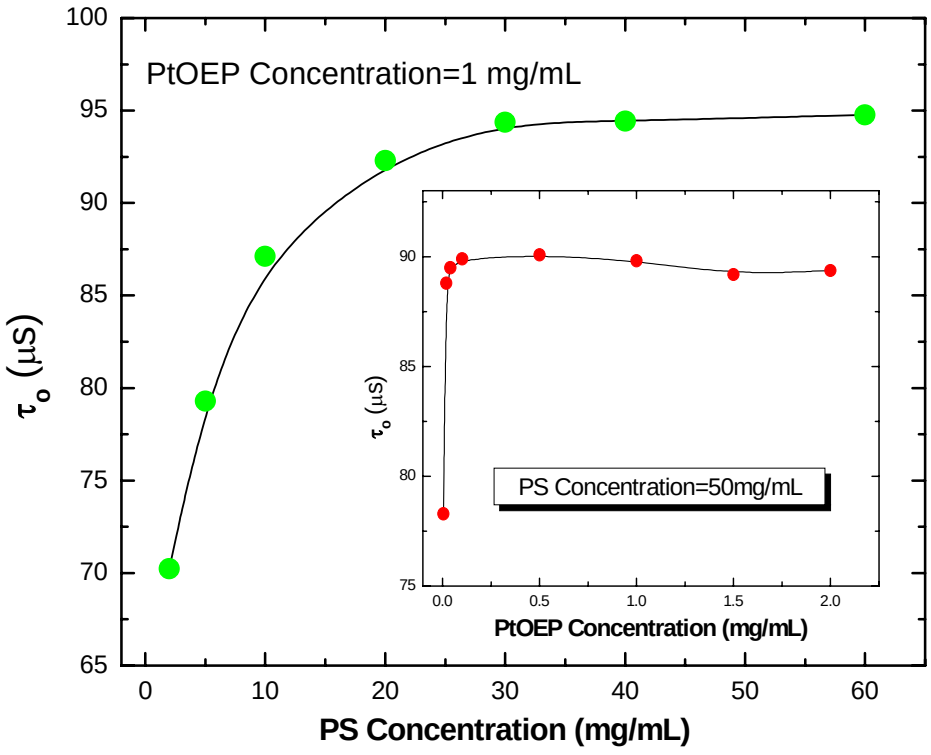

Figure 2. τ_0 in the gas phase as a function of PS concentration in solutions used to generate the sensing films. The PtOEP concentration was 1mg/mL. Inset is τ_0 in the gas phase as a function of PtOEP concentration in solutions, in which PS concentration is at 50 mg/mL. The line is a guide to the eye.

For a film prepared from 50 μL of a 1 mg/mL PdOEP solution in toluene that was allowed to dry on a glass slide, τ_0 was ~38 μs; this short value is believed to be due to self-quenching of the dye molecules clustered in aggregates.

Fig. 3 shows SV plots at 23 ˚C of two different films, using PtOEP from two different commercial batches, similarly prepared by drop casting 50 μL of solutions containing PtOEP:PS at a ratio of 1:50, and evenly spreading the drop. As seen, the use of different commercial batches of PtOEP resulted in different sensor responses, with one batch resulting in *S*g values of ~50, while the other showed lower values, typically of ~37. Variations in the thickness and homogeneity of drop cast films are also suspected to contribute to variations in *S*g in similarly prepared films. As seen, the SV plots for such films are typically nonlinear.

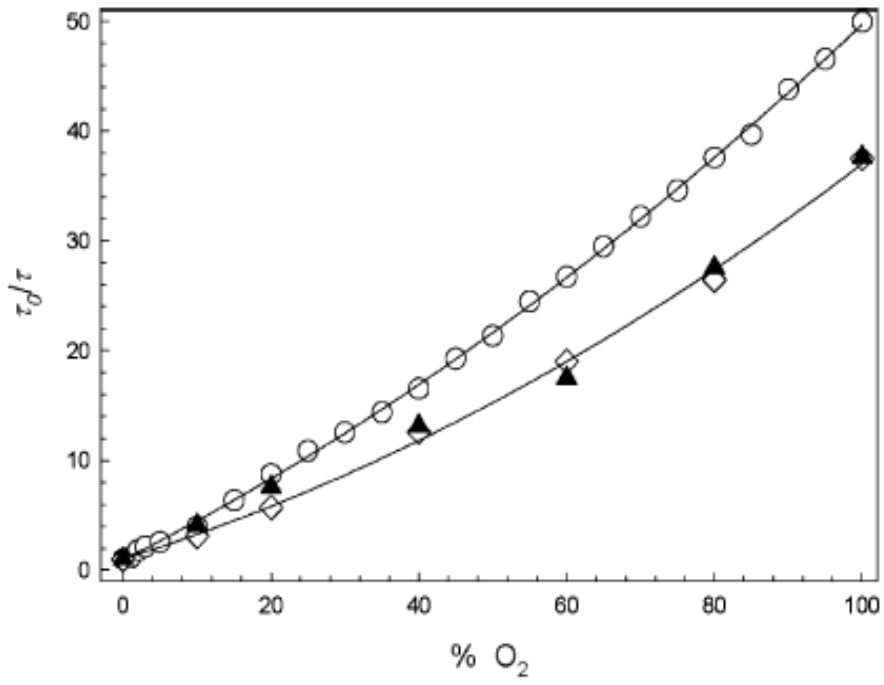

Figure 3. Stern–Volmer plots obtained at 23 °C (○, ◊) for two different films prepared by drop casting 50 μL of solutions containing PtOEP:PS at a ratio of 1:50. The PtOEP originated from two different commercial batches. The SV plot for one film at 45 °C (▲) is also shown. The lines represent a best quadratic fit.

While films with dye:PS ratio of 1:50 are better in terms of *S*g, a 1:10 ratio was still usable, exhibiting a slightly lower sensitivity, but a linear SV plot. Film drying conditions (i.e., in air at~23 or 60 ˚C, under vacuum conditions, or in an Ar atmosphere) did not affect sensor performance appreciably, and AFM and SEM images did not reveal any significant differences between the various films.

The emission band of Alq_3, which peaks at 530 nm, overlaps a small absorption band of the porphyrin dyes. The strong red shift of the PL of the dyes, which peaks at ~645 nm, is advantageous in resulting in a very low background. Moreover, τ_0 (PtOEP) ~100 μs and τ_0 (PdOEP) ~1 ms. Clearly, these long PL lifetimes are responsible for the higher detection sensitivities. The Alq3/PtOEP sensors exhibited sensitivities of typically ~37 or ~50. These sensitivities are from ~10 to ~20 times larger than those of the DPVBi/Ru(dpp) sensors [4,5]. The PdOEP-doped PS sensing film showed larger responses, with *S*g exceeding 200, but a more limited dynamic range, as seen in Fig. 4.

The nonlinear behavior of $1/\tau$ versus $[O_2]$ for Alq3/PtOEP, where the slope increases with increasing $[O_2]$, is unusual, and currently not clear. It may be speculated that oxygen induces local changes in the PS morphology, which enhance accessibility to the PtOEP molecules. For [Alq3 OLED]/PdOEP:PS, linearity is seen only up to ~ 40% O_2; this is probably due largely to O_2 saturation stemming from the high sensitivity of PdOEP to quenching by O_2 and to the moderate porosity of PS. The deviation of the SV plots from linearity, which is often observed [6,11,12,16], is a potential disadvantage in using the porphyrin dyes. In some cases this deviation does not complicate calibration, as it is possible to fit the experimental data to a polynomial (see Fig. 3). Additionally, it is sometimes

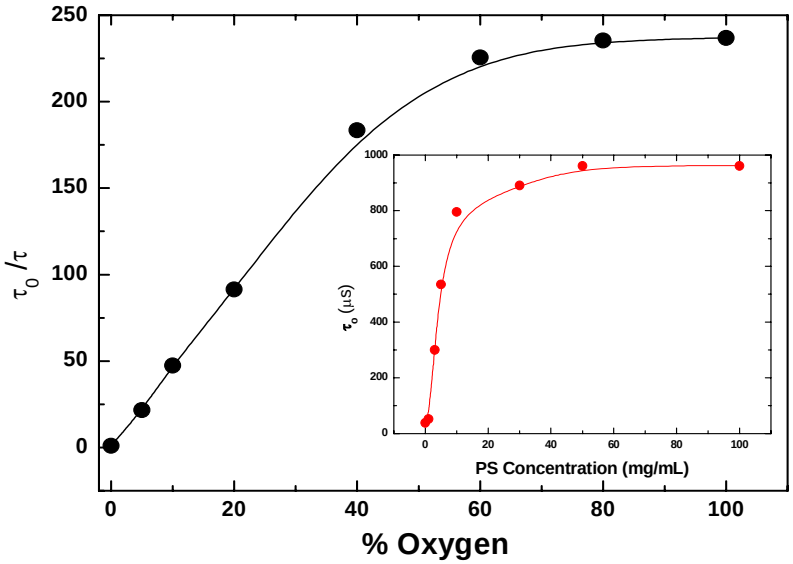

Figure 4. The SV plot at 23 ^{0}C of a PdOEP-based gas phase sensor excited by an Alq_3 OLED. The sensing film was prepared by drop casting and drying in air at room temperature.

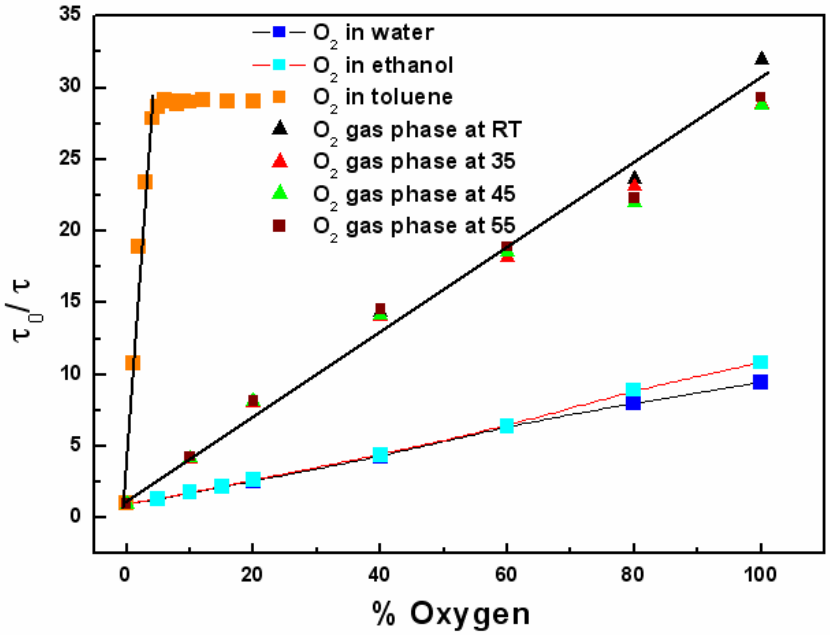

Figure 5. Linear Stern-Volmer plots obtained for gas phase O_2 at 23 ^{0}C (■) and 55 ^{0}C (▲) for a PtOEP:PS film prepared by drop casting 50 μ L of a solution containing 1 mg/mL PtOEP and 10 mg/mL PS, and SV plots for DO in water (○), ethanol (□), and toluene (Δ). For water and ethanol, the sensing element was a thin film of PtOEP embedded in polystyrene; for toluene it was solution-based with 0.01 mg/mL PtOEP in toluene.

possible to obtain linear SV plots by modifying the sensing film, as demonstrated in Fig. 5, which shows the SV plots of a film prepared from a solution of 1:10 ratio of dye:PS. As mentioned, such films showed close to linear SV plots with somewhat reduced sensitivities.

To monitor O_2 levels accurately over the entire 0–100% O_2 range, an array of sensors with various PtOEP and PdOEP films can be used simultaneously. By preparing the films under different conditions (e.g., PS: dye ratio, film thickness), different SV plots and detection sensitivities are expected. For example, one such simple array could comprise two sensing films: a 1:10 PtOEP: PS film that exhibits near linear SV plot over the whole 0–100% range (Fig. 5), and a PdOEP: PS film, which is very sensitive to low levels of O_2 and exhibits a linear behavior up to ~40% O_2 (Fig. 4). By using the OLED-based sensing platform, it is possible to easily fabricate a small-size array of OLED pixels, where two to four pixels correspond to a given sensing film in the sensor array. Thus, through consecutive excitation of such small groups of OLED pixels, O_2 can be detected by different sensing films that exhibit linear calibration plots and sensitivities suitable for different regions of O_2 levels. This approach will also result in redundancy in determining the O_2 level, thus providing a more accurate and reliable result. Moreover, it will provide the basis for sensor (micro) arrays for multianalyte detection, using an array of OLEDs emitting at various wavelength. Such arrays were recently fabricated using combinatorial methods [41].

5.3.1.2 Effect of temperature and gas flow rate

The values of τ are expected to generally decrease with increasing temperature, as the PL quenching is enhanced at elevated temperatures [7,42]. However, in the 23–60 °C range studied in this work, the phosphorescence of porphyrins is only slightly dependent on the

temperature [42]. Indeed, the temperature effect on the SV plots (see Figs. 3 and 5) was minimal; small reductions in τ_0 and τ (100% O_2) were observed as the temperature increased from 23 to 60 °C. The small reproducible decreases in τ_0 were, e.g., from~115 to 109 μs and from~91 to 84 μs (see Fig. 6); τ (100% O_2) showed a similar trend (see inset of Fig. 6). Thus, *S*g for this film varied from ~36.5 to ~37.5 in this temperature range. We note that the reason for the stronger decease in τ_0 observed at ~50 °C is not clear. The gas flow rate in the range of 25–500 sccm had no effect on the gas phase measurements.

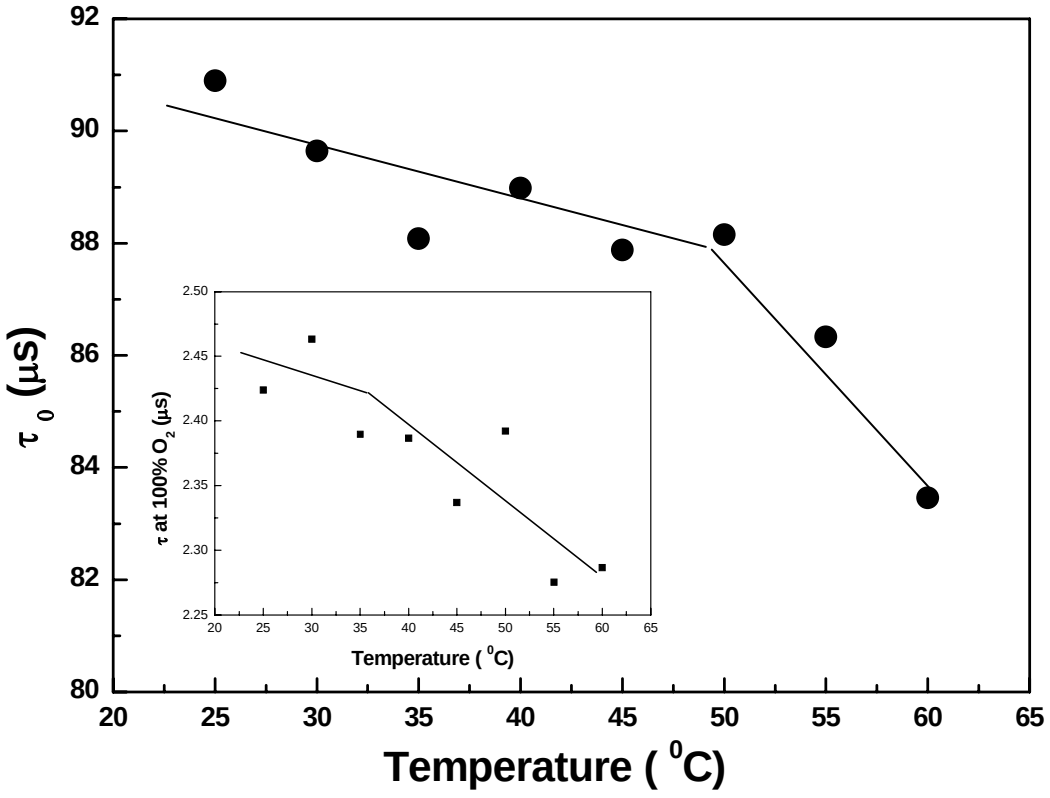

Figure 6. Temperature effect on τ_0 and τ at 100% O_2 (inset) for an Alq_3/PtOEP gas phase sensor. The lines are a guide to the eye.

5.3.2 Dissolved oxygen sensing

5.3.2.1 Detection sensitivity

PtOEP-doped PS films, similar to those used to monitor gas phase oxygen, were used to monitor DO in water and ethanol. The DO in toluene was monitored by measuring τ of PtOEP dissolved in toluene.

Fig. 5 shows also the SV plots of DO in water, ethanol, and toluene. The sensitivities are ~9.5 and 10.8 for water and ethanol, respectively. In water, the values of τ increased from ~8.9 μs in O_2-saturated solution to ~84 μs in Ar-saturated solution; in ethanol, they increased from ~7.9 to ~86 μs. For DO in toluene, the values of τ increased from ~2.2 μs for 5% gas phase oxygen in Ar to ~60 μs in an Ar-saturated solution. The lower values of τ_0 for DO relative to the value in gas phase probably reflect solvent-related PL quenching, as the PL of the polymer-embedded dye was reported to be quenched also by hydroxyl vibrations of water [16]. τ_0 is lowest for toluene, possibly reflecting also incomplete de-oxygenation of the solution together with a sensitivity to ppb levels of oxygen. The high sensitivity in toluene is seen from the lowest value of τ in the O_2-saturated solvent. The larger values of τ in the O_2- saturated water and ethanol in comparison to that in toluene and in the gas phase may indicate the more limited solubility of oxygen in the former. The difference in the sensor responses between toluene and the other solutions is probably largely a result of the enhanced accessibility of the dye molecules in solution relative to their accessibility in the moderately porous solid films.

The similarity of the responses and detection sensitivities for water and ethanol, despite the larger solubility of oxygen in ethanol (~8 times higher at 25 °C) [43], may indicate

that the oxygen concentration in the PS host, which is in equilibrium with the DO, is comparable for both liquids. We note that the detection sensitivities of DO in water measured with the OLED based sensors is among the highest reported to date.

As mentioned above, unlike the case for DO in water and ethanol, where film-based sensing elements were used, the DO in toluene was monitored using a solution-based sensing element, which was responsible for the larger S_{DO}. However, aggregation of the PtOEP molecules in solution can limit S_{DO}. The self-quenching due to such aggregation is demonstrated in Fig. 7, where τ_0 as a function of PtOEP concentration in the toluene solution is shown. As seen, reducing the PtOEP concentration in solution resulted in increased τ_0. This increase is believed to stem from reduced self-quenching and consequently increased S_{DO}.

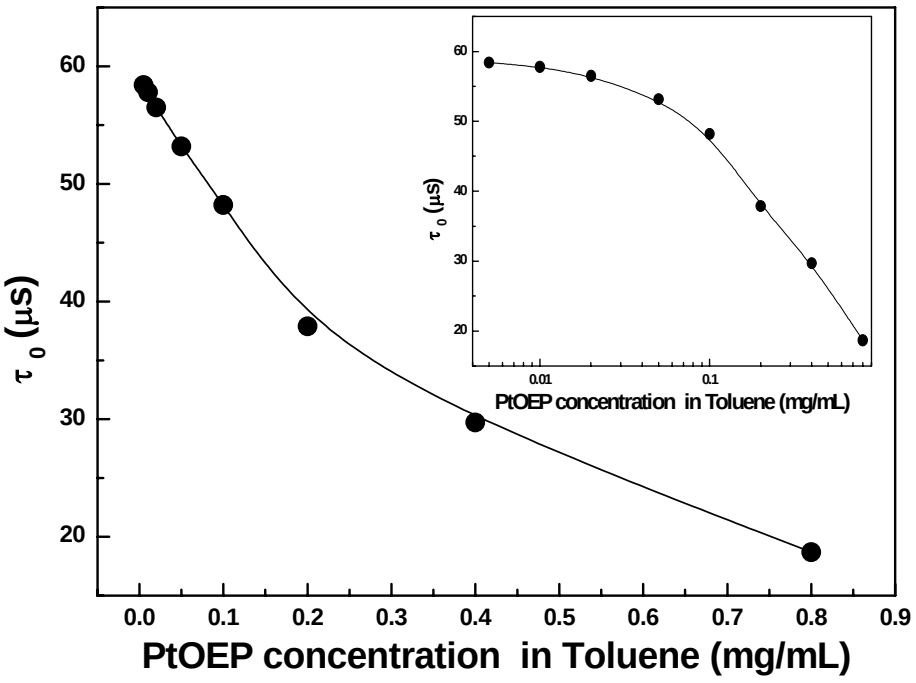

Figure 7. τ_0 of PtOEP for DO in toluene as a function of PtOEP concentration in solution. The inset shows the data on a semi-log scale.

An increased τ_0 is generally expected when the concentration of aggregated dye molecules is reduced. However, the dye concentration should not be reduced below the threshold for aggregate formation, since reduction below this threshold will result in reduced PL intensity and a reduced signal-to-noise ratio. Fig. 7 suggests that for PtOEP in toluene, the optimal concentration is ~0.01–0.02 mg/mL.

5.3.2.2 Effect of temperature

Fig. 8 shows the effect of temperature on τ_0 and τ for an oxygen-saturated water solution. As seen, τ_0 generally decreases with increasing temperature, but the decrease is small, from 84 μs at 23°C to 82 μs at 60°C, i.e., a decrease of 2.4% over ΔT=37°. In contrast, τ for oxygen-saturated water decreases sharply, from ~8.5 μs at 23°C to ~5.3 μs at 60°C, i.e., a decrease of 38%. Consequently, the resulting S_{DO} increases with increasing temperature, unlike the case for the gas phase, where Sg values were largely temperature-independent. The dependence of τ_0 on the temperature was also reported in measuring DO using a sensor based on Pd porphyrins, which was developed for measuring in vivo oxygen levels [44,45]. Sinaasappel and Ince [44] found that τ_0 of Pd porphyrin decreased much more sharply with temperature, from 690 μs at 10°C to 580 μs at 38 °C, i.e., a decrease of 16% over ΔT=28 °C. Tsukada et al. [45] also found that τ_0 decreased much more sharply with temperature, from 470 μs at 20°C to 300 μs at 45°C, i.e., a decrease of 36% over ΔT=25°C. In general, it is believed that the temperature dependence of τ_0 and τ probably results from the temperature dependence of oxygen/Ar solubilities and solvent vibrations.

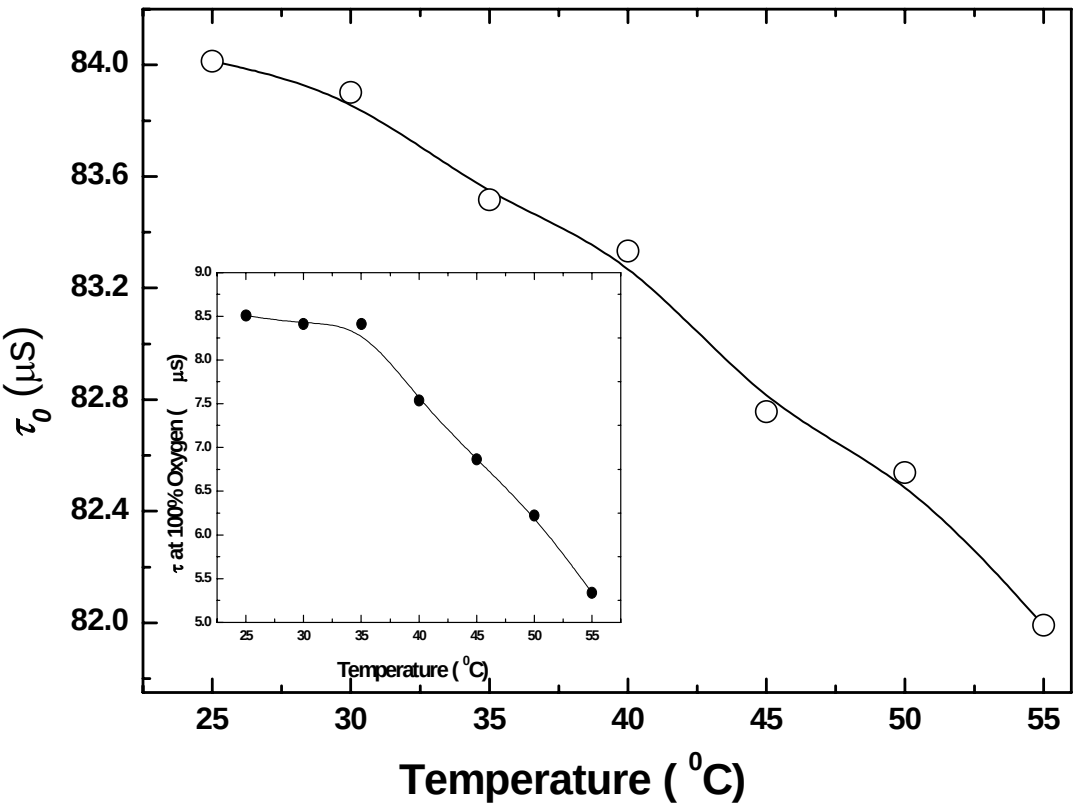

Figure 8. Effect of temperature on τ_0 and τ at 100% O_2 (inset) for an Alq_3/PtOEP sensor measuring dissolved oxygen in water. The lines are a guide to the eye.

In summary, it is clear that structurally integrated OLED based sensors are suitable for detection of dissolved oxygen in water and other solvents. The detection sensitivities using the PL lifetime mode are relatively high and the sensors are suitable for measurements at a temperature range of 23–60 ˚C. Additional studies are still needed to optimize the PL-based DO sensors for real-world applications, through the choice of the dye, the film material, and the sensor design.

5.4 Conclusion

Based on the performance of the oxygen sensors described in this work, the use of OLEDs as excitation sources in PL-based chemical and biological sensors is promising. The ease of OLED fabrication and OLED/sensing component structural integration result in compact devices, which are expected to be inexpensive and suitable for real-world applications. The example of oxygen sensing demonstrates the viability of the approach in using the PL lifetime detection mode, where small changes in the intensity of the excitation source, dye leaching or stray light have a minimal effect on the sensor response. In evaluating the OLED-based platform for oxygen sensing, a new assessment of PtOEP-based sensors in terms of PtOEP aggregation, and the effects of film composition and measurement temperature on the PL lifetime was obtained.

The availability of OLEDs with EL spectra covering a wide spectral range makes them attractive for use with various fluorophores. In particular, OLED arrays with different color pixels that are individually addressable have been developed. Such arrays are attractive for developing small-size sensor arrays for multianalyte detection. Current studies focus on such studies and on a structural integration of not only the OLED/sensing component, but also the photodetector.

5.5 Acknowledgements

This work was supported by NIH Grant 1 R43 EB001513- 01A1, NASA Grant NAG-1-02098, NSF Grants CHE-0345189 and ECS-0428220, the Institute for Physical Research and Technology of Iowa State University (ISU), and by the Director for Energy Research,

Office of Basic Energy Science, USDOE. Ames Laboratory is operated by ISU for USDOE under Contract W-7405-Eng-82.

5.6 References

[1] J.W. Aylott, Z. Chen-Esterlit, J.H. Friedl, R. Kopelman, V. Savvateev, J. Shinar, US Patent No. 6,331,438 (December 2001).

[2] V. Savvate'ev, Z. Chen-Esterlit, J.W. Aylott, B. Choudhury, C.-H. Kim, L. Zou, J.H. Friedl, R. Shinar, J. Shinar, R. Kopelman, Appl. Phys. Lett. **81,** 4652 (2002).

[3] B. Choudhury, R. Shinar, J. Shinar, J. Appl. Phys. **96,** 2949 (2004).

[4] B. Choudhury, R. Shinar, J. Shinar, Organic light emitting materials and devices VII, in: Z.H. Kafafi, P.A. Lane (Eds.), SPIE Conference Proceedings, vol. **5214**, SPIE, Bellingham, WA, 2004, p. 64.

[5] R. Shinar, B. Choudhury, Z. Zhou, H.-S. Wu, L. Tabatabai, J. Shinar, Smart medical and biomedical sensor technology II, in: B.M. Cullum (Ed.), SPIE Conference Proceedings, vol. **5588**, SPIE, Bellingham, WA, 2004, p. 59.

[6] C.S. Burke, O. McGaughey, J.-M. Sabattie, H. Barry, A.K. Mcevoy, C. McDonagh, B.D. MacCraith, Analyst **130,** 41 (2005).

[7] W. Trettnak, W. Gruber, F. Reininger, I. Klimant, Sens. Actuators B **29,** 219 (1995).

[8] D.B. Papkovsky, G.V. Ponomarev, W. Trettnak, P. O'Leary, Anal. Chem. **67,** 4112 (1995).

[9] Z. Rosenzweig, R. Kopelman, Anal. Chem. **67**, 2650 (1995).

[10] S.-K. Lee, I. Okura, Anal. Commun. **34**, 185 (1997).

[11] C. McDonagh, B.D. MacCraith, A.K. McEvoy, Anal. Chem. **70**, 45 (1998).

[12] D. Garcia-Fresnadillo, M.D. Marazuela, M.C. Moreno-Bondi, G. Orellana, Langmuir **15**, 6451 (1999).

[13] Y. Amao, K. Asai, T. Miyashita, I. Okura, Polym. Adv. Technol. **11**, 705 (2000).

[14] Y. Amao, Microchim. Acta **143**, 1 (2003).

[15] Y.-E.L. Koo, Y. Cao, R. Kopelman, S.M. Koo, M. Brasuel, M.A. Philbert, Anal. Chem. **76**, 2498 (2004).

[16] R.N. Gillanders, M.C. Tedford, P.J. Crilly, R.T. Bailey, Anal. Chim. Acta **502**, 1 (2004).

[17] P.A.S. Jorge, P. Caldas, C.C. Rosa, A.G. Oliva, J.L. Santos, Sens. Actuators B **103**, 290 (2004).

[18] C. Prininger, I. Klimant, O.S. Wolfbeis, Anal. Chem. **66**, 1841 (1994).

[19] Y. Amao, T. Miyashita, I. Okura, Analyst **125**, 871 (2000).

[20] A.K. McAvoy, C.M. McDonagh, B.D. MacCraith, Analyst **121**, 785 (1991).

[21] S.-K. Lee, I. Okura, Spectrochim. Acta A **54**, 91 (1998).

[22] C. McDonagh, B.D. MacCraith, A.K. McEvoy, Anal. Chem. **70**, 45 (1998).

[23] D.B. Papkovsky, J. Olah, I.V. Troyanovsky, N.A. Sadovsky, V.D. Rumyantseva, A.F. Mironov, A.I. Yaropolov, A.P. Savitsky, Biosens. Bioelectron. **7**, 199 (1992).

[24] Emagin Corporation, OLED display, 2003, <www.emagincorp.com>.

[25] G. Gustafsson, Y. Cao, G.M. Treacy, F. Klavetter, N. Colaneri, A.J. Heeger, Nature **357**, 447 (1992).

[26] Universal Display Corporation, OLED display, 2004, <www.universaldisplay.com>.

[27] Sony, OLED display, 2004, <www.sony.com>, Toshina, OLED display display, 2004, <www.toshiba.co.jp>, Pioneer, OLED display, 2004, <www.pioneer.co.jp>, Samsung, OLED display, 2004, <www.samsung.co.kr>.

[28] T. Tsutsui, M.-J. Yang, M. Yahiro, K. Nakamura, T. Watanabe, T. Tsuji, Y. Fukuda, T. Wakimoto, S. Miyaguchi, Jpn. J. Appl. Phys. **38**, L1502 (1999).

[29] M.A. Baldo, S. Lamansky, P.E. Burrows, M.E. Thompson, S.R. Forrest, Appl. Phys. Lett. **75**, 4 (1999).

[30] C. Adachi, M.A. Baldo, S.R. Forrest, M.E. Thompson, Appl. Phys. Lett. **77**, 904 (2000).

[31] C. Adachi, R.C. Kwong, P. Djurovich, V. Adamovich, M.A. Baldo, M.E. Thompson, S.R. Forrest, Appl. Phys. Lett. **79**, 2082 (2001).

[32] H. Spreitzer, H. Schenk, J. Salbeck, F. Weissoertel, H. Riel, W. Reiss, Organic light emitting materials and devices, in: Z.H. Kafafi (Ed.), SPIE Conference Proceedings, vol. **3797**, SPIE, Bellingham, WA, 1999, p. 316;

F. Steuber, J. Staudigel, M. St¨ossel, J. Simmerer, A. Winnacker, H. Spreitzer, F. Weiss¨ortel, J. Salbeck, Adv. Mater. **12**, 130 (2000).

[33] V. Savvate'ev, J.H. Friedl, L. Zou, J. Shinar, K. Christensen, W. Oldham, L.J. Rothberg, Z. Chen-Esterlit, R. Kopelman, Appl. Phys. Lett. **76**, 1501 (2000).

[34] K.O. Cheon, J. Shinar, Appl. Phys. Lett. **81**, 1738 (2002).

[35] G. Li, J. Shinar, Appl. Phys. Lett. **83**, 5359 (2003).

[36] L. Zou, V. Savvate'ev, J. Booher, C.-H. Kim, J. Shinar, Appl. Phys. Lett. **79**, 2282 (2001).

[37] V.G. Kozlov, G. Parthasarathy, P.E. Burrows, S.R. Forrest, Y. You, M.E. Thompson, Appl. Phys. Lett. **72**, 144 (1998).

[38] S.E. Shaheen, G.E. Jabbour, M.M. Morell, Y. Kawabe, B. Kippelen, N. Peyghambarian, M.-F. Nabor, R. Schlaf, E.A. Mash, N.R. Armstrong, J. Appl. Phys. **84**, 2324 (1998).

[39] L.S. Hung, C.W. Tang, M.G. Mason, Appl. Phys. Lett. **70**, 152 (1997).

[40] Z.J. Fuller, D.W. Bare, K.A. Kneas, W.-Y. Xu, J.N. Demas, B.A. DeGraff, Anal. Chem. **75**, 2670 (2003).

[41] K.O. Cheon, J. Shinar, Appl. Phys. Lett. **83**, 2073 (2003).

[42] D.B. Papkovsky, G.V. Ponomarev, W. Trettnak, P. O'leary, Anal. Chem. **67**, 4112 (1995).

[43] W.F. Linke, Solubilities of Inorganic and Metal–Organic Compounds, American Chemical Society, Washington, DC, 1958; J.M. Hale, Technical Notes, Orbisphere Laboratories, NJ, 1980; M. Vadekar, PTQ Winter 2002/03, p. 87, (http://www.eptq.com/Pages/Articles/Winter0203/Winter0203 pdf/PTQ03107.pdf).

[44] M. Sinaasappel, C. Ince, J. Appl. Physiol. **81**, 2297 (1996).

[45] K. Tsukada, S. Sakai, K. Hase, H. Minamitani, Biosens. Bioelectron. **18**, 1439 (2003).

6. ENHANCED PHTOTLUMINESCENCE OF OXYGEN SENSING FILMS THROUGH DOPING WITH HIGH DIELECTRIC CONSTANT PARTICLES

Zhaoqun Zhou,[1] Ruth Shinar,[2]* and Joseph Shinar[1]*

[1]*Ames Laboratory – USDOE and Department of Physics and Astronomy*

Iowa State University, Ames, IA 50011

[2]*Microelectronics Research Center, Iowa State University, Ames, IA 50011*

Submitted for publication in Advanced Functional Materials

Abstract

A uniquely simple approach to increase the intensity of the photoluminescence (PL) of dye-doped sensor films is demonstrated for oxygen sensors, where the sensor film, i.e., Pt or Pd octaethylporphyrin (PtOEP or PdOEP, respectively)-doped polystyrene, is additionally doped with small-size particles that have a high dielectric constant, such as 360 nm-diameter titania (TiO_2) particles. When excited by an organic light emitting device (OLED), the dye PL intensity increases up to ~10 fold, depending on the TiO_2 concentration and the excitation source. The enhanced PL is attributed to light scattering by the embedded particles and possibly by voids in the film. The particles scatter the light that excites the PL, increasing the optical path of the exciting light and consequently the absorption of that light and the PL. The particles can also result in an increase in the PL outcoupling, reducing waveguiding to the film edges. The increased PL results in an improved signal-to-noise (S/N) ratio in oxygen monitoring, without any deterioration or change in the response time or the long-term stability of the sensor films. In addition, at a given O_2 level, the dye PL decay time τ increases in the presence of the particles, but is independent of their concentration in the measured range. The improved S/N can improve the analyte limit of detection, allow

shortened data acquisition times, and enable the use of low-intensity excitation sources to minimize potential dye photobleaching. In particular, it improves the performance of structurally integrated OLED-based chemical and biological sensors, which are drawing increasing attention due to their uniquely simple and flexible integration geometry.

6.1 Introduction

In general, photoluminescence (PL)-based (bio)chemical sensors include a luminescent sensing element (the PL of which is analyte-sensitive), a light source that excites that element, a photodetector (PD), a power supply, and the electronics for signal processing. Typical light sources include lasers, lamps, and inorganic light-emitting diodes (LEDs). Recently, organic LEDs (OLEDs) have been introduced as promising light sources for such applications due to the ability to structurally integrate them with the sensor film in a uniquely simple geometry[1-6]. Therefore, they were used as the excitation sources in this work.

The field of luminescent chemical and biological sensors, which detect changes in the PL intensity I or decay time τ caused by the analyte, has been growing rapidly[1-29]. Yet in spite of their potential widespread applications, simple, low-cost approaches that further improve sensor performance are highly desired. Enhancement of the detection sensitivity is often achieved with new matrices that are more permeable to the analyte, with dyes with a high PL quantum yield and/or a long τ, and by optimizing the dye concentration when embedded in a thin host film, immobilized on a surface, or dissolved in solution. These approaches improve the signal-to-noise ratio (S/N) in the measurement, enabling more accurate determination of analyte levels. However, new methods are desired for signal enhancement beyond the incremental increases obtained by the approaches mentioned above.

This paper demonstrates such strong increases obtained by doping the sensor films with high dielectric constant particles such as titania (TiO_2).

6.1.1 Principle of PL-based oxygen sensors

PL-based oxygen sensors have been extensively research[2-6, 8-10, 13, 16-18, 21-29]. Typically, an oxygen-sensitive dye, such as Pt octaethylporphyrin (PtOEP), is embedded in a thin polymeric matrix. Collisions of oxygen molecules with the dye result in quenching of I and shortening of τ; ideally, the inverse of both is linear with O_2 concentration [O_2] (see below). Coupling the oxygen sensing film with specific enzymes results in biosensors for, e.g., glucose, alcohol, and lactate[4,5,13], enabling fabrication of a multianalyte sensor array, in particular when using an OLED pixel array as the excitation source[4,5]. Monitoring oxygen through τ is advantageous over I, since τ is independent of variations in the intensity of the excitation source or minor deterioration of the sensing film, though the decay curves, from which τ is obtained, are often non-exponential[28].

Ideally, the relation between [O_2] and I and τ is given by the Stern-Vollmer (SV) equation

$$I_0/I = \tau_0/\tau = 1 + k_{SV}[O_2] \quad (1)$$

(where I_0 and τ_0 are the unquenched values), although deviations from that linear relation are quite common[6,28,29].

6.1.2 Sensing films

In response to the diverse applications of PL-based oxygen sensors, a wide range of probes have been developed, providing high sensitivity, selectivity, long term stability, and

reversibility. Common dyes used in such sensors include luminescent ruthenium complexes and Pt- and Pd-porphyrins[6,16,17,26]. The dyes are attractive due to their long τ_0, which ensures high detection sensitivity. For example, τ_0(PtOEP) ~ 100 μs and τ_0(PdOEP) ~ 1 ms[6,16,17,26].

Matrices in which the oxygen-sensitive dyes are embedded are important in shaping the sensor performance. To ensure high sensitivities and fast response times, the matrix should be highly permeable to oxygen, but it should also entrap the dye so that its leaching is avoided. Examples of matrices include sol-gel films, poly(dimethylsiloxane) (PDMS), fluoropolymers, and polystyrene (PS). The sensor films are fabricated using various techniques, such as spray-, drop-, dip-, and spin-coating. The dye molecule concentration and the matrix material, as well as the film fabrication conditions, are optimized to improve the sensor performance, including the limit of detection (LOD). High concentrations of dye molecules can lead to their aggregation and consequently, self-quenching. Additionally, high concentrations will result in absorbance of the exciting light near the surface, reducing the PL signal[22]. Low dye concentrations will result in weak signals, in particular at high analyte concentrations that strongly quench the PL, as in oxygen sensors.

Embedding nanoparticles in sensor films has also been employed to enhance the performance of oxygen sensors. Typically, modified silica nanospheres or mesoporous silica were used[22, 23]. Silica fillers embedded in a sensor film improve the mechanical strength of films made of soft (low glass transition temperature) polymers and/or serve as carriers for the dye molecules. The particles can affect the oxygen diffusion rate and path in the film, as well as aggregation of dye molecules. Moreover, O_2 can adsorb onto the particles' surface, resulting in complex oxygen transport and PL quenching mechanisms. A large filler volume fraction and mesoporous silica can also generate voids in the films. Such voids scatter light,

affect the optical properties of the film, increase the surface area exposed to the gas-phase, and can result in faster sensor response[22, 23].

In this work, we present a new approach to enhance the PL intensity in oxygen and oxygen-based sensors by co-embedding the sensor films with high dielectric constant TiO_2 nanoparticles (refractive index ~2.8 around 590 nm) [24]. In using this simple approach, an up to ~10 fold enhancement in the PL is obtained. However, in the presence of O_2, τ increases in comparison to its values in the absence of the particles. The effect of TiO_2 concentration on the PL intensity and lifetimes in various environments and for different excitation sources and intensities is described. The enhanced PL intensity is discussed in terms of increased electroluminescence (EL) and PL optical lengths, and PL outcoupling.

6.1.3. OLED-based bio(chemical) sensors

The OLED-excited, structurally integrated, PL-based sensing platform has been described in previous reports[1-6]. In brief, the small-molecular OLED matrix arrays are fabricated on an indium tin oxide (ITO)-coated glass substrate; the ~100 nm-thick ITO is etched to yield 2 mm-wide strips. The organic layers, with a total thickness of ~100 nm, the 1 nm-thick CsF buffer layer, and the perpendicular 2 mm-wide, 100 – 150 nm-thick Al cathode strips are then thermally evaporated on these ITO strips in a low-vacuum (~10^{-6} Torr) chamber. The 2×2 mm^2 OLED pixels are consequently defined by the overlap between the ITO and the Al strips. The (typically 2×10) OLED pixel array is encapsulated by attaching a glass cover to the substrate with Torr Seal™ high-vacuum epoxy.

The ~20 μm-thick sensor film is typically drop-cast on the other side of the OLED pixel array glass substrate or on a separate glass substrate that is attached back-to-back to the

OLED substrate. The thickness of the resulting OLED/sensor film module is consequently determined by that of the glass substrates and encapsulating OLED cover (typically ~2 mm).

6.2 Results and Discussion

6.2.1 Sensing films

The materials used to fabricate the oxygen sensing films included the oxygen-sensitive dyes PtOEP and PdOEP, the PS matrix, and 360 nm diameter DuPont TiO_2 particles, which were co-embedded with PtOEP or PdOEP in the PS matrix to enhance the PL. The TiO_2 surfaces are coated with a thin polymeric layer to improve dispersibility; a thin alumina/silica barrier layer between the TiO_2 surface and the organic layer protects the latter from photodegradation[31]. The PtOEP or PdOEP, PS, and titania concentrations in the toluene solutions used for film fabrication were 1 mg/mL, 50 mg/mL, and 0.25 to 8 mg/mL, respectively. Typically, the sensor films were prepared by drop casting 60 μL of the solution onto the glass substrate; the resulting films were all ~ 6 μm thick as measured with a Sloan Dektak II Profilometer. The PtOEP dye was used for monitoring gas-phase and dissolved oxygen (DO) in water; PdOEP was used for monitoring DO only.

Fig. 1 shows a simplified schematic of the multiple scattering/refraction of the EL and PL in a TiO_2-doped dye: PS sensing film excited by an OLED in a “back-detection” configuration, i.e., where the sensor films is "in front" of the OLED array while the PD is located "behind" it. At low TiO_2 concentrations (< 3 mg/mL) in the solution used for film preparation, the nanoparticles are dispersed largely evenly within the resulting polymeric

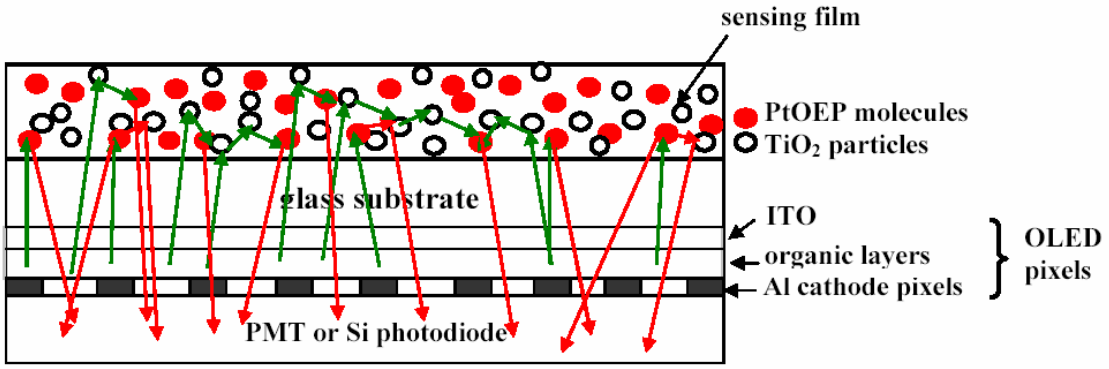

Figure 1. Schematic of the structurally integrated OLED-based oxygen sensor (not to scale). The photodetector, a PMT or Si photodiode, is behind the OLED pixel array. The TiO2 nanoparticles, which are embedded in the dye:PS sensing film, act as a scattering medium.

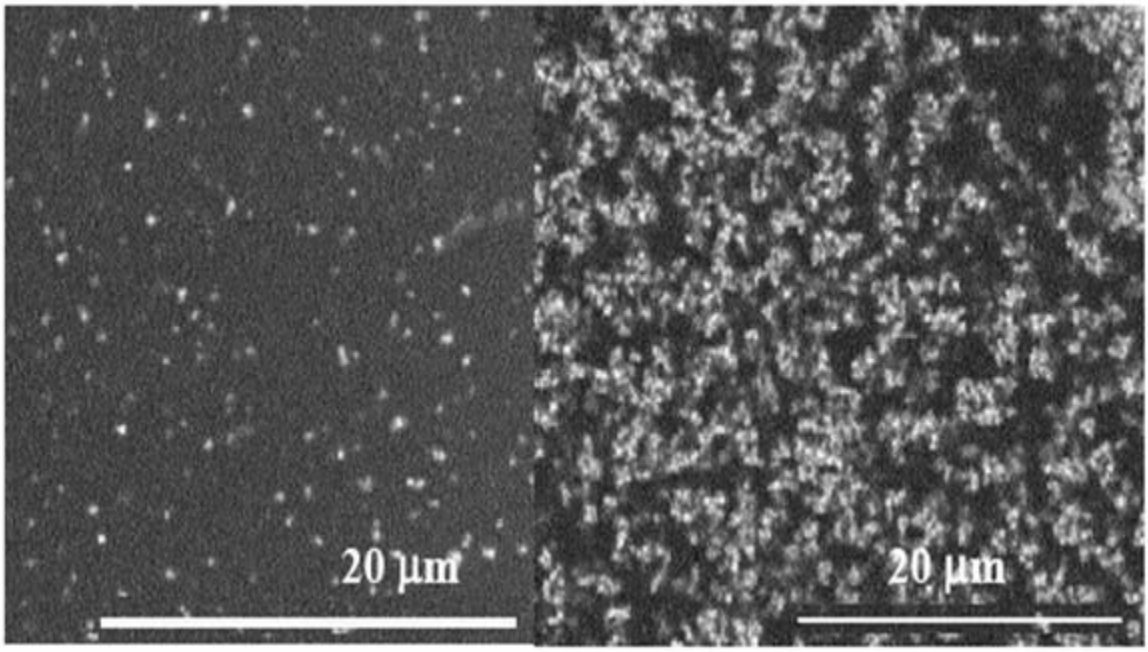

Figure 2. SEM images of PS films doped with PtOEP and titania particles. (a) 2 mg/mL TiO2 in the solution used for film fabrication, (b) 8 mg/mL particles.

film, as shown in the SEM image (Fig. 2a) for 2 mg/mL titania. As the TiO_2 concentration increases, the particles tend to cluster throughout the film (Fig. 2b; 8 mg/mL particles).

Indeed, the films become hazy as the titania concentration increases, indicating the formation of such particle aggregates.

As shown and detailed below, the PL signal is enhanced in the presence of titania particles. This is due to the high refractive index of the TiO_2 particles, which act as excellent scattering centers. These scattering centers increase the optical path of the exciting photons, consequently increasing their absorption by the PtOEP/PdOEP dye molecules. Additionally, similar scattering of the PL photons should decrease their waveguiding to the film edges and increase their outcoupling to the surface of the film, further enhancing the PL that is collected by the PD.

6.2.2 OLED-based sensors

The OLEDs used for oxygen sensing are based on 4,4'-bis(9-carbazolyl)biphenyl (CBP), with an EL peaking at ~380 nm, and tris(quinolinolate) Al (Alq_3), with an EL peaking at ~535 nm; these EL bands match absorption bands of PtOEP molecules, which have a very intense absorption band at ~380 nm ($S_0 \rightarrow S_2$ electronic transition) and two lower-energy absorption bands at ~500 and ~535 nm ($S_0 \rightarrow S_1$)[32]. The observed PtOEP phosphorescence, peaking at ~645 nm, follows intersystem crossing to the triplet state. Rubrene-doped Alq_3, with an EL peak at ~545 nm, was used for PdOEP excitation, which has an absorption peak at that wavelength.

As mentioned, the PD, a photomultiplier tube or a Si photodiode, was typically placed behind the OLED array, measuring the PL passing through the gaps between the OLED pixels (see Fig. 1)[4-6]. The OLEDs were operated in a pulsed mode with 50-100 μs-long pulses, and a 20 Hz repetition rate. The PL decay curves were obtained following the OLED

pulse as this mode of operation eliminated the need for optical filters that would block the EL from the PD.

6.2.3 PL spectra of TiO_2-doped sensing films

6.2.3.1 Excitation at ~535 nm by an Alq_3 OLED

Fig. 3 shows the PL spectra of PtOEP:PS sensing films doped with different TiO_2 concentrations, excited by an Alq_3 OLED; the PL was measured in the reflection mode. The inset of the figure shows the integrated signal enhancement as a function of TiO_2 concentration. As seen, the PL signal increases with increasing TiO_2 concentration, leveling off at ~6-8 mg/mL with a ~10 fold increase. No optical filters were used in obtaining the data shown in Fig. 3. Thus, the background signal is due to the tail of the EL.

The TiO_2-induced PL enhancement may result from several possible mechanisms: (*i*) The high dielectric contrast between the TiO_2 nanoparticles and the surrounding film leads to efficient scattering of the light that excites the PL. As a result, the optical path length of the exciting light increases, and consequently the absorption of that light by the dye, and its PL, as well. (*ii*) Scattering of the exciting light by TiO_2-induced voids may similarly enhance the PL. (*iii*) The PL itself may undergo similar multiple scattering, which may increase its outcoupling to the surface of the film by reducing the waveguiding to its edges. Without the particles, much of the PL, and in particular all of the PL that is incident on the film/air interface at an angle greater than the critical angle, is reflected back into the film. A large fraction of that PL then undergoes multiple reflections until it exits the film at its edges,

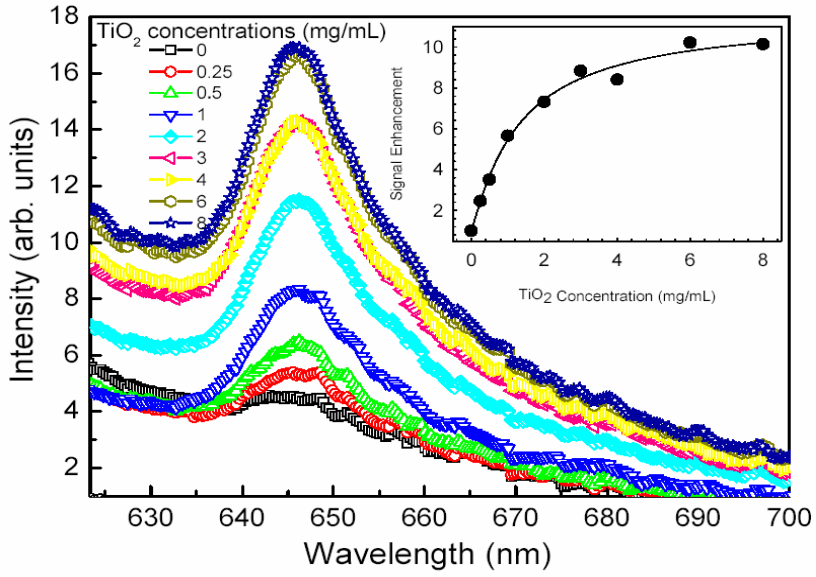

Figure 3. The PL spectra in air, excited at ~530 nm by the Alq_3 OLED, of PtOEP:PS doped with different concentrations of TiO2, measured in reflection geometry. The inset shows the signal enhancement at various TiO2 concentrations.

resulting in a low outcoupling efficiency. With the TiO_2 particles, some of that internally reflected light is scattered by the particles and propagates at angles that enable it to exit the film at its front or back face, thus increasing the outcoupling efficiency.

6.2.3.2 Excitation at ~366 nm by a UV lamp

In an attempt to distinguish between the signal enhancement due to EL scattering by the particles and the other possible mechanisms, we monitored the effect of titania particles on the PL excited by a UV lamp with a broad emission band peaking at 366 nm. Titania particles reflect only ~10% of the light at this wavelength, and therefore the light scattered should be significantly less than at 535 nm, where the reflection is close to 100%. Fig. 4 shows the PL spectra and enhancement as a function of titania particles concentration; the PL

was measured in the reflection mode. As seen, the PL enhancement using that UV excitation reaches a maximal 3 fold enhancement that levels off at ~2 mg/mL titania. The smaller enhancement and the leveling off at the smaller TiO_2 concentration, in comparison to those obtained using the ~535 nm Alq_3 OLED excitation, is likely due to the strong absorption of titania particles at this wavelength. However, it is clear that even 10% reflection can result in signal enhancement. This is plausible if even at 535 nm, only a small fraction of the incident photons excite the PL; the majority of the photons are transmitted through the largely transparent layer.

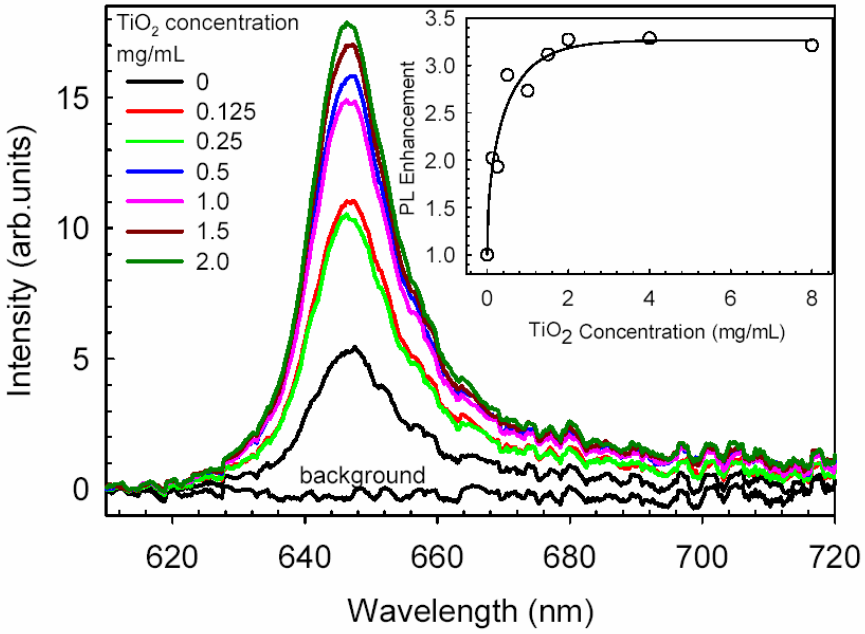

Figure 4. The PL spectra in air, excited at ~366 nm by a UV lamp, of PtOEP:PS doped with different concentrations of TiO2. The inset shows the signal enhancement at various TiO2 concentrations.

Saturation of the absorption by the PtOEP (i.e., photobleaching) will result in leveling off of the enhancement. However, the PL intensity for 0 to 8 mg/mL titania doped films

increased linearly with the excitation intensity, as the latter increased 10 fold. Moreover, the PL enhancement was comparable for all UV lamp intensities in that range. This clearly rules out photobleaching. The effect of multiple scattering of the PL, which results in improved outcoupling (as observed in OLEDs) [33-35], and the scattering by voids, should remain comparable at both excitation wavelengths.

Small matrix-dependent shifts in the excitation and PL spectra (peak emission or band width) induced by silica nanoparticles were reported for PtOEP[22,23]. Such TiO_2 nanoparticle-induced shifts could not be determined, within the experimental error.

Due to the titania-induced PL enhancement, a TiO_2-doped sensing element for e.g., oxygen monitoring, can function with reduced concentrations of dyes while maintaining comparable or improved signal intensities in comparison to sensing elements with larger dye concentrations, but no titania particles. Reducing the dye concentration can minimize aggregation of dye molecules in the sensing film, which results in quenching of the PL intensity. As expected and shown below, the addition of the particles improves the S/N, which should enable faster O_2 monitoring with a reduced number of recorded signals that are needed for noise reduction.

6.2.4 The performance of an OLED-excited, TiO_2-doped oxygen sensor film

In testing the effects of TiO_2 doping on the performance of OLED-based, structurally integrated oxygen sensors, the PL intensity and decay time of PtOEP:PS and PdOEP:PS following the pulsed OLED excitation were monitored for sensing films doped with different TiO_2 concentrations; both gas-phase oxygen and DO in water were monitored.

Fig. 5 shows the effect of titania on the PL decay curve and on the EL of the Alq_3 OLED in a 100% Ar environment at room temperature. It shows the intensity measured by the PD during and following the 50 μs Alq_3 OLED pulse at different concentrations of titania

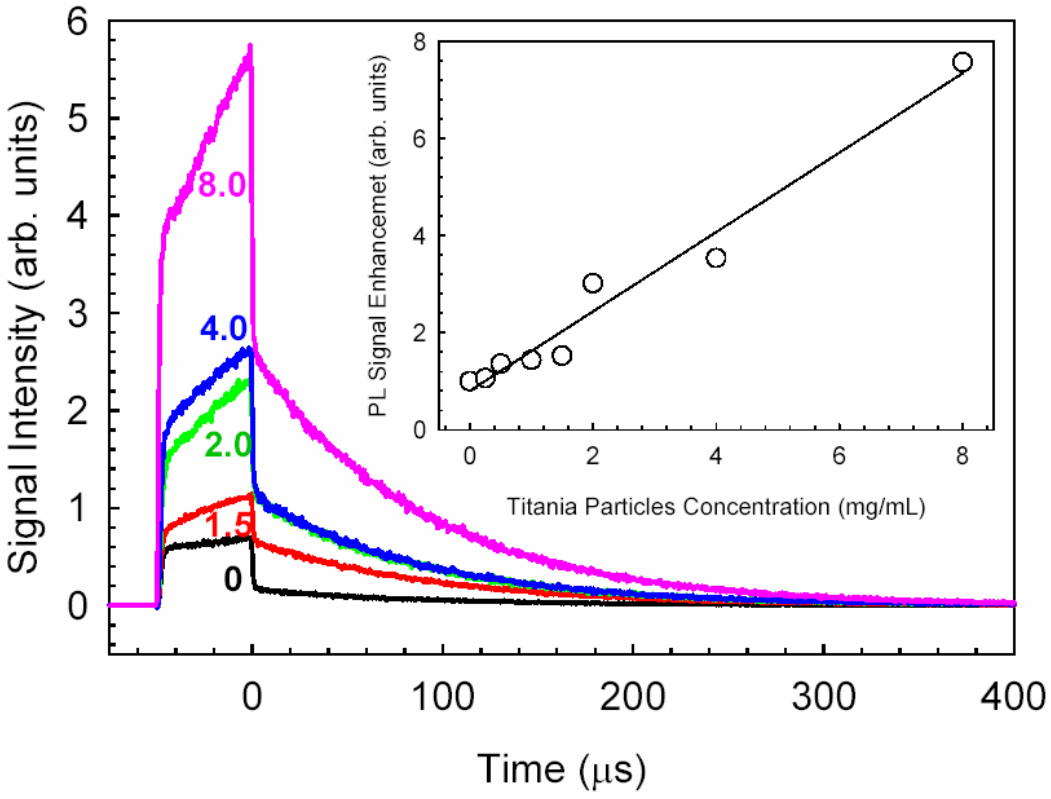

Figure 5. The effect of titania particles on the PtOEP:PS PL decay curves and on the EL of the Alq3 OLED in a 100% Ar environment at room temperature. Shown is the intensity measured by the PD during and following the 50 μs Alq3 OLED pulse at different concentrations of titantia particles.

particles. A 610 nm long-pass filter was used, so that only a small fraction of the EL was detected by the PD. As seen, for a given film, there is an initial fast increase in the intensity, which is due to the EL. This sharp increase is followed by a gradual increase due to the PtOEP PL. As $\tau_0 \sim 90$ μs, the PL intensity did not reach a steady-state value after the 50 μs of the pulse duration. As the OLED pulse is turned off, a fast decrease in the intensity, due to

the fast decay of the EL, is first seen, followed by the PtOEP PL decay. The significant enhancement of the PL intensity (by up to a factor of ~8) due to the addition of TiO_2 is clearly demonstrated in the inset of this figure. However, the nature of the difference between the linear behavior observed in this case, *vs* the nonlinear increase shown in Fig. 3, where saturation sets in above 2 mg/mL titania, is not clear.

In addition to the effect of the titania particles on the PtOEP: PS PL, Fig. 5 shows that the EL intensity that is detected by the PD also increases with increasing concentration of the TiO_2 particles, as expected. In previous experiments[22], a ~2 fold increase in the intensity of the ~535 nm band was observed in the pulsed laser excitation spectrum of PtOEP embedded together with silica nanospheres in a PDMS film.

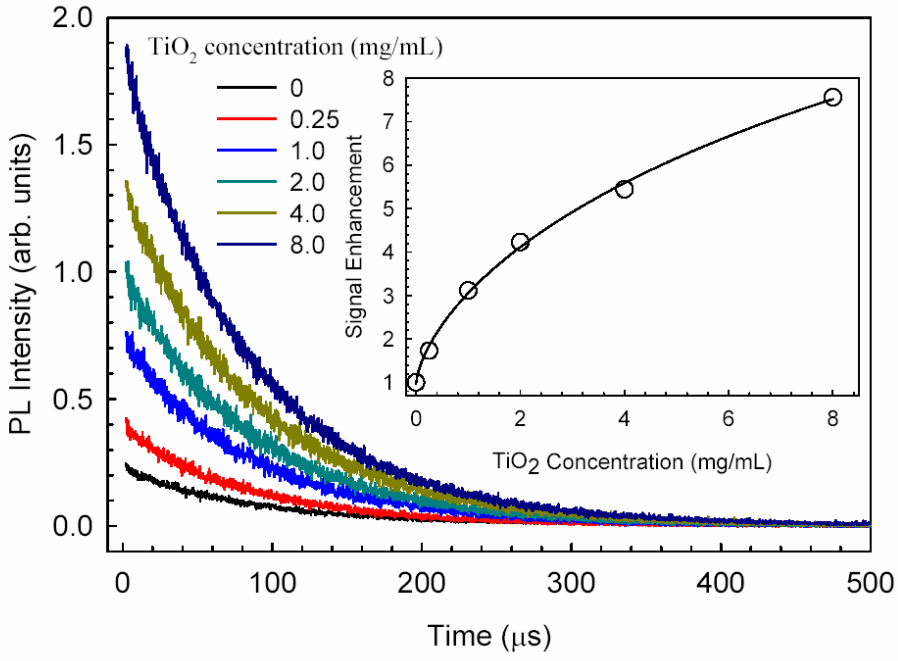

Figure 6. The PtOEP PL decay curves in 100% Ar excited by UV-violet CBP OLED (~380 nm EL peak) at different TiO2 doping concentrations.

Fig. 6 shows the PtOEP PL decay curves in 100% Ar excited by the ~380 nm emission from a UV-violet CBP OLED at different TiO_2 doping concentrations. At 380 nm the titania particles' reflectance is ~13%. As clearly seen, a ~8-fold enhancement was observed for 8 mg/mL titania. Thus Figs. 5 and 6 show that the PL enhancement at 8 mg/mL titania is comparable for Alq_3 and CBP excitations; at lower titania concentrations, CBP showed a somewhat larger enhancement. This is surprising in view of the stronger reflectance of the particles at 535 nm (the Alq_3 EL peak), but may be due to the significantly stronger absorption of PtOEP at 380 nm relative to its absorption at 535 nm. It may provide another indication, consistent with that provided by excitation with the UV lamp, that a large fraction of the EL photons are not absorbed by the dye, so that a reflectance of ~13% (with increased absorption) is sufficient to generate a comparable enhancement.

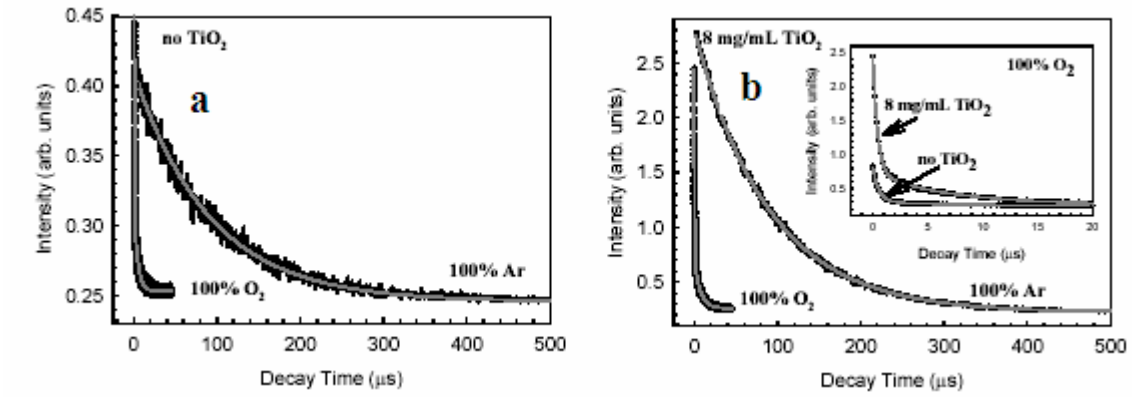

Figure 7. The PL decay curves in 100% Ar and 100% O2 environments (a) for a film without titania and (b) for a film with 8 mg/mL titania. The inset in Fig. 7b shows the expanded decay curves in 100% O2 for the two films. The exponential fit for 100% Ar and bi-exponential fit for the 100% O_2 data are also shown.

While the PL intensities were clearly enhanced in the presence of the titania particles, the PL decay times in oxygen-containing environments, but not in 100% Ar, were longer. As such, the detection sensitivities, defined as τ_0/τ(100% oxygen), were lower. In 100% Ar the

decay curves were independent of the TiO_2 concentration, and could be fitted successfully to a single exponential decay. This behavior indicates that there is no dye aggregation in the sensing film and that the O_2-sensitive dye is probably distributed within the polymeric matrix rather than adsorbed on the TiO_2 particles' surface[22].

In the presence of oxygen, the PL decay curves deviated significantly from a simple exponent. This behavior is commonly observed with O_2 sensors, and several approaches have been described to analyze the observed decay[29]. The data presented in this work were fitted successfully to a biexponential decay. Fig. 7 shows the decay curves in 100% Ar and 100% O_2 environments for a film without titania (Fig. 7a) and for a film with 8 mg/mL titania (Fig. 7b). The inset in Fig. 7b shows the expanded decay curves in 100% O_2 for the two films. The exponential fit for 100% Ar and biexponential fit for the 100% O_2 data are also shown. As seen, the intensity is increased and the S/N is improved when doping with titania. The effective decay time, τ_{eff}, can be defined as the weighted average of the two exponential decay constants τ_1 and τ_2

$$\tau_{eff} = \sum A_i \tau_i / \sum A_i \qquad (2)$$

In 100% O_2, τ_{eff} for the two films were 1.5 μs in the absence of titania, and ~3.5 μs in the doped film. The slower decay time for the titania-doped film is seen clearly in the inset of Fig. 7(b).

Fig. 8 shows the SV plots (see Eq. 1) (τ_0/τ_{eff} vs % O_2) for the 0, 2, and 8 mg/mL films. As seen from the plots, the values of τ_{eff} are longer for the titania-doped films in O_2-containing atmospheres, and the SV plots are similar for films with 2 to 8 mg/mL titania. This behavior, in particular the independence of τ_{eff} on the titania level, is not clear. It is

possible that the titania particles affect the permeability of oxygen, impede oxygen diffusion within the film, and consequently increase the diffusion path, or block O_2 access to the PtOEP molecules. However, these effects, in contrast to the experimental observation, are expected to be more pronounced as the titania concentration increases. In a study by Lu et al.[22], a decrease in the diffusion rate of oxygen with increasing content of silica nanospheres in a PtOEP:PDMS film was attributed to silica particles acting as obstacles to oxygen diffusion.

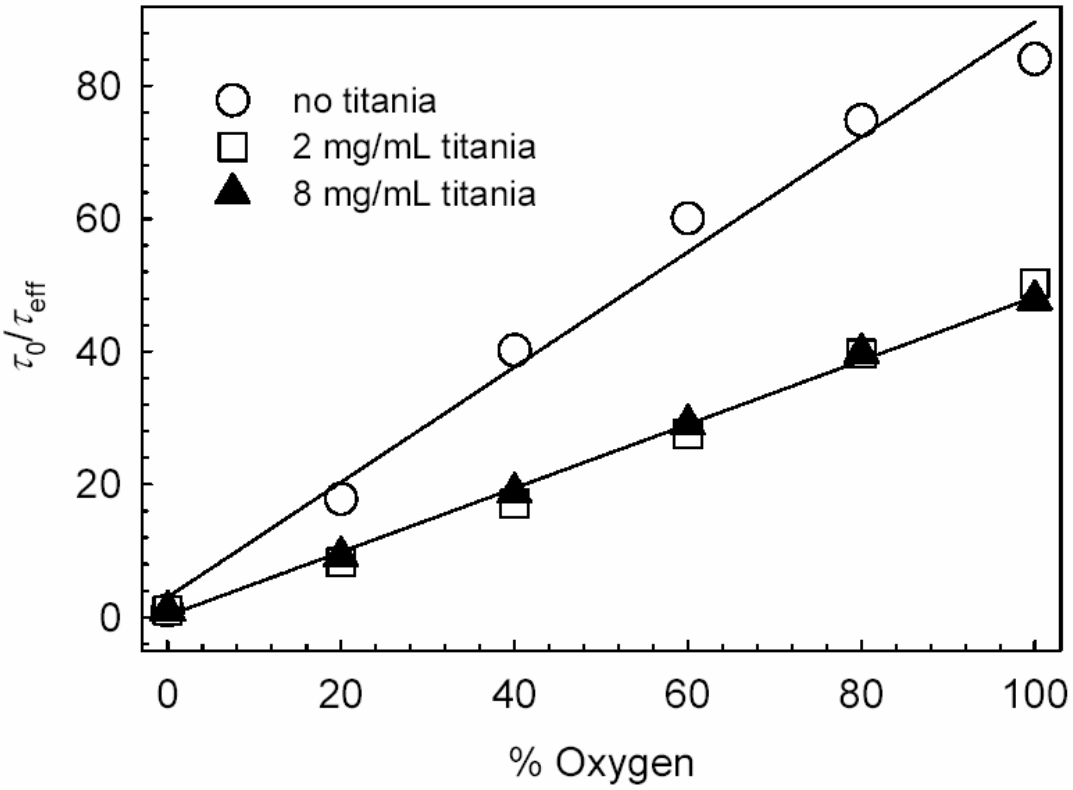

Figure 8. The gas-phase SV plots (see Eq. 1; τ_0/τ_{eff} vs % O2) for films prepared from solutions containing 0, 2, and 8 mg/mL TiO2.

The data presented above was for gas-phase O_2 sensing. A similar qualitative signal enhancement was observed also in monitoring DO. Fig. 9 shows the decay curves and the exponential and bi-exponential fitting in Ar- and O_2-saturated solutions, respectively, for

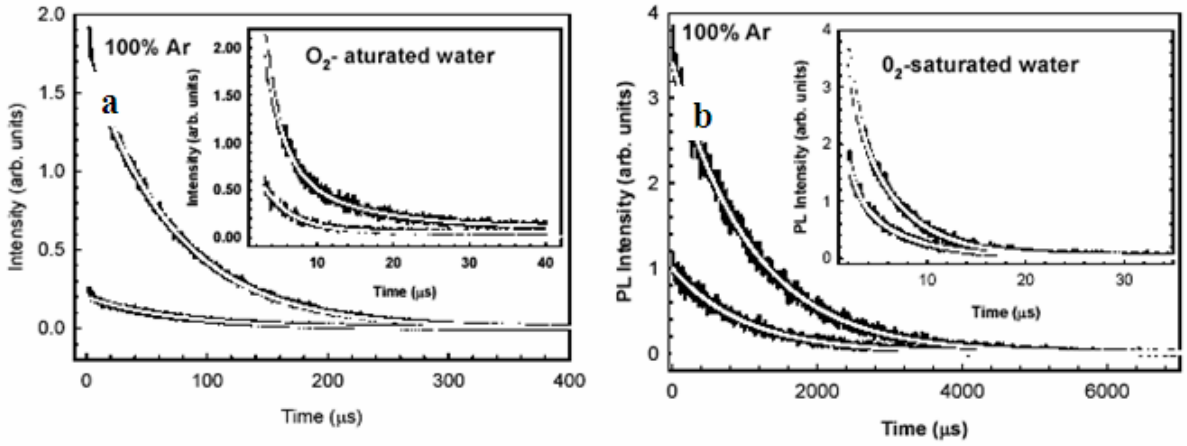

Figure 9. The PL decay curves in Ar- and O2-saturated solutions for PtOEP (a) and PdOEP (b); the exponential and bi-exponential fitting, respectively, are also shown.

PtOEP and PdOEP. The signal enhancement is clear in both cases. Fig. 10 shows the effect of TiO_2 concentration on the signal enhancement of PtOEP in air-saturated water. The behavior is qualitatively similar to that observed for gas-phase monitoring. We note that the signal enhancement by the TiO_2 particles is strong and reproducible in both gas-phase and water. It depends on the oxygen level, particles concentration, and excitation source; there are small variations among different films. It is expected to depend also on the particle size, with particle size ideally approaching half the light wavelength for enhanced scattering cross section.

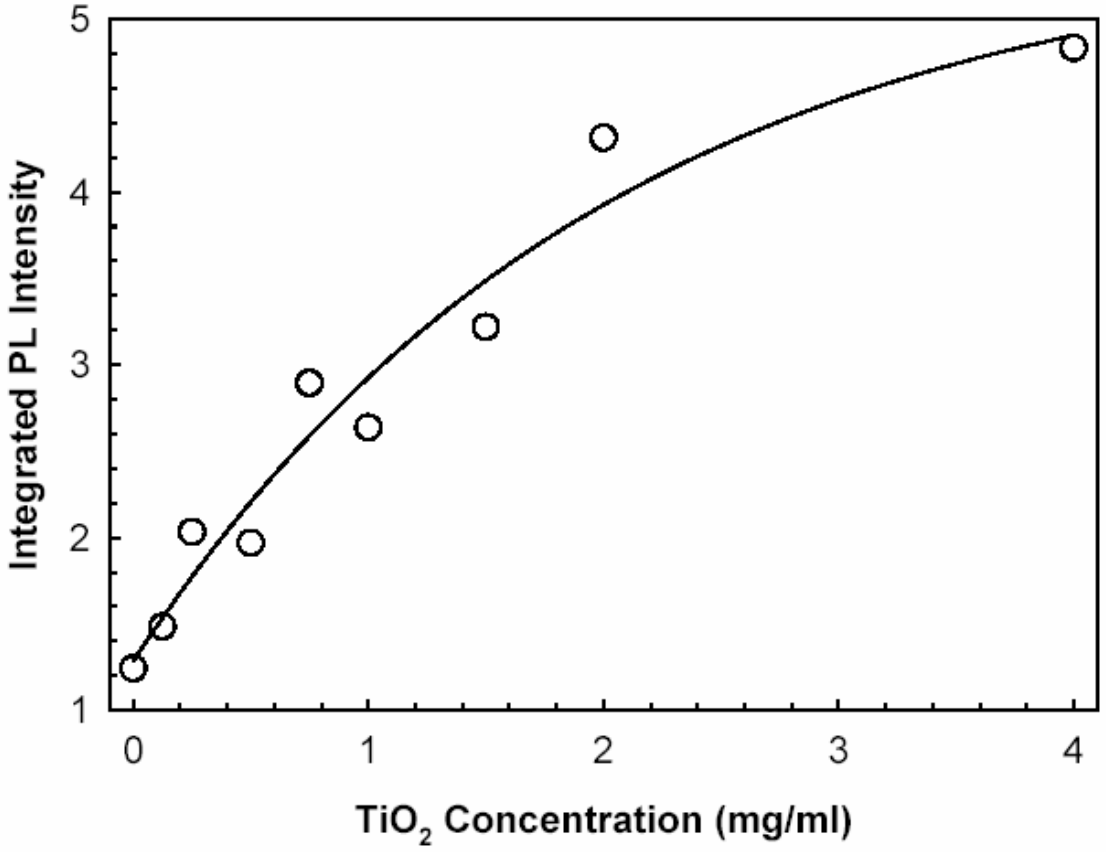

Figure 10. The effect of TiO2 particles concentration on the signal enhancement of PtOEP in air-saturated water.

6.3 Summary

A simple approach to strongly enhance the PL intensity of PtOEP- and PdOEP-doped PS film by co-embedding 360 nm titania particles in the polymeric film was demonstrated. Intensity enhancements of up to x10 relative to the PL intensity of the titania-free films were observed with the PD collecting the reflected light, using two different OLEDs and a UV lamp as the excitation sources. In the gas-phase O_2 and DO sensors, where the sensor film is structurally integrated with its OLED excitation source, such signal enhancement improves

the S/N, which improves the limit of detection and the accuracy of the measurement, in particular for small intensities due to high O_2 levels. Titania doping can allow for the use of lower dye concentrations and weaker excitation sources, which reduce dye aggregation, and consequently self-quenching, and photobleaching, respectively. The signal enhancement is believed to be a result of the large refraction index (2.8) of the particles, which results in efficient scattering of the EL photons within the film, increasing the optical length of the exciting light and consequently the absorption of that light and the PL. Scattering by voids that may be present in the films, in particular at large titania levels, and increased outcoupling of the luminescence may also contribute to the signal enhancement. The EL was increased by TiO_2 particles similarly to the PL. In gas-phase PtOEP-based sensors, the presence of the titania resulted in longer luminescence decay times in O_2 environments, possibly by inhibiting oxygen diffusion. In contrast, the unquenched decay time, which could be fit to a single exponent, was independent of the titania presence, indicating that the dye molecules did not aggregate and were largely dispersed uniformly in the polystyrene.

6.4 Experimental

6.4.1 Materials

TiO_2 nanoparticles, *Ti-Pure*® R-706, with a 360 nm average diameter were obtained from Dupont. The particles are coated with an outer organic layer and a thin silica/alumina barrier layer between the titania and the organic coating. The PtOEP was purchased from H.W. Sands, and polystyrene (molecular weight 45,000) and toluene were purchased from Aldrich.

6.4.2 Sensing film preparation

The sensing films were prepared by drop casting 60 μL of toluene solution that contained PtOEP, PS, and TiO_2 on glass slides. The TiO_2 nanoparticles were ultrasonicated separately in toluene. The particles were then mixed with PtOPE:PS toluene solutions. The PtOEP and PS concentrations were 1 and 50 mg/mL, respectively[6], the TiO_2 concentrations ranged from 0.25 to 8 mg/mL in the solutions used for film fabrication. Prior to drop-casting the solutions, the glass substrates were cleaned by ultasonication in acetone and iso-proponal to remove organic residues. The slides were then dried in Ar. The drop-cast solution was spread evenly onto the cleaned glass substrate. To minimize the nanoparticles' aggregation during film formation, the mixed colloidal solution containing the titania, polymer, and dye molecules was Vortexed for ~1 minute immediately before film fabrication. The films were dried overnight at room temperature in the dark.

6.4.3 OLED fabrication

As received ITO coated glass (Applied Films Corp., 20 $\Omega/\square$) was cleaned with surfactant, acetone and iso-proponal in an ultrasonic bath, followed by 10 minutes of UV-ozone (UVOCS INC. Model: T16X16/0ES) treatment to remove the organic residues. It was then etched to yield 2 mm-wide strips. The sequence of organic layers, with a total thickness of ~100 nm, and 1 nm-thick CsF buffer layer, were deposited on the whole glass/ITO substrate by thermal evaporation in a vacuum chamber (base pressure ~10^{-6} mbar) that is installed in a glove box, in which oxygen and water levels are typically below 1ppm. The 100 – 150 nm-thick Al cathode was deposited in the same chamber through a mask containing 2

mm-wide slits aligned perpendicular to the ITO strips. The deposition rate of the organic materials and cathode were 2 and 4 Å/s, respectively. Since the OLED pixels were defined by the overlap between the ITO and Al strips, they were 2×2 mm^2, with a 2 mm gap between the pixels. The OLED pixel array was encapsulated by gluing a glass cover to the substrate with high vacuum epoxy.

6.4.4 PL decay curves and measurement

The PL spectra of the sensing films were measured with an Ocean Optics CHEM2000 spectrometer. The excitation sources were a two-band UV lamp (Mineralight Lamp: UVGL-58), which generates 254 nm and 366 nm UV light, and Alq_3 and CBP-based OLEDs with EL bands peaking at 535 nm and 380 nm, respectively. The PD was typically a Hamamatsu R6060 photomultiptier (PMT) operated at -650 V. The PL decay curves were recorded on a transient digitizer-Textronix TDS 460 oscilloscope. Measurements were performed in a flow cell with flowing oxygen/argon mixtures, controlled by mass flow controllers MKS multi Gas Controller 147, in which the ratio of oxygen and argon varied, while the total flow was kept constant, thus generating varying oxygen partial pressures. The OLEDs were operated in a pulse mode using an AVTECH: AV-1011-B power supply with a pulse width of 50-100 μs, a bias of 12 V and a repetition rate of 20 Hz. The decay times were obtained from the PL decay curves using exponential or biexponential fitting with a constant background.

6.5 Acknowledgements

Ames Laboratory is operated by Iowa State University for the U.S. Department of Energy under Contract No. W-7405-Eng-82. The work at the Ames Laboratory was partially

supported by the Director for Energy Research, Office of Basic Energy Sciences, DOE, NASA Grant NAG-1-02098, and NSF Grant ECS-0428220.

6.6 References

[1] J. W. Aylott, Z. Chen-Esterlit, J. H. Friedl, R. Kopelman, V. Savvateev, and J. Shinar, US Patent No. 6,331,438 (December 2001).

[2] B. Choudhury, R. Shinar, and J. Shinar, in *Organic Light Emitting Materials and Devices VII,* edited by Z. H. Kafafi and P. A. Lane, SPIE Conf. Proc. **5214**, 64 (2004).

[3] R. Shinar, B. Choudhury, Z. Zhou, H.-S. Wu, L. Tabatabai, and J. Shinar, in *Smart Medical and Biomedical Sensor Technology II,* edited by Brian M. Cullum, SPIE Conf. Proc**.** **5588**, 59 (2004).

[4] B. Choudhury, R. Shinar, and J. Shinar, J. Appl. Phys. **96**, 2949 (2004).

[5] R. Shinar, C. Qian, Y. Cai, Z. Zhou, B. Choudhury, and J. Shinar, in *Smart Medical and Biomedical Sensor Technology III,* edited by B. M. Cullum and J. Chance Carter, SPIE Conf. Proc. **6007**, 600710-1 (SPIE, Bellingham, WA, 2005).

[6] R. Shinar, Z. Zhou, B. Choudhury, and J. Shinar, Anal. Chim. Acta **568** 190 (2006).

[7] W. L. Ramsey, J. M. Vanderkooi, and D. F. Wilson, Science **241**, 1649 (1988).

[8] E. R. Carraway, J. N. Demas, B. A. DeGraff, and J. R. Bacon, Anal. Chem. **63**, 337 (1991).

[9] O. S. Wolfbeis, Editor, *Fiber Optical Chemical sensors and Biosensors* (CRC Press, Boca Raton, FL, 1991).

[10] B. H. Weigl, A. Holobar, W. Trettnak, I. Klimant, H. Kraus, P. O'Leary, and O. Wolfbeis, J. Biotech. **32**, 127 (1994).

[11] S. Draxler, M. E. Lippitsch, I. Klimant, H. Kraus, and O. S. Wolfbeis, J. Phys. Chem. **99**, 3162 (1995).

[12] H. Szmacinski et al. Biophys. Chem. **62**, 109 (1996).

[13] Z. Rozenzweig and R. Kopelman, Sensors and Actuators B **35-35**, 475-483 (1996).

[14] X. Li and Z. Rosenzweig, Anal. Chim. Acta **353**, 263 (1997).

[15] X.-Q. Guo et al. Anal. Biochem. **254**, 179-186 (1997).

[16] S.-K. Lee and I. Okura, Analyst **122**, 81 (1997).

[17] S.-K. Lee and I. Okura, Anal. Comm. **34**, 185 (1997).

[18] D. B. Papkovksy, A. N. Ovchinnikov, V. I. Ogurtsov, G. V. Ponomarev, T. Korpela, Sens. & Act. B **51,** 137 (1998).

[19] F. N. Castellano, and J. R. Lakowicz, Photochem. Photobio. **67**, 179 (1998).

[20] J. R. Lakowicz, *Principles of Fluorescence Spectroscopy,* 2nd edition, Kluwer Academic/Plenum Publishers, 1999.

[21] A. N Ovchinnikov, V. I. Ogurtsov, W. Trettnak, and D. B. Papkovsky, . Anal. Lett. **32**, 701 (1999).

[22] X. Lu, I. Manners, and M. A. Winnik, Macromol. **34**, 1917 (2001).

[23] X. Lu and M. A. Winnik, Chem. Mater. **13**, 3449 (2001).

[24]J.M. Kurner, I. Klimant, C. Krause, H. Preu, W. Kunz, and O.S. Wolfbeis, Bioconjugate Chem. **12**, 883 (2001).

[25] M. Smiddy, N. Papkovskaia, D. B. Papkovsky and J. P. Kerry, Food Res. Intl. **35**, 577 (2002).

[26] Y. Amao, Microchim. Acta **143**, 1 (2003).

[27] Z.J. Fuller, W.D. Bare, K.A. Kneas, W.-Y. Xu, J.N. Demas, and B.A. DeGraff, Anal. Chem. **75**, 2670 (2003).

[28] R. Ramamoorthy, P. K. Dutta, S. A. Akbar, J. Mat. Sci. **38**, 4271 (2003).

[29] P. Roche, R. Al-Jowder, R. Narayanaswamy, J. Young, and P. Scully, Anal. Bioanal. Chem **386**:1245 (2006).

[30] Martin Störzer, Christof M. Aegerter, and Georg Maret, Phys. Rev. B **73**, 065602 (2006).

[31] Dupont online brochure on the TiO2 particles.

[32] D. B. Papkovksy, Sensors and Actuators B, **11**, 293 (1993).

[33] B. J. Matterson, J. M. Lupton, A. F. Safonov, M. G. Salt, W. L. Barnes and I. D. Samuel, Adv. Mat. **13**, 123 (2001).

[34] S. R. Forrest, Organic Electronics **4**, 45 (2003).

[35] S. Moller, S. R. Forrest, J. Appl. Phys. **91**, 3324 (2002).

7. SUMMARY AND GENERAL CONCLUSIONS

This thesis described the basic properties of OLEDs, which included combinatorial screening of CBP-based UV-violet OLEDs and extremely bright and highly efficient white OLEDs. In Chapter 2, the optimal CBP-based UV-violet-OLED structure was determined by varying the thicknesses of the CBP and BCP layers. A maximum radiance of 20 W/m^2 was achieved at 500 mA/cm^2. The stability of these OLEDs was also discussed. It was shown that the peak emission wavelength 380 nm did not change appreciably over a wide range of applied bias. Highly efficient and bright white OLEDs were achieved by using a complementary mixed color technique. Combining a fluorescent layer of rubrene-doped $Almq_3$ and a double hole transport layer structure, a maximum external quantum efficiency of 4.5% and power efficiency of 6.41 lm/W was obtained. The WOLED color coordinates were only weakly affected by the driving voltages.

Structurally integrated OLED-based chemical and biological sensors were discussed in detail. A hydrazine sensor, based on the reaction between non-luminescent anthracene-2,3-dicarboxaldehyde and hydrazine or hydrazine sulfate, which generates a luminescent product, was described. The limit of detection for hydrazine gas bubbled through the ADA solution far exceeded OSHA requirements. The use of ultra-thin OLED excitation source in PL–based sensors will enable the realization of small-size, robust, field-deployable sensors for industrial and environmental security.

The oxygen sensors' performance was evaluated in detail in Chapter 5. The detection sensitivity, dynamic range, gas flow rate, and temperature effect, including the temperature dependence of τ in pure Ar and O_2 atmospheres, was discussed in detail. The dependence of

the sensitivity on the preparation procedure of the sensing film and on the PS and dye concentrations in the sensing element, whether a solid matrix or solution, were also evaluated. That sensor exhibited a high sensitivity, but a limited dynamic range. Effects of aggregation of dye molecules, sensing film porosity, and the use of the OLED-based sensor arrays for O_2 and multianalyte detection were also discussed. The ease of OLED fabrication and OLED/sensing component structural integration results in compact devices, which are expected to be inexpensive and suitable for real word applications.

A uniquely simple approach to increase the intensity of the photoluminescence (PL) of dye-doped sensor films is demonstrated in Chapter 6 for oxygen sensors, where the sensor film, i.e., Pt (octaethylporphyrin) or the Pd analog embedded in polystyrene, was additionally doped with small-size particles that have a high dielectric constant, such as 360 nm titania (TiO_2) particles. The improved S/N can improve the analyte limit of detection, allow shortened data acquisition times, and enable the use of low-intensity excitation sources to minimize potential dye photobleaching. In particular, it improves the performance of structurally integrated OLED-based chemical and biological sensors, which are drawing increasing attention due to their uniquely simple and flexible integration geometry.